

TOWARDS PATIENT-SPECIFIC DOSE AND IMAGE QUALITY ANALYSIS IN CT IMAGING

Caro Franck

Supervisors: Prof. Dr. Ir. K. Bacher, Prof. Dr. E. Achten

Thesis submitted in fulfilment of the requirements for the degree of
Doctor in Health Sciences

Department of Basic Medical Sciences
Faculty of Medicine and Health Sciences
2017

Supervisors

Prof. Dr. Ir. K. Bacher

Prof. Dr. E. Achten

Examination Board

Chairman: Prof. Dr. Ir. C. De Wagter¹

Prof. Dr. P. Parizel²

Prof. Dr. N. Buls³

Prof. Dr. G. Villeirs¹

Prof. Dr. Ir. S. Vandenberghe¹

Prof. Dr. L. Van Hoorebeke¹

Em. Prof. Dr. H. Thierens¹

¹ Ghent University, Belgium

² University Hospital Antwerp, Belgium

³ Vrije Universiteit Brussel, Belgium

Research Institute

Ghent University

Faculty of Medicine and Health Sciences

Department of Basic Medical Sciences

Medical Physics Division

Proeftuinstraat 86, N7

B-9000 Ghent

Tel: +32(0) 9 264 66 50

Sanguis, sudor et lacrimae

Een woord van dank

't Is gebeurd! De interne verdediging is achter de rug, de uitnodigingen zijn de deur uit en de allerlaatste woorden worden zorgvuldig neergepend in dit dankwoord. Het besef dat het hele PhD-avontuur op zijn einde loopt begint langzaam door te dringen. Alhoewel ik mij aan een nog nooit eerder ervaren gevoel van opluchting had verwacht blijft dat voorlopig nog even uit. Ik surf nog verder op de stressgolf van de laatste maanden en kan dit hoofdstuk pas definitief afsluiten wanneer ik iedereen heb bedankt die aan de verwezenlijking van dit proefschrift heeft meegewerkt, zij het bewust of onbewust.

Helemaal terecht bedank ik eerst mijn promotor Prof. dr. ir. Bacher en co-promotor Prof. dr. Achten. Klaus, het scheelde niet veel of ik had gebouw N7 op het INW nooit leren kennen. Door omstandigheden kon ik niet starten met mijn initieel gekozen masterthesis en schakelde ik jouw hulp in. Je was onmiddellijk bereid om samen met mij nog een onderwerp uit te werken. Toen je me aan het einde van het academiejaar vroeg of ik interesse had in een doctoraat moest ik niet lang nadenken. Jouw expertise en kritische begeleiding hebben ervoor gezorgd dat ik mezelf heb kunnen ontplooien. Klaus, bedankt voor het vertrouwen. Professor Achten, zonder de samenwerking met de dienst Radiologie van het UZ Gent had dit proefwerk niet tot stand kunnen komen, waarvoor mijn oprechte dank.

Daarnaast wil ik ook alle leden van de examencommissie bedanken voor het kritisch nalezen van mijn manuscript. Jullie opmerkingen en vragen hebben dit werk naar een hoger niveau getild.

Als medisch fysicus een klinische studie opstarten is niet vanzelfsprekend. Zonder de hulp van Dr. Smeets en Dr. Lapeire was me dit nooit gelukt. Mede dankzij hen is de X-CARE studie een prachtige kers op de taart geworden. In de laatste fase van mijn doctoraat heb ik dr. Snoeckx leren kennen. Annemiek, ik wil jou niet alleen bedanken voor de gecreëerde opportuniteiten, maar ook voor de opkikkertjes tijdens de laatste loodjes.

Tijdens mijn PhD-periode heb ik de kans gekregen om verschillende thesisstudenten te mogen begeleiden. Samen hebben we vele uren aan de scanner doorgebracht, met mooie resultaten als gevolg. Bo, Delphine, Amélie, Bieke, Daphne, Maarten, Mattias, Charles en Leen, het was een plezier om met jullie samen te werken.

Nog even terug naar dat fameuze gebouw N7. Wat een pareltjes van collega's vind je daar! Door jullie aanwezigheid was het steeds een plezier om te komen werken. Nancy, Lothar, Levi en Myriam: bedankt om de lunchpauzes op te vrolijken en het beste van jullie zelf te geven tijdens de saloons. Chamberlain, I still have your cheetah on my desk, I call her Kike. Isabelle, jij zorgde als copiloot voor significant meer duiding tijdens de autoritjes naar Antwerpen. Bedankt om in je drukke werkschema tijd te maken voor serieuze en minder serieuze babbels.

Sommige collega's zochten andere oorden op: Nele, Robbe, Régine, Kim en Stephanie, jullie worden nog steeds gemist. Professor Thierens, bedankt voor de vrolijke noot en de vele diepzinnige gesprekken. An DC en Liesbeth, QCC dames van het eerste uur, ik heb waanzinnig veel bijgeleerd van jullie en ben jullie daar ontzettend dankbaar voor. Jullie moesten eens weten hoe vaak ik nog denk: 'Hoe zouden An en Liesbeth dit oplossen?'. Virginie, onze rots in de branding, wat moeten we zonder jou? Bedankt voor de goede raad, ik kon steeds bij jou terecht met al mijn vragen. Sofie, als bureaugenootjes hadden we weinig geheimen voor elkaar. Bedankt voor je nuchtere kijk op het leven en om mijn dagen op te vrolijken wanneer het nodig was. Charlot, jou wil ik bedanken voor de vele hilarische momenten op en naast het INW. Ik kon ook steeds rekenen op een luisterend oor wanneer het even wat minder ging.

Sarah, bedankt om ons QCC-team te vervolledigen. Tim, ik heb je tijdens je stage zien openbloeien tot een volwaardig QCC-lid, dikke duim! An DH, jouw expertise op vlak van mammo is bewonderenswaardig. Het is daarom ook schitterend te zien wat jij naast het vele werk nog allemaal in elkaar weet te knutselen. Je creaties worden steeds maar professioneler. Dimi, geen vraag of opdracht is jou teveel. Bedankt voor de dubbelzinnige mopjes, maar vooral ook een welgemeende dankjewel om steeds met veel enthousiasme klaar te staan en te willen helpen. Lore, waar moet ik beginnen? Van onderuit gaan in operatiezalen, over het Roos Kotje, tot wilde avonturen in Druisland, we hebben het allemaal meegemaakt. Hoewel ik je eerst maar een overenthousiaste spraakwaterval vond, ben je ondertussen gepromoveerd van collega tot bestie. Jou kan ik niet genoeg bedanken voor de vriendschap die er tussen ons ontstaan is.

Na een zware werkweek zorgden de Kontich Kittens er iedere keer weer voor dat de stress van me afgeschud kon worden op (en ook naast) het basketveld. Woo's, ook jullie wil ik bedanken om mijn Gents sociaal leven in stand te houden. Het is altijd een beetje thuis komen wanneer ik met jullie afspreek. Ayla, bedankt voor je wijze raad. Ik weet dat ik steeds met alles bij jou terecht kan, merci daarvoor.

Mama en papa, mede dankzij jullie onvoorwaardelijke steun en liefde ben ik kunnen opgroeien tot wie ik nu ben. Dikke merci voor jullie support in alles wat ik doe.

Anja, moon of my life, dit is ondertussen al het tweede doctoraat dat we samen doorzwommen hebben. Je hebt het hele traject van dichtbij gevolgd en ik ben je ontzettend dankbaar voor de steun die je me daarbij gegeven hebt. De laatste maanden gingen we door een moeilijke periode. De eindsprint van mijn doctoraat maakte het er niet makkelijker op. Nu dat hoofdstuk achter de rug is hebben we terug meer tijd om volop te genieten van ons gezinnetje.

Liv, mijn kleine knollebol, telkens wanneer ik jouw vrolijke snoetje zag, smolten alle PhD-perikelen als sneeuw voor de zon. Jij doet me beseffen wat echt belangrijk is in het leven.

Promotoren, juryleden, studenten, (ex-)collega's, vrienden en familie, mijn oprechte dank aan jullie allemaal.

Bazinga!

Caro

26 juni 2017

Table of contents

<i>Summary</i>		<i>i</i>
<i>Samenvatting</i>		<i>v</i>
<i>List of acronyms</i>		<i>ix</i>
Part I	Introduction	1
1	Computed Tomography	3
1.1	Basic principles	3
1.2	The role of CT in medical imaging	7
1.3	References	10
2	CT dosimetry	11
2.1	Standard dose metrics	11
2.1.1	CTDI and DLP	11
2.1.2	Size-specific dose estimate	13
2.2	Organ dose calculation	15
2.2.1	Anthropomorphic phantoms	15
2.2.2	Mathematical computational phantoms	16
2.2.3	Individualized voxel models	18
2.3	Monte Carlo simulation for individualized dosimetry	19
2.3.1	Mean free path	20
2.3.2	X-ray interactions	21
2.3.3	Scattering angle and energy loss	21
2.3.4	Monte Carlo transport codes	23

2.4	Risk estimation	25
2.5	References	27
3	Dose reduction tools in CT	29
3.1	Automatic exposure control	29
3.2	Organ-based tube current modulation	32
3.3	Peak kilovoltage optimization	34
3.4	Iterative reconstruction	35
3.5	Adaptive Z-collimation	37
3.6	Other dose reducing techniques	38
3.7	References	40
4	Image quality assessment in CT	43
4.1	Objective image quality	43
4.2	Subjective image quality	47
4.3	Automatic image quality evaluation	50
4.4	References	54
5	Aim and outline of the thesis	55
5.1	References	57
Part II	Original research	59
6	Influence of localizer and scan direction on the dose-reducing effect of automatic tube current modulation in computed tomography	61
7	Evaluation of automatic image quality assessment in chest CT – A human cadaver study	77
8	Patient-specific dose and risk estimation for organ-based tube-current modulation in chest CT	99

9	The role of Size-Specific Dose Estimate (SSDE) in patient-specific organ dose and cancer risk estimation in paediatric chest and abdominopelvic CT examinations	117
Part III	General discussion	137
10	Tube current modulation	139
10.1	References	146
11	Dose calculation and risk estimates	147
11.1	References	157
12	Image quality	159
12.1	References	162
13	Final conclusions	163
14	Future perspectives	165
Part IV	About the author	167
15	Curriculum Vitae	169

Summary

As opposed to conventional radiography, computed tomography provides 3D information of the anatomical structures and tissues of the patient, at a much better low-contrast performance. However, radiation doses associated with CT are up to 40 times higher compared to conventional X-ray examinations. In addition, the number of scans performed increases every year. Since a small but significant risk of radiation induced malignancies is associated with exposure to ionizing radiation, CT imaging must be optimized to assure the required diagnostic level of image quality (IQ) at the lowest possible dose.

The aim of this PhD work was to assess the performance of CT systems in terms of patient dose and IQ. To this end, Monte Carlo simulations were performed with voxelized phantoms, based on clinical CT data. IQ was evaluated by means of an automatic scoring algorithm based on local standard deviations. Using the proposed methods, the behaviour of tube current modulation (TCM) techniques was investigated. In addition, a simplified approach for patient-specific organ dose calculation and risk estimation was developed for use in clinical practice.

To reduce patient radiation dose and to optimize IQ in CT imaging, tube current modulation (TCM) systems were developed. By modulating the tube current along the length axis of the scan, a constant IQ level can be obtained throughout the patient. The tube current is adapted based on a projection radiograph, taken prior to the CT acquisition in either the anterior–posterior (AP), posterior–anterior (PA) or lateral (LAT) direction. As a result, exposure values will be lowered in less attenuating or smaller anatomical regions. In this work, the influence of the localizer type and the scan direction on the dose reducing efficacy of TCM systems was investigated. Chest CT scans based on AP, PA, LAT or dual AP/LAT localizers were acquired on systems from 3 different vendors. In addition the scan direction was changed for one particular system. Organ doses were calculated with Monte Carlo simulations and validated in an anthropomorphic phantom. Thyroid and lung doses increased with 60% for a PA- instead of dual AP/LAT-based scan, with significant differences in image noise. In addition, the thyroid dose halves by taking the scan in the caudocranial (feet first) direction. IQ was not significantly different when changing the scan direction. Our results demonstrate a strong need for detailed analysis of the TCM system performance during commissioning of CT scanners.

The traditional physical-technical image quality parameters are measured in dedicated technical phantoms which are not representative to the patient's anatomy. Clinical IQ has to be determined with extensive human observer studies. An automatic algorithm based on local standard deviations in the image was evaluated for use in clinical practice. Chest CT's of Thiel embalmed cadavers were made at different exposure levels. Soft and sharp datasets were acquired with filtered back projection and iterative reconstruction. A visual grading analysis study was set up to validate the outcome of the automated algorithm. A significant correlation was found between the observed clinical IQ and the proposed scoring method ($\rho = 0.91$, $p < 0.001$). The automatic scoring algorithm is a promising tool for the evaluation of thoracic CT scans in daily clinical practice.

The absorbed dose to the female breast in thoracic CT imaging is up to 10 times higher than in screening mammography. Since the breasts are rarely the object of interest in chest scans, concern is raised about the elevated population risk of breast cancer incidences from CT. We evaluated the performance and dose reducing potential of organ-based TCM (OBTCM), a technique developed to lower the exposure to anterior located organs. The position of the breasts with respect to the reduced tube current zone was determined. Monte Carlo simulations of standard and OBTCM based scans were performed with clinical CT data of 17 female patients. Individual organ doses and risks were compared between both scan techniques. The potential benefit of OBTCM to the female breast in chest CT is overestimated as the reduced tube-current zone is too limited. Despite a 9% reduction of the breast dose, posterior organs will absorb to 26% more dose, resulting in no additional benefit for reduction of radiation induced malignancies.

Performing Monte Carlo simulations is not possible in a clinical setting. Therefore, in this work a simplified method was developed to estimate patient-specific organ doses and lifetime attributable risks (LAR) resulting from CT torso examinations. Individualized voxel models were created from full body CT data of 10 paediatric patients. Patient-specific organ doses and LAR of cancer incidence and mortality were calculated by means of Monte Carlo simulations. Results were compared to the size-specific dose estimate (SSDE). The latter showed significant strong correlations with organ dose ($r > 0.8$) and LAR ($r > 0.9$). Consequently, this dose metric can be used to estimate patient-specific organ doses and risks by taking into account a linear correction factor. The SSDE method makes an on-the-spot dose and LAR estimation possible in routine clinical practice.

The correct use of tube current modulation systems can provide a significant dose reduction in CT imaging. However, positioning the patient in the isocenter of the gantry is extremely important. Miscentering causes an incorrect functioning of the modulation technique as the shadow on the scanned projection radiograph will be too small or too large. In addition, SSDE calculations will be over- or underestimated. Performing Monte Carlo simulations with voxelized phantoms based on clinical CT data of the patient provides an accurate estimate of the delivered dose to in-beam organs. However, the

dose distribution outside the field of view is unknown so that conclusions about organs on the periphery of the model should be taken with care.

This PhD work emphasizes the need for patient-specific dosimetry and image quality assessment in computed tomography. The patient's anatomy, including the relative positions of the different organs, needs to be taken into account when evaluating the performance of different systems. Preferably, individualized organ doses should be determined in a Monte Carlo environment using the patient's CT dataset. However, as this is not possible in a clinical setting, the SSDE method established in this thesis provides a good approximation. In addition, the proposed IQ scoring algorithm has proven to be a valuable alternative for clinical image quality assessment. The method could allow for IQ monitoring over time without the need for human intervention.

Samenvatting

In tegenstelling tot conventionele radiografie is CT in staat om 3D informatie van de anatomische structuren en weefsels van de patiënt te genereren. In vergelijking met een conventionele RX opname echter, kan de stralingsdosis van een CT onderzoek tot wel 40 keer hoger zijn. Bovendien neemt het aantal uitgevoerde scans ieder jaar toe. Blootstelling aan ioniserende straling zorgt voor een klein, maar significant risico op stralingsgeïnduceerde maligniteiten. Het is dan ook noodzakelijk dat CT beeldvorming wordt geoptimaliseerd, om het vereiste beeldkwaliteitsniveau te kunnen garanderen aan een zo laag mogelijk dosis.

Het doel van deze thesis was om de werking van CT systemen te beoordelen, met betrekking tot dosis en beeldkwaliteit. Voxelfantomen, op basis van klinische CT data, werden gebruikt om Monte Carlo simulaties uit te voeren. De beeldkwaliteit werd geëvalueerd aan de hand van een automatisch algoritme, gebaseerd op lokale standaarddeviaties. Met deze methodiek werd het gedrag van buisstroomodulatie onderzocht. Verder werd een vereenvoudigde benadering ontwikkeld om patiëntspecifieke orgaandoses en risico's te bepalen in de klinische praktijk.

Om de stralingsdosis te verlagen en de beeldkwaliteit te optimaliseren in CT beeldvorming werden buisstroomodulatie technieken ontwikkeld. Door de buisstroom te moduleren langsheen de lengte-as van de scan wordt het beeldkwaliteitsniveau constant gehouden doorheen de patiënt. De buisstroom wordt aangepast op basis van een topogram dat op voorhand wordt genomen, in de anterieur-posterieure (AP), posterieur-antérieure (PA) of laterale (LAT) richting. Als gevolg zal de exposie worden verlaagd in minder attenuerende of smallere anatomische regio's. Zowel de invloed van het topogram type en de scanrichting op het dosisreducerend effect van deze modulatietechniek werd in dit werk onderzocht. Op basis van een AP, PA, LAT of dubbel AP/LAT topogram werden thorax scans genomen met CT's van 3 verschillende fabrikanten. Bovendien werd de scanrichting gewijzigd voor 1 welbepaald toestel. Met behulp van Monte Carlo simulaties werden orgaandoses berekend die nadien werden gevalideerd met een antropomorf fantoom. De schildklier- en longdosis nam met 60% toe wanneer de scan gebaseerd was op een PA- in plaats van een dubbel AP/LAT topogram. Dit resulteerde tevens in significante verschillen in beeldkwaliteit. De schildklierdosis halveerde wanneer de scan in de caudocraniale richting (voeten eerst) werd genomen. Hierbij werden geen significante verschillen in

beeldkwaliteit waargenomen. Onze resultaten tonen aan dat een gedetailleerde analyse van de werking van de buisstroommodulatie absoluut noodzakelijk is bij de kwaliteitscontrole van een CT scanner.

De klassieke fysisch-technische beeldkwaliteitsparameters worden gemeten in welbepaalde technische fantomen, welke niet representatief zijn voor de anatomie van de patiënt. De klinische beeldkwaliteit dient te worden beoordeeld met human observer studies. Een automatisch algoritme, op basis van lokale standaarddeviaties in het beeld, werd geëvalueerd voor gebruik in de klinische praktijk. Er werden thorax scans van Thiel gebalsemde lichamen gemaakt bij verschillende exposities. Zachte en scherpe kernels werden gebruikt om de beelden zowel met iteratieve als met filtered back projectie te reconstrueren. Om het automatisch algoritme te valideren werd een visual grading analysis opgezet. Er werd een significante correlatie gevonden tussen de klinische beeldkwaliteit en de voorgestelde scoringsmethode ($\rho = 0.91$, $p < 0.001$). Het automatisch scoringsalgoritme biedt grote mogelijkheden voor de evaluatie van thorax scans in de klinische praktijk.

De geabsorbeerde borstdosis in thoracale CT beeldvorming kan tot wel 10 maal hoger zijn dan bij een screeningsmammografie. Omdat het borstklierweefsel zelden de reden van de scan is, groeit de bezorgdheid over het verhoogde risico op borstkanker ten gevolge van CT onderzoeken. De werking en potentiële dosisreductie van orgaan-gebaseerde buisstroommodulatie werd in dit werk onderzocht. De techniek werd ontwikkeld om de dosis van anterior gelegen organen te verlagen. De positie van de borsten ten opzicht van de gereduceerde dosiszone werd bepaald. Monte Carlo simulaties van standaard en orgaan gemoduleerde scans werden uitgevoerd op basis van klinische CT data van 17 vrouwelijke patiënten. Individuele orgaandoses en risico's werden vergeleken tussen beide opnames. Het voordeel van orgaan-gebaseerde buisstroommodulatie wordt overschat, aangezien de gereduceerde dosiszone te klein is. Ondanks een borstdosisreductie van 9% absorberen posterieure organen tot 26% meer dosis. Dit zorgt ervoor dat het risico op stralingsgeïnduceerde maligniteiten niet vermindert.

In de klinische praktijk is het niet mogelijk om Monte Carlo simulaties uit te voeren. Daarom werd in dit werk een vereenvoudigde methode ontwikkeld om patiëntspecifieke orgaandoses en risico's te bepalen ten gevolge van een CT scan van de torso. Geïndividualiseerde voxelmodellen werden gecreëerd op basis van volledige lichaamsscans van 10 pediatrische patiënten. Patiëntspecifieke orgaandoses en risico's werden berekend met Monte Carlo simulaties. De resultaten werden vergeleken met de size-specific dose estimate (SSDE). Deze laatste correleerde significant met de verkregen orgaandoses ($r > 0.8$) en risico's ($r > 0.9$). Bijgevolg kan deze dosisparameter gebruikt worden om patiëntspecifieke orgaandoses en risico's te berekenen, mits rekening te houden met een lineaire correctiefactor. De SSDE-methode zorgt voor een on-the-spot dosis en risico bepaling in de klinische praktijk.

Mits een correct gebruik van buisstroommodulatie kan een significante dosisreductie worden verkregen in CT beeldvorming. Het correct positioneren van de patiënt in het isocentrum van de scanner is echter van cruciaal belang. Bij een foute positionering zal de modulatietechniek niet correct functioneren. De schaduw op het topogram is dan immers te groot of te klein. Bovendien zullen de SSDE waarden onder- of overschat worden. Het uitvoeren van Monte Carlo simulaties met voxelfantomen op basis van klinische CT data laat toe om de geabsorbeerde dosis in organen binnen het stralingsveld accuraat te bepalen. De dosisverdeling buiten de field of view is echter niet gekend, zodat conclusies over organen op de rand van het voxelmodel met de nodige voorzichtigheid dienen te gemaakt te worden.

Deze PhD thesis benadrukt de nood voor patiëntspecifieke dosimetrie en beeldkwaliteitsbepaling in CT beeldvorming. Wanneer de werking van verschillende CT systemen wordt geëvalueerd, moet rekening gehouden worden met de anatomie van de patiënt, inclusief de relatieve positie van de verschillende organen. Bij voorkeur dienen individuele organdoses te worden bepaald in een Monte Carlo omgeving, gebruik makend van de CT data van de patiënt. Aangezien dit in een klinische omgeving niet mogelijk is, kan de ontwikkelde SSDE-methode gehanteerd worden. Bovendien werd aangetoond dat het voorgestelde algoritme om de beeldkwaliteit automatisch te scoren, een waardevol alternatief voor klinische beeldkwaliteitsevaluatie kan bieden. Deze methode laat toe om de beeldkwaliteit te monitoren in de tijd zonder menselijke tussenkomst.

List of acronyms

A

AAPM	American Association of Physicists in Medicine
AC	Attenuation Correction
AEC	Automatic Exposure Control
AP	Anterior-Posterior
ALARA	As Low As Reasonably Achievable
ASIR	Adaptive Statistical Iterative Reconstruction
ATCM	Automatic Tube Current Modulation

B

BEIR	Biological Effects of Ionizing Radiation
BMI	Body Mass Index

C

CAP	Chest Abdomen Pelvis
CD	Contrast-Detail
CHO	Channelized Hotelling Observer
CNR	Contrast-to-Noise Ratio
CT	Computed Tomography
COR	Centre of Rotation
CTDI _{vol}	Volume Computed Tomography Dose Index

D

DCS	Differential Cross Section
DDREF	Dose and Dose Rate Effectiveness Factor
DICOM	Digital Imaging and Communications in Medicine
DLP	Dose Length Product
DRL	Dose Reference Level
DNA	Deoxyribonucleic Acid
DQE	Detective Quantum Efficiency
DRL	Dose Reference Level

D_w Water Equivalent Diameter

E

E Effective Dose

EPDL Evaluated Photon Data Library

EUREF European Reference Organisation for Quality Assured Breast Screening and Diagnostic Services

F

FBP Filtered Back Projection

FPF False Positive Fraction

FOV Field of View

G

γ -H2AX Phosphorylated Histone Subtype H2A Isoform X

GSF German National Research Centre for Environment and Health

H

HU Hounsfield Units

I

ICRP International Commission on Radiological Protection

ICRU International Commission on Radiation Units

IQ Image Quality

IQF_{inv} Inverse Image Quality Figure

IQs Image Quality Score

IR Iterative Reconstruction

L

λ Mean Free Path

LAR Lifetime Attributable Risk

LAT Lateral

LiF Lithium Fluoride

LNT Linear-no-Threshold model

M

MBIR Model-based Iterative Reconstruction

MC Monte Carlo

Mg Magnesium

MR Magnetic Resonance Imaging

MTF Modulation Transfer Function

N

NEQ Noise-Equivalent Quanta
nIQs Normalized Image Quality Score
NRPB National Radiological Protection Board
NPS Noise Power Spectrum
NPWE Non-prewhitening Matched Filter

O

OBTM Organ-based Tube Current Modulation
ORNL Oak Ridge National Laboratories

P

p Pitch
PA Posterior-Anterior
PDF Probability Density Function
PET Positron Emission Tomography
PMMA Polymethyl Methacrylate

Q

QRM Quality Reference mAs

R

ROC Receiver Operating Characteristics
ROI Region of Interest
RX Plain Radiography

S

SAFIRE Sinogram Affirmed Iterative Reconstruction
SD Standard Deviation
SDNR Signal Difference to Noise
SNR Signal-to-Noise Ratio
SPECT Single-Photon Emission Computed Tomography
SPR Scan Projection Radiograph
SSDE Size-Specific Dose Estimate

T

Ti Titanium
TLD Thermoluminescent Dosimeters

TCM Tube Current Modulation
TNF True Negative Fraction
TPF True Positive Fraction

U

UNSCEAR United Nations Scientific Committee on the Effects of Atomic Radiation
US Ultrasound

V

VEO
VGA Visual Grading Analysis

Part I

Introduction

Chapter 1

Computed Tomography

1.1 BASIC PRINCIPLES

An example of a modern CT scanner is shown in Figure 1.1. The X-ray tube (T) and detector arrays (D) are mounted, opposite to each other, on a ring shaped gantry. While the gantry is rotating (R) and the X-ray tube produces a broad fan-shaped beam (X), the patient moves continuously through the scanner. This imaging technique is called helical CT. The fan beam is created by placing 2 collimator blocks in front of the tube. In addition, a beam shaping filter is used to account for the elliptical shape of the patient. During an acquisition, the attenuation of the X-ray beam crossing the patient is measured by the detector, at different projection angles.

For each rotation, up to 1000 projections are made and stored in a sinogram. To reconstruct axial images or slices of the patient, the measured attenuation profiles are back projected. A filter is applied in the process to give more weight to certain frequencies and to change the characteristics of the CT dataset. Soft tissue (smooth) filters suppress higher frequencies to reduce the noise at the expense of spatial resolution. Bone (sharp) kernels use these high frequencies so that the images will have more noise but an improved resolution. This process is called filtered backprojection (FBP) and is the traditional reconstruction method used in CT imaging [1]. The method is illustrated in Figure 1.2.

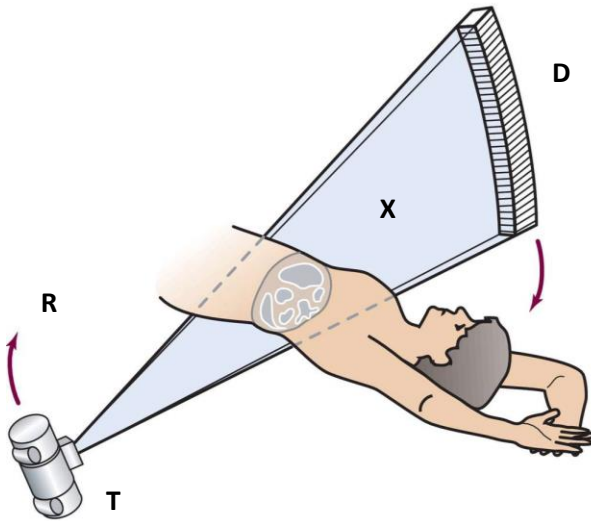
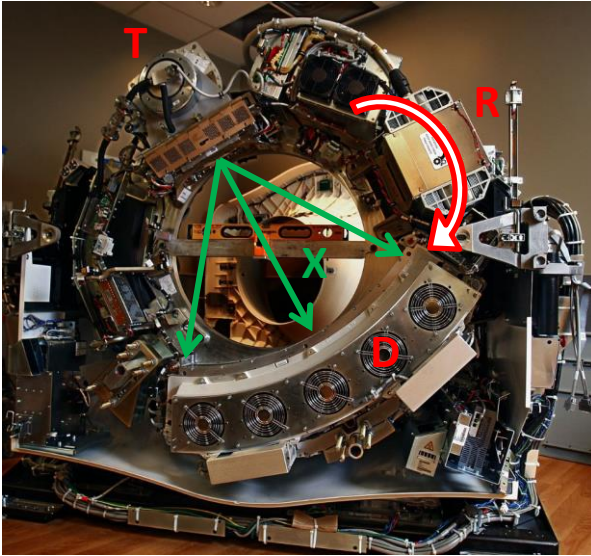


Figure 1.1 Modern CT scanner with cover removed (top) and its schematic representation (bottom), showing the X-ray tube (T), detector arrays (D), X-ray beam (X) and gantry rotation (R) [2].

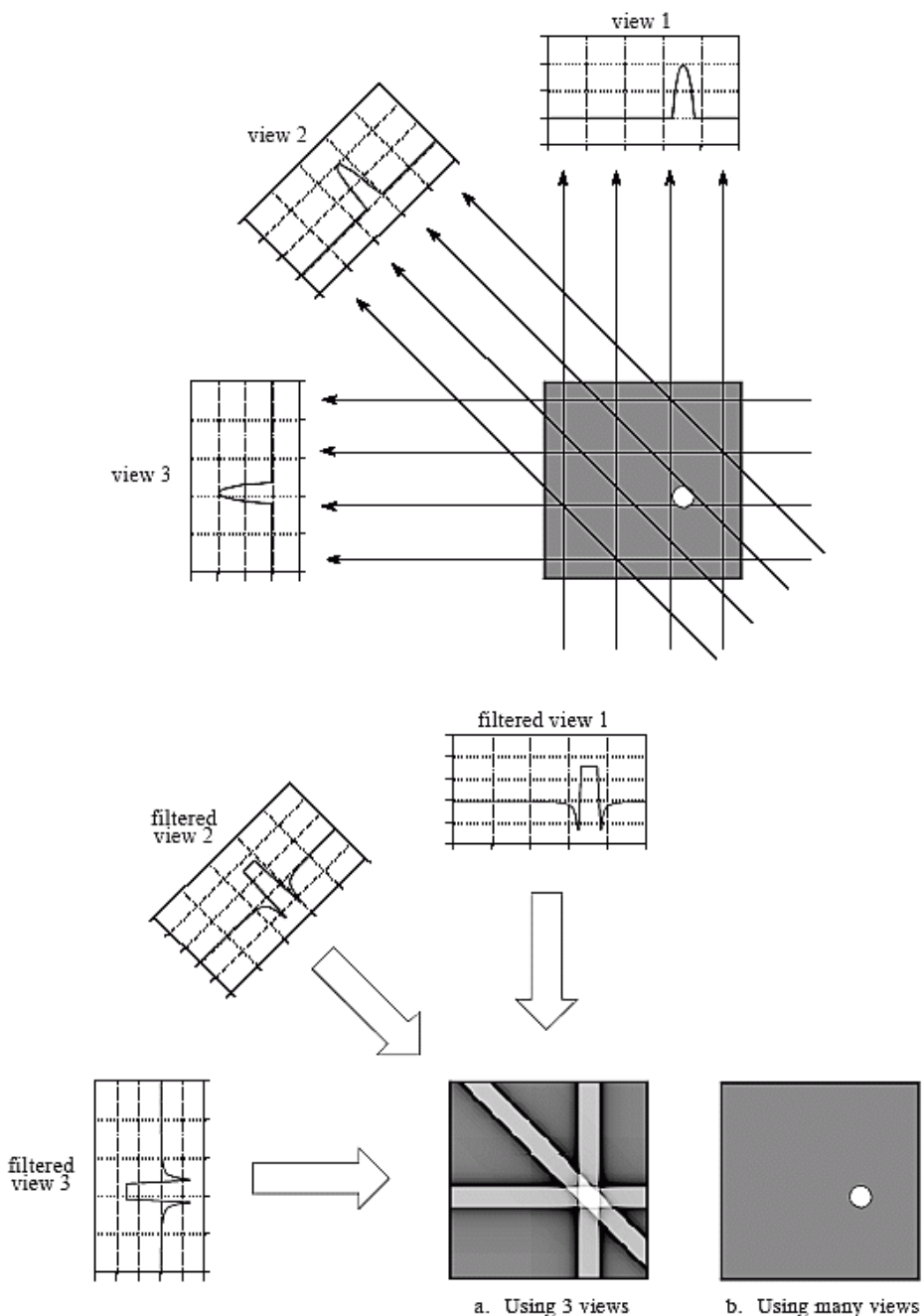


Figure 1.2 Filtered backprojection

Top: projections at different angles of the object are made.

bottom: the measured attenuation profiles are filtered and back projected to generate an image.

The pixel values in a CT image are displayed in Hounsfield Units (HU). These are a linear transformation of the obtained attenuation values, relative to water:

$$HU = \frac{\mu - \mu_{\text{water}}}{\mu_{\text{water}} - \mu_{\text{air}}} \cdot 1000$$

In practice, μ_{air} is neglected with respect to μ_{water} in the Hounsfield Units calculation. The main advantage of CT is that it provides 3D information of the patient, as opposed to conventional RX where all the anatomical structures are projected and superimposed on a 2D image. With present-day pixel sizes as small as 0.23 mm and a good low contrast resolution, CT is able to detect very small details and changes in tissue composition.

In helical CT scanning the spiral pitch factor is an important parameter and is defined as:

$$pitch = \frac{\text{table feed}}{N \cdot T}$$

Where the table feed is the distance the table travels during one rotation. N is the number of slices scanned simultaneously and T is the thickness of a single slice. The product of N and T is referred to as the total beam collimation and is measured in the isocenter of the scanner. If the pitch is chosen to be smaller than 1, the beams of consecutive rotations will significantly overlap, increasing the dose to the patient. On the other hand, a pitch larger than 1 will result in gaps in the imaged volume as adjacent rotations are not contiguous, leading to a decreased patient dose. The choice of the pitch factor is examination dependent, involving a trade-off between coverage and accuracy. High pitch mode can be useful for myocardial perfusion scans as the table speed will increase and motion artefacts will be minimized.

The scan field of view (SFOV) is defined by the fan beam angle and will determine the maximum possible size of the reconstructed images. Typically a head or body SFOV can be selected, each of them using a different shaping filter. The display field of view (DFOV) or reconstruction FOV can be less than or equal to the SFOV and determines how much of the SFOV is reconstructed into an image. If the same matrix is used, a reduced DFOV will result in a smaller pixel size and the achievable resolution will improve.

Providing equivalent radiation to all detector elements requires that the X-ray beam is wider than the collimation such that all detector rows are irradiated by the inner, non-penumbra region, as illustrated in Figure 1.3. The z-axis geometric efficiency characterises the extent of the radiation beam that is used for image creation and is calculated as the ratio of the total beam collimation and the FWHM of the dose profile:

$$geom\ eff = \frac{N \cdot T}{FWHM\ dose\ profile}$$

The fractional loss of dose efficiency associated with the discarded penumbra becomes smaller for larger beam widths, because the penumbra represents a smaller fraction of the

total X-ray beam width [3]. However, during spiral CT procedures, at least an additional half rotation is necessary at the beginning and end of the scanrange to ensure that complete datasets are obtained for the reconstruction of the first and last slices [4]. As a result, before and after the volume of interest, additional tissue is unnecessarily exposed. This z-overscanning effect is more important for larger beam widths.

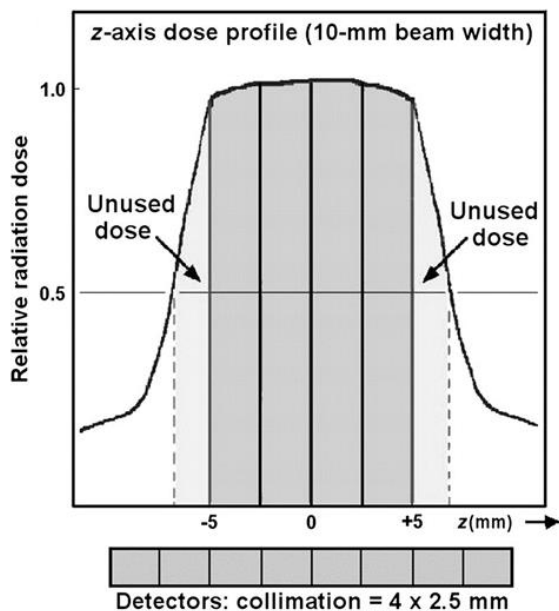


Figure 1.3 Dose profile for a 10 mm wide beam used to irradiate a multislice detector collimation of 4×2.5 mm. The penumbra of the beam is not used for image reconstruction [3].

1.2 THE ROLE OF CT IN MEDICAL IMAGING

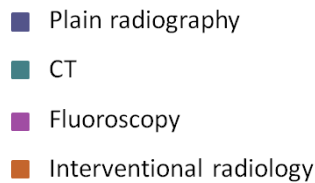
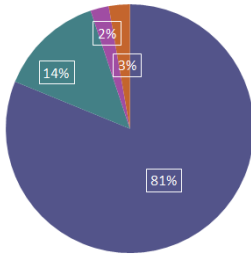
A rising trend of annual performed CT examinations is clearly noticeable in the literature [5-8]. Data from UNSCEAR show an increase in average annual frequency of CT examinations in health-care level I countries from 48 per 1000 population in 1991-1996 to 128 per 1000 population in 1997-2007 [6,9].

From 2011 to 2014, the Dose Dated 2 project collected data on the doses from radiodiagnostic procedures from EU member states. The results are published as Radiation Protection report n° 180 and divided into 4 categories: plain radiography, CT,

fluoroscopy and interventional radiology. Plain RX, including dental imaging, appears to be the most common X-ray examination in all European countries. However, when it comes to effective dose, CT yields by far the highest contribution to the population. More specifically, in Belgium, CT accounts for 60% of the overall collective dose to the medical population, while only 14% of the total number of X-ray procedures in the medical imaging department are CT scans [10]. The relative contributions of the 4 groups are shown in Figure 1.4.

A small but significant increased risk of cancer incidence and mortality is associated with the exposure to ionizing radiation [11]. Typical CT doses are shown in Table 1.1. As a reference the doses resulting from common plain radiography exams are added. Radiation doses from CT are up to 40 times higher compared to conventional X-ray examinations.

number of examinations



collective effective dose

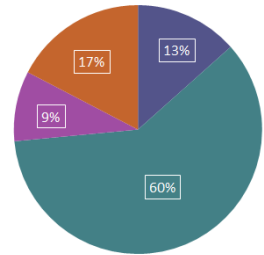


Figure 1.4 Relative contributions to the total number of X-ray procedures and to the resulting collective effective dose in Belgium. Plain radiography includes dental imaging and mammography. [10]

Table 1.1 Typical effective doses, resulting from CT and plain radiography [10]

Radiologic examination	Effective dose (mSv)
CT head	1.3
CT chest	4.2
CT spine	10.1
CT abdomen	8.6
RX thorax	0.09
RX cervical spine	0.17
RX thoracic spine	0.48
RX lumbar spine	3.15
RX abdomen	0.68

The rising number of scans performed, combined with the use of CT in radiation-sensitive populations (children, young adults and pregnant female patients) has drawn the attention to radiation exposure and risks from CT examinations [12].

Apart from the use of CT in diagnostic radiology, there is a significant increase in CT installations in multimodality imaging. Here, the CT data is used to provide precise localization of functional data from nuclear medicine studies. Furthermore, a CT scan delivers accurate attenuation correction (AC) information of the positron emission tomography (PET) and single-photon emission CT (SPECT) data [13]. Since the CT acquisitions are not used for diagnostic purposes, the use of low dose protocols is essential. The need to optimize the use of CT in hybrid imaging is high as little standardization exists.

Efforts are made to replace some of the stand-alone CT examinations by magnetic resonance imaging (MR) scans. MR acquisitions are not performed with ionizing radiation and provide an extremely good low contrast resolution in soft tissue regions. However, the use of MR is restricted due to the limited availability and longer scanning times, compared to CT. In addition, the use of high magnetic field strengths can cause biological effects and physical harm to the patient.

MR can also play a role in the nuclear medicine department. State-of-the-art technologic advances made it possible to replace CT by MR in hybrid PET imaging. Although the emerging PET/MR solutions are promising in terms of patient dose, MR based AC is challenging as it does not provide direct information on electron densities needed for PET AC [14,15]. Bone and air have a near-zero signal in conventional MR images, yet bone regions result in high photon attenuation levels per unit volume, whereas air does not cause any photon attenuations. The most difficult task of MR-based AC is to separate bone from air and other tissue. To date, the use of integrated PET/MR systems in a clinical setting is restricted due to the limited availability, cost and the aforementioned technical challenges [16]. As PET/CT systems will continue to be used, it is important to minimize the radiation exposure, resulting from the CT acquisition.

Although the individual risk estimates from CT acquisitions are small, they have to be applied to an increasingly large population [8]. Therefore, care must be taken that every examination is performed at the lowest possible dose (ALARA principle). Children are more sensitive to radiation than adults due to their rapid cellular proliferation and increased lifetime risk of malignancy [8]. It must be emphasized that if a CT examination is clinically justified, the benefits for the patient will by far exceeds the risks. Unfortunately, far too many clinically unnecessary CT scans are being performed today [17].

1.3 REFERENCES

- 1 Kalender WA (2011) *Computed Tomography: Fundamentals, System Technology, Image Quality, Applications*, 3 edn. Wiley VCH
- 2 Mosby Inc. (2009) *Mosby's medical dictionary*, 8th edn. Mosby, St. Louis, MO
- 3 Goldman LW (2008) Principles of CT: multislice CT. *J Nucl Med Technol* 36:57-68; quiz 75-56
- 4 Tzedakis A, Damilakis J, Perisinakis K, Karantanas A, Karabekios S, Gourtsoyiannis N (2007) Influence of z overscanning on normalized effective doses calculated for pediatric patients undergoing multidetector CT examinations. *Med Phys* 34:1163-1175
- 5 (2007) Milieurapport Vlaanderen, Achtergronddocument ioniserende straling.
- 6 UNSCEAR (2008) Sources and effects of ionizing radiation. Report to the General Assembly of the United Nations. United Nations, New York
- 7 Brix G, Nagel HD, Stamm G et al (2003) Radiation exposure in multi-slice versus single-slice spiral CT: results of a nationwide survey. *Eur Radiol* 13:1979-1991
- 8 Brenner DJ, Hall EJ (2007) Computed tomography--an increasing source of radiation exposure. *N Engl J Med* 357:2277-2284
- 9 UNSCEAR (2000) Sources and effects of ionizing radiation. Report to the General Assembly of the United Nations. United Nations, New York
- 10 EC (2014) Medical Radiation Exposure of the European Population Part 1/2. Radiation Protection 180. Office for Official Publications of the European Communities
- 11 Council N (2006) Health risks from exposure to low levels of ionizing radiation: BEIR VII phase 2. The National Academies Press
- 12 Raman SP, Johnson PT, Deshmukh S, Mahesh M, Grant KL, Fishman EK (2013) CT dose reduction applications: available tools on the latest generation of CT scanners. *J Am Coll Radiol* 10:37-41
- 13 Kinahan PE, Townsend DW, Beyer T, Sashin D (1998) Attenuation correction for a combined 3D PET/CT scanner. *Med Phys* 25:2046-2053
- 14 Akbarzadeh A, Ay MR, Ahmadian A, Alam NR, Zaidi H (2013) MRI-guided attenuation correction in whole-body PET/MR: assessment of the effect of bone attenuation. *Ann Nucl Med* 27:152-162
- 15 Andersen FL, Ladefoged CN, Beyer T et al (2014) Combined PET/MR imaging in neurology: MR-based attenuation correction implies a strong spatial bias when ignoring bone. *Neuroimage* 84:206-216
- 16 Singnurkar A, Poon R, Metser U (2017) Comparison of 18F-FDG-PET/CT and 18F-FDG-PET/MR imaging in oncology: a systematic review. *Ann Nucl Med* 31:366-378
- 17 Brenner DJ, Hall EJ (2012) Cancer risks from CT scans: now we have data, what next? *Radiology* 265:330-331

Chapter 2

CT dosimetry

The imaging process in diagnostic radiology must be optimized to achieve the necessary image quality while minimizing the risks for radiation induced malignancies. To quantify these potential risks, accurate dose calculations are required.

Radiation dosimetry in CT is challenging, because the amount and distribution pattern of the absorbed energy in the patient is difficult to determine. First of all, the human body consists of a very large number of anatomical structures that are heterogeneous in density and composition. In addition, during a CT examination, the broad fan-shaped X-ray irradiates the patient during a helical movement.

To estimate the dose to the patient resulting from a CT scan, different approaches exist. They all have their advantages and disadvantages, as will be discussed below.

2.1 STANDARD DOSE METRICS

2.1.1 CTDI and DLP

The irradiation geometry of CT is different from that of other X-ray modalities. With conventional RX imaging, the X-ray tube is stationary and the entrance skin dose will be higher than the exit dose. In CT, the X-ray tube makes a full rotation around the patient, while irradiating only a narrow section of the body. This will result in a radial symmetric dose gradient in the patient. Along the length axis of the scan, the dose profile will have a peak in the centre and long tails at each side, because of scattered radiation in the body (Figure 2.1).

The computed tomography dose index (CTDI) is the height of the dose profile resulting from a single axial rotation, assuming the complete dose profile $D(z)$ was located in a

rectangular interval with length nS , where n is the number of slices of thickness S (Figure 2.1). The metric is expressed in mGy and calculated as:

$$CTDI = \frac{1}{nS} \int_{-\infty}^{+\infty} D(z) dz$$

CTDI can be measured free in air. Often CTDI reflects the average dose to a cylindrical PMMA phantom, resulting from a CT acquisition. In the latter situation, the CTDI quantity is measured in a phantom with a diameter of either 16cm or 32cm (Figure 2.1). To quantify body scans, the 32cm *body CTDI phantom* is used. The 16cm phantom, referred to as the *head CTDI phantom*, is linked to head CT examinations.

In general the dose profile is not integrated over infinity, but a 10 cm pencil ionization chamber is used for the measurements. Since, the dose at the surface of the phantom will be higher compared to the centre, the weighted CTDI ($CTDI_w$) is introduced as:

$$CTDI_w = \frac{1}{3} CTDI_{100,c} + \frac{2}{3} CTDI_{100,p}$$

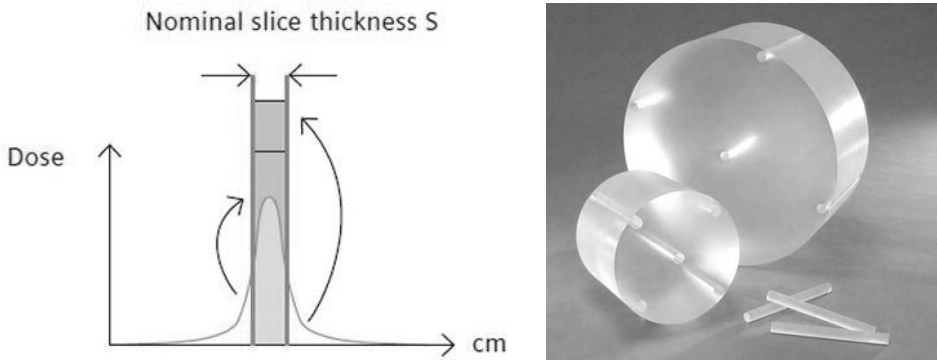


Figure 2.1 (left) In a PMMA phantom, the radiation dose profile along the longitudinal axis contains dose tails caused by scattering. (right) 16cm and 32cm PMMA phantoms used for CTDI measurements on a CT scanner.

Hereby $CTDI_{100,c}$ and $CTDI_{100,p}$ represent the dose in the centre and in the periphery of the PMMA phantom respectively. Typically for body protocols, $CTDI_{100,p}$ will be twice as high as $CTDI_{100,c}$, whereas for head scans both quantities will be approximately equal.

Finally, for spiral acquisitions, the helical pitch p is taken into account by the volume CTDI ($CTDI_{vol}$):

$$CTDI_{vol} = \frac{CTDI_w}{p}$$

To express the total radiation resulting from a CT acquisition, the dose-length product (DLP) is used and measured in mGycm. DLP is calculated by multiplying the $CTDI_{vol}$ with the irradiated scan length. DLP is an overall dose indicator for CT, whereas dose-area product (DAP) is used in projection radiography and fluoroscopy.

It must be emphasized that CTDI is developed to quantify the radiation output of a CT system. It enables the user to compare different scan protocols or scanners. However, because $CTDI_{vol}$ is displayed on the console and included in the patient's dose report, it is often incorrectly assumed that this metric represents the dose delivered to the patient [1]. Therefore, CTDI and DLP only serve as an *index* for CT dose. They are insufficient to describe the absorbed dose to the patient. Although, the attenuation of the used PMMA phantoms is similar to that of a real patient, these homogeneous cylinders are either too small or too big to represent the human anatomy. In addition, calculating individual organ doses is not possible.

2.1.2 Size-specific dose estimate

Volume CTDI provides a standardized method to compare radiation output levels between different CT scanners using a reference phantom. The metric is affected by changes in scan parameters such as tube voltage, tube current, rotation time, pitch and shaping filter. However, this quantity is independent of the size of the patient. When all scan parameters are kept the same, imaging a large or small patient will result in the same $CTDI_{vol}$. Hence, volume CTDI cannot be used to estimate patient dose.

The need to take patient size into account has led to the introduction of the size-specific dose estimate (SSDE) by the AAPM Task Group [2]. SSDE scales the $CTDI_{vol}$, according to the patient's contour. In Chapter 9 of this PhD work, the SSDE is used to develop a clinically applicable method for patient-specific organ dose and lifetime attributable risk estimation.

The formula to estimate the dose for a specific patient size is given by:

$$SSDE = f_{size}^{16} * CTDI_{vol}^{16}$$

for the 16cm CTDI phantom, and

$$SSDE = f_{size}^{32} * CTDI_{vol}^{32}$$

for the 32cm CTDI phantom.

The conversion factors (f^{16} and f^{32}) are tabulated in the AAPM report, as a function of different measures of patient size [2]. In general, the conversion factors are larger than unity for diameters smaller than the reference phantom, and lower than unity for larger patients. To describe the approximate size of the patient, either the LAT dimension, the AP dimension, the sum of the AP and LAT dimensions, or the effective diameter can be used. The effective diameter of the patient is the diameter of the circle whose area is the same as that of the patient's cross-section. Assuming the patient to have an elliptic cross-section, it is seen that:

$$\text{effective diameter} = \sqrt{AP * LAT}$$

The above equation focuses on the geometric size of the patient, in terms of AP and LAT dimensions. In this way, the same scanner output will result in the same SSDE for a thoracic and an abdominal region, if both regions have the same cross-sectional area. However, the lungs are less dense than the abdomen. Therefore, delivering the same $CTDI_{vol}$ will result in a higher absorbed dose to the thorax region, compared to the abdomen region. To deal with this issue, the AAPM Task Group published a new report in 2014, regarding the use of the water equivalent diameter for SSDE calculations [3]. The water equivalent diameter (D_w) takes into account the attenuation of the patient. It is calculated on a specific slice along the length of the patient as:

$$D_w = 2 * \sqrt{\left[\frac{1}{1000} * \mu + 1 \right] * \frac{A}{\pi}}$$

A and μ represent the total area and the mean pixel value (in HU) of the specific axial CT image. Based on D_w , the SSDE is calculated as:

$$SSDE = a * e^{-bD_w} * CTDI_{vol}$$

Where a and b are exponential fit coefficients, depending on the diameter of the PMMA phantom used to measure $CTDI_{vol}$ [3]. The use of attenuation information in addition to the geometry of the patient increases the accuracy of dose estimates, especially for the thorax. If attenuation is not considered, the size of the chest will be overestimated, resulting in an underestimation of the SSDE.

If the patient is scanned with automatic tube current modulation, the scanner output varies considerably along the longitudinal axis. Variations in patient dimension and attenuation causes the tube current values to change during the scan. By decreasing the exposure in less-attenuating regions, the photon flux at the detector will be more homogeneous for all projections. As a result, the reconstructed images will have comparable noise levels and the dose to smaller anatomical regions can be reduced. If automatic exposure control is used, the scanner output (in terms of $CTDI_{vol}$) will be

dependent on the location along the longitudinal axis of the patient. Consequently, the patient's SSDE can be calculated at each position z as:

$$SSDE(z) = f_{D_w}(z) * CTDI_{vol}(z)$$

Finally, the mean SSDE over the entire scan range can be expressed as:

$$\overline{SSDE} = \frac{\sum_{z=1}^N SSDE(z)}{N}$$

where N are the number of slices.

2.2 ORGAN DOSE CALCULATION

In radiation dosimetry, the term *phantom* is used to refer to either a physical object that mimics the human body or a mathematically defined anatomical model.

2.2.1 Anthropomorphic phantoms

A well-established approach to quantify the absorbed dose to the patient is the use of physical anthropomorphic phantoms. Anthropomorphic phantoms are carefully made to represent the human anatomy. They can be used to perform more detailed dose calculations. Compared to CTDI measurements, anthropomorphic phantoms mimic the patient's geometry and attenuation.

The phantom used in Chapter 6 of this PhD dissertation is the Alderson RANDO phantom (Figure 2.2) [4]. It represents the 'standard man', an average person of 170cm and 73.5kg. The phantom is transected horizontally into 2.5cm thick slices. Each slice contains several predrilled holes so that dosimeter chips can be inserted. The phantom consists of two tissue-equivalent materials, following the ICRU44 standards [5], in addition to a natural human skeleton. The lungs are moulded from syntactic foam with a specific gravity of 0.30 g/cc. Soft tissue is manufactured from an urethane mixture. The material has an effective atomic number and mass density which simulates muscle tissue with randomly distributed fat.

Dosimeter chips can be positioned in the predrilled holes of the RANDO phantom. In Paper 2 of this PhD thesis thermoluminescent dosimeters (TLDs) with a diameter of 5 mm and a thickness of 1 mm are used. The chips consist of lithium fluoride, doped with magnesium and titanium (MTS-N; LiF:Mg,Ti) [6].



Figure 2.2 The Alderson RANDO phantom [4]. An anthropomorphic phantom, used in combination with TLDs to measure organ doses in Paper 2 of this PhD thesis.

2.2.2 Mathematical computational phantoms

Experimental methods with physical anthropomorphic phantoms require considerable resources in terms of time and equipment. This often prevent their use in a clinical radiology environment. As an alternative, indirect computational approaches can be used to determine the radiation dose delivered to the patient. The existing computational methods for organ dose assessment resulting from CT exposures are based on Monte Carlo calculations. The radiation transport is simulated in geometric reference phantoms. An example is the family of anthropomorphic phantoms developed by the German National Research Centre for Environment and Health (Gesellschaft für Strahlen; GSF) [7]. The GSF's adult male and female modes, referred to as ADAM en EVA, are depicted in Figure 2.3. Based on computational methods, two main Monte Carlo data sets of normalised absorbed organ doses from CT exposures are available. The databases are generated by the UK National Radiological Protection Board (NRPB) [8,9] and the GSF [10,11].

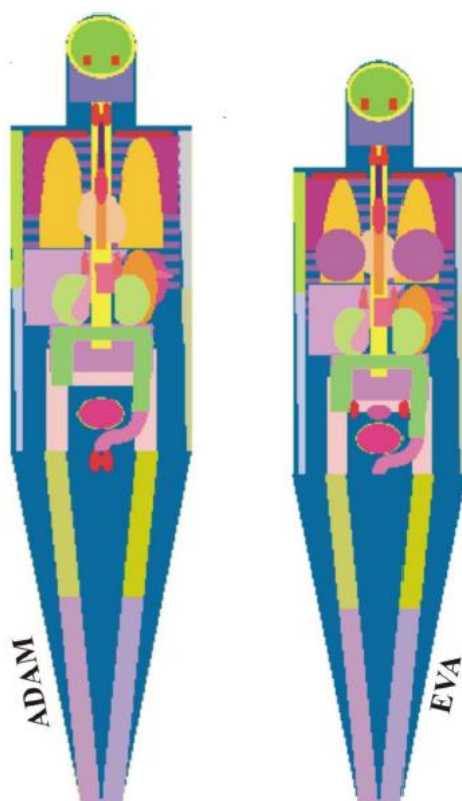


Figure 2.3 The mathematical ADAM en EVA phantoms, developed by the German National Research Centre for Environment and Health (Gesellschaft für Strahlen; GSF) [7].

Several software programs are commercially available, providing organ dose estimates for standard patient sizes and scanners. They are based on the pre-calculated tables of the dose contributions to all organs in a given phantom, resulting from 1 cm wide single section scans. After specifying the patient's scan range, the software adds up the contributions resulting from all sections belonging to the scan range [12]. An overview of different CT dose calculation tools based on pre-tabulated Monte Carlo data is given in Table 2.1.

Table 2.1 Overview of the available CT dose calculation tools, together with the selectable phantoms.

dose calculator	Phantoms
CT-Expo	6w, 7y, adult male, adult female
ImPACT	hermaphrodite adult
ImpactDose	newborn, 1y, 5y, 10y, 15y, adult male, adult female
PCXMC Rotation	newborn, 1y, 5y, 10y, 15y, adult male, adult female

w = week; y = year

The described software tools are useful for training and teaching the influence of different exposure parameter settings on the resulting organ doses. However, determining the absorbed dose of an individual patient is not possible with these methods. The selection of CT scanner models is limited and not always up-to-date. Furthermore, only standard patient sizes at discrete reference ages are available. Considering the diversity among people, especially in paediatrics, it is impossible to represent the whole population with only a few phantom models. In addition, there may be disagreement in patient positioning and uncertainty about the dimensions of the field of view.

2.2.3 Individualized voxel models

Dose calculation tools based on computational phantoms allow a quick, yet imprecise estimation of individual organ doses. In order to make conclusions about potential radiation risks, accurate dose calculations need to be available. Especially for paediatric radiology, only standard patient sizes at discrete reference ages can be selected with these software tools. The use of a more realistic representation of the human anatomy, including a patient-specific model, is recommended.

Individualized 3D voxel models can be created based on clinically available CT images of the patient. The patient's DICOM images are converted into a voxel phantom, which can be used in a Monte Carlo environment. This patient-specific voxelmodel allows to simulate the deposited energy distribution in the patient more accurately, compared to the use of anthropomorphic phantoms. In Chapters 6, 8 and 9 of this PhD thesis, Monte Carlo simulations were performed with ImpactMC (CT Imaging, Erlangen Germany). The software generates a 3D dose distribution in a patient-specific voxel model. After delineating the desired structures on the original CT images, mean organ doses can be estimated using the output images of the simulation (Figure 2.4). The fundamentals of a Monte Carlo simulation are explained in detail in Section 2.3.

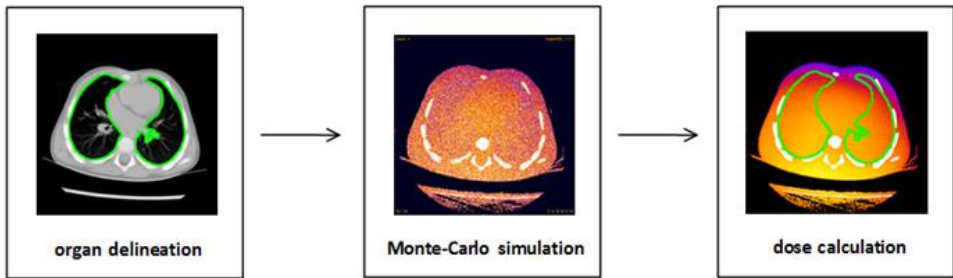


Figure 2.4 Clinical CT images of the patient are used to create a 3D voxel model. After delineating the individual organs, mean organ doses are calculated on the output images of the Monte Carlo simulations [13].

2.3 MONTE CARLO SIMULATION FOR INDIVIDUALIZED DOSIMETRY

Mathematical or physical problems often involve multiple independent variables. Solving them with conventional numerical methods would require a tremendous amount of memory and computer time. Another way of handling complex equations is through approximation, using random numbers and probability statistics. The so-called Monte Carlo (MC) methods solve the problem by directly simulating the underlying physical process and then calculating the average result. They are used for modelling events with a significant uncertainty in inputs. The transport of X-rays in matter, for example, is a natural stochastic process. The type of interaction, energy loss, angular deflection and path length are the main events involved in the simulation of the trajectory of a particle. All these events occur at random.

Figure 2.5 is a schematic representation of the simulation of radiation transport in matter. Consider a photon at a given position \mathbf{r} , direction of flight \mathbf{d} and energy E . These 3 variables determine the *state* of the particle. Hence, each track in the simulation consists of a series of states $(\mathbf{r}_n, \mathbf{d}_n, E_n)$ where \mathbf{r}_n is the position of the n -th scattering event and \mathbf{d}_n and E_n are the direction of flight and energy just after the event.

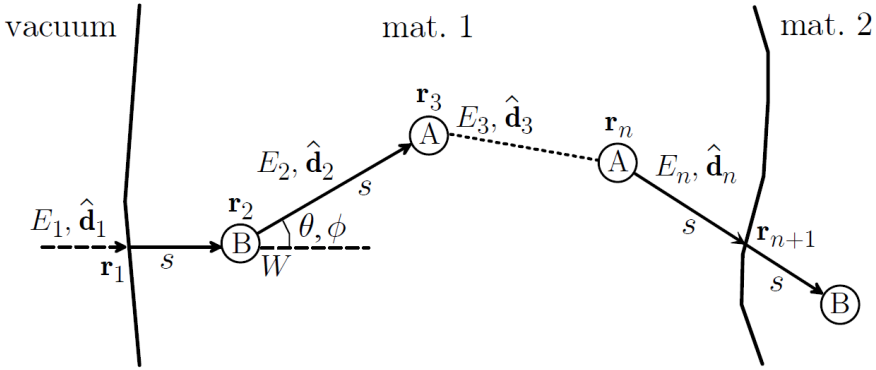


Figure 2.5 Generation of random tracks. A particle enters material 1 from the vacuum and, after multiple interactions, crosses the interface between materials 1 and 2 [14].

The state of the next event (r_{n+1} , d_{n+1} , E_{n+1}) can be calculated as:

$$r_{n+1} = r_n + s * d_n$$

$$d_{n+1} = \mathcal{R}(\Omega) * d_n$$

$$E_{n+1} = E_n - W$$

where the rotation matrix $\mathcal{R}(\Omega)$ is determined by the solid scattering angle Ω . The length s of the free path to the next collision, the interaction type (A or B in Figure 2.5), the scattering angle Ω as well as the energy loss W are random variables, sampled from their corresponding probability density functions (PDF). The PDFs of each stochastic process are deduced from theoretical and measured properties of X-rays.

2.3.1 Mean free path

According to the law of Lambert-Beer, the intensity of an X-ray beam reduces exponentially as it passes through matter [15]. The PDF of the travelled distance of a photon can be expressed as [14]:

$$p(s) = \frac{1}{\lambda} e^{-s/\lambda}$$

with λ the mean free path, defined as the average path length between collisions. The mean free path is a property of the interaction material and the energy of the particle.

Given a random number ξ , the length of the path to the next collision can be sampled from [14]:

$$s = -\lambda \ln(1 - \xi)$$

2.3.2 X-ray interactions

The X-ray tubes used in clinical radiological practice produce photons with energies between 0 and 140 keV. The three main interaction types with the human body in this case are Compton scattering, Rayleigh scattering and photoelectric effect. In the case of the latter, a photon is absorbed by the target atom and transfers all its energy to it. In this way the atom makes a transition to an excited state where a photoelectron leaves the target. In comparison with the mean free path of a photon, this photoelectron does not travel far. Therefore, stating that all the energy of the photon is deposited at the interaction site where the photoelectric effect took place, is a reasonable assumption [14]. Compton scattering occurs when only part of the energy of the incident photon is absorbed by the target atom. As a consequence, a secondary photon with a reduced energy leaves the site of interaction. In the case of Rayleigh scattering, the incident photon is deflected by the target atom without any energy deposition [16].

The type of event that occurs is a discrete random variable, with probabilities depending on the total cross sections of the different interaction mechanisms. The total cross section σ is an effective area that quantifies the likelihood of a scattering event, given a certain beam quality and target object. The cross sections of the various interaction processes are obtained from approximate theoretical calculations and from experimental results. The most extensive tables of atomic photoelectric cross sections are those of the Evaluated Photon Data Library (EPDL97) of Cullen et al [17]. In addition, cross sections for scattering and photoelectric absorption are tabulated in the XCOM Photon Cross Section Database [18].

2.3.3 Scattering angle and energy loss

In addition to the total cross section, each interaction mechanism is characterized by corresponding differential cross sections (DCSs). A DCS determines the probability distribution of the various quantities related to the interaction process, such as the energy loss and the angular deflection of the particle [16].

In the case of a Compton or Rayleigh interaction, the incident photon is scattered under a certain solid angle $\Omega(\theta, \varphi)$. The DCS $d\sigma/d\Omega$ quantifies the rate at which scattered

particles can be detected at a given angle. Azimuthal symmetry is assumed, meaning that the DCS is independent of the azimuthal scattering angle φ . Therefore, φ is uniformly distributed between 0 and 2π [14]:

$$p(\varphi) = \frac{1}{2\pi} \quad \text{and} \quad \varphi = 2\pi\xi$$

The polar angle θ , on the other hand, can be sampled from $d\sigma/d\Omega$, knowing the energy of the incident photon. Figure 2.6 depicts the Compton scattering angular distributions in water for 3 different photon energies.

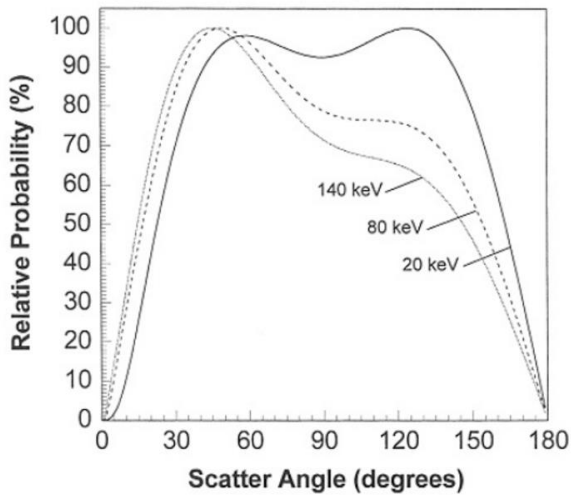


Figure 2.6 Differential cross sections $d\sigma/d\Omega$ for Compton scattering of photons in water. The probabilities are given for 3 X-ray energies. As the energy of the X-rays increases, the photons are more likely to be scattered forward [15].

The energy-loss DCS $d\sigma/dW$ quantifies the rate at which scattered particles can be detected with a given energy. The energy loss of the scattered photon can be sampled from $d\sigma/dW$.

2.3.4 Monte Carlo transport codes

Several MC codes are available for the simulation of photon transport in matter. A few examples are FLUKA [19,20], PENELOPE [21,22], ImpactMC [23-25], EGSnrc [26] and MCNP [27]. In all existing codes, the simulation of photon histories is performed by using a detailed scheme, in which all interactions undergone by the transported photons are simulated in chronological succession [16]. A photon history terminates after a photoelectric event or after a couple Compton interactions. In this way, the number of histories in each track is relatively small (< 10). Therefore, with present-day computational powers, a small enough uncertainty can be reached by simulating $>10^9$ during a couple of hours.

In this thesis, MC simulations were performed with ImpactMC [28]. The software was validated before in the literature [23-25]. Quantitative CTDI measurements at various scan conditions were performed in cylindrical PMMA phantoms of different sizes. The simulated values were within 7.6% of the measured values. Knowing that the ionization chamber used (CT chamber type 30009 with Unidos electrometer, PTW, Germany) gives results within $\pm 5\%$ in the range of 50 to 150 kV, the simulated and measured values can be considered in good agreement [24]. The validation experiments were repeated in our lab with comparable results.

An important feature of the ImpactMC software is the use of a patient-specific voxel geometry. This 3D model is created, based on the clinically available CT data of the examined patient. The input volume consists of a three dimensional grid of voxels and can be provided in DICOM format. The characteristics of the CT system and scan protocol used have to be specified in the input file. For a helical scan, these include:

- X and Y coordinates of the centre of rotation (COR)
- Distance between COR and X-ray focal spot
- In-plane fan angle of the X-ray beam
- Total beam collimation, measured at the axis of rotation
- Table feed
- Starting angle and starting Z position
- Rotation time and number of rotations
- X-ray spectrum
- Shaping filter

The X-ray spectrum and shaping filter of the Siemens Somatom Definition Flash are predefined in the software. Automatic and organ-based tube-current modulation can be incorporated, by specifying a tube current value for each simulated projection.

The Monte Carlo simulation characteristics are:

- Break energy, energy level below which a photon is not traced anymore (10 keV)
- Maximum number of interactions considered for one photon (10)
- Number of projections per rotation
- Simulation time

A photon track ends if the energy of the particle is below 10 keV or the maximum number of interactions is reached. In either case, the remaining photon energy is deposited within the voxel of the last interaction site. The simulations in this PhD thesis were performed on a 64-bit Windows 7 desktop with an Intel Core i7-2600 CPU @ 3.40 GHz and 12 GB RAM. A NVIDIA GeForce GTX 580 with 3 GB VRAM was installed. The simulations were set to end after 1 hour. The number of photon histories over the entire 3D volume during one simulation was in the order of 10^{10} .

To calibrate the software, air kerma values were measured free-in-air in the isocenter of the CT gantry for one rotation. The measurements were performed with a pencil ionisation chamber (Xi CT detector, Raysafe, Sweden) and included the same X-ray spectrum and shaping filter as the simulated scans. The values are used to scale the dose distributions to absolute values.

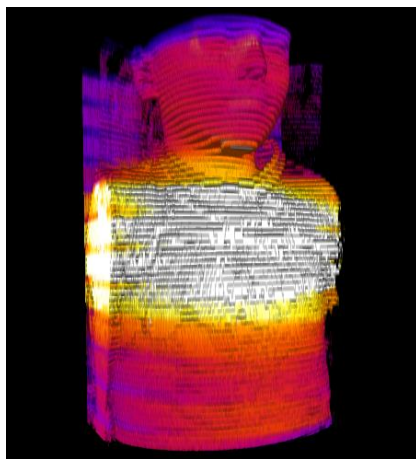


Figure 2.7 ImpactMC [28] makes it possible to simulate CT examinations. A patient-specific voxel model is created, using the DICOM images of the patient's CT scan. In this way, a 3D voxelized dose distribution can be calculated.

With ImpactMC, CT scans of examined patients can be simulated to calculate the dose distribution in the body (Figure 2.7). More specific, the obtained 3D dose distribution makes it possible to assess the dose in each voxel and to determine patient-specific organ and tissue doses.

2.4 RISK ESTIMATION

Substantial evidence exists that exposure to high levels of ionizing radiation (100 mSv to 2.5 Sv) can cause illness or death. Data from atomic bomb survivors proves that high doses are connected to the development of cancer, heart disease, stroke and mental retardation in the children of exposed mothers. However, little epidemiologic data is available for lower doses, involved in diagnostic radiology (less than 100 mSv) [29].

For the radiation doses at which excess cancers occur in the Hiroshima and Nagasaki studies, the induction of solid tumours in general follows a positive linear trend with increasing dose [30]. International committees as the International Commission on Radiological Protection (ICRP) and the Biological Effects of Ionizing Radiation (BEIR) committee concluded that the risk would continue in a linear fashion at lower doses, without a threshold. The smallest dose has the potential to cause a small risk increase in humans. According to the abovementioned committees, this linear-no-threshold model (LNT) provides the most reasonable description of the relation between low-dose exposure to ionizing radiation and the incidence of radiation-induced cancers [31]. Risk estimations at low doses (< 100 mGy) remain subject of debate. Several studies challenge the assumption that the biological responses at high and low exposures are proportional with radiation dose [32-34]. Possible dose-response relations described by [29] are depicted in Figure 2.8. The LNT model could both underestimate (curve b) or overestimate (curves c-e) the risk to low dose radiation. Curve d reflects a dose threshold below which the risk of cancer induction is zero, whereas curve e even depicts a hormetic response. The latter would mean that a given amount of radiation dose would reduce the background incidence for some cancers.

Based on individual organ dose estimates, the radiation induced risk to the patient resulting from a CT examination can be quantified. In Chapters 3 and 4 of this PhD thesis, the model proposed by the BEIR VII publication was used, resulting in the estimation of lifetime attributable risks (LAR) [31]. Age-dependent cancer incidence (and mortality) rates for males and females were applied. According to this model, approximately 1 person in 1000 in the total population would be expected to develop cancer from a dose of 10 mSv above background, either in a solid form or leukaemia. According to Kalender, this is comparable with an abdominal CT examination [12].

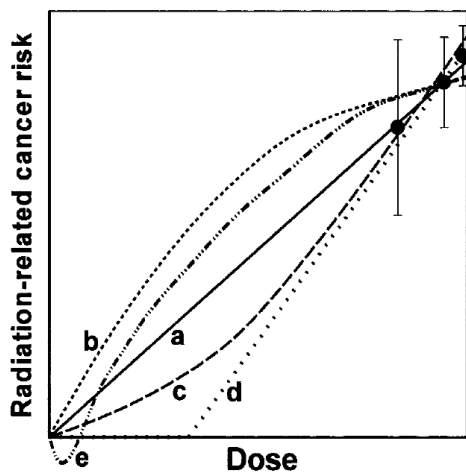


Figure 2.8 Different possible extrapolations of radiation risks associated with high dose epidemiological data down to very low doses. Curve a accords to the linear-non-threshold model; curve b: hypersensitivity; curve c: hyposensitivity; curve d: threshold assumption; curve e: hormetic [29].

2.5 REFERENCES

- 1 McCollough CH, Leng S, Yu L, Cody DD, Boone JM, McNitt-Gray MF (2011) CT dose index and patient dose: they are not the same thing. *Radiology* 259:311-316
- 2 AAPM (2011) Size-specific dose estimates (SSDE) in pediatric and adult body ct examinations (Task Group 204).
- 3 AAPM (2014) Use of Water Equivalent Diameter for Calculating Patient Size and Size-Specific Dose Estimate (SSDE) in CT (Task Group 220).
- 4 (2014) The Alderson RANDO phantom. RSD Radiology Support Devices. Available via http://rsdphantoms.com/rt_art.htm
- 5 International Commission on Radiation Units and Measurements. (1989) Tissue substitutes in radiation dosimetry and measurement. International Commission on Radiation Units and Measurements, Bethesda, Md., U.S.A.
- 6 (2005) MTS-N. TLD Poland. Available via <http://www.tld.com.pl/tld/mts.html>
- 7 Kramer R (1986) The Calculation of dose from external photon exposures using reference human phantoms and Monte Carlo methods. Gesellschaft für Strahlen- und Umweltforschung, München
- 8 Jones DG, Shrimpton PC (1991) Survey of CT Practice in the UK. Part 3: normalised organ dose calculation using Monte Carlo techniques. NRPB-R250.
- 9 Jones DG, Shrimpton PC (1993) Normalized organ doses for X-ray computed tomography calculated using Monte Carlo techniques. NRPB SR-250.
- 10 Zankl M, Panzer W, Drexler G (1991) The calculation of dose from external photon exposures using reference human phantoms and Monte Carlo methods, Part VI: organ doses from computed tomography examinations. GSF Report 30/91.
- 11 Zankl M, Panzer W, Drexler G (1993) Tomographic anthropomorphic models, part II: organ dose from computed tomographic examinations in paediatric radiology; GSF Report 30/93.
- 12 Kalender WA (2014) Dose in x-ray computed tomography. *Phys Med Biol* 59:R129-150
- 13 Franck C, Vandevoorde C, Goethals I et al (2016) The role of Size-Specific Dose Estimate (SSDE) in patient-specific organ dose and cancer risk estimation in paediatric chest and abdominopelvic CT examinations. *Eur Radiol* 26:2646-2655
- 14 Salvat F (2015) Penelope-2014 A Code System for Monte Carlo Simulation of Electron and Photon Transport. OECD, Barcelona, Spain
- 15 Beutel J (2000) Handbook of medical imaging. SPIE Press, Bellingham, Wash.
- 16 Salvat F, Fernandez-Varea JM (2009) Overview of physical interaction models for photon and electron transport used in Monte Carlo codes. *Metrologia* 46:S112-S138
- 17 (1997) EPDL97 The Evaluated Data Library. 6
- 18 Berger M, Hubbell J, Seltzer S et al (2005) XCOM: Photon Cross Sections Database. National Institute of Standards and Technology, Gaithersburg. Available via <http://www.nist.gov/pml/data/xcom/index.cfm>
- 19 Ferrari A, Sala P, Fasso A, Ranft J (2005) FLUKA: A Multiple-particle Transport Code. CERN
- 20 Bohlen T, Cerutti F, Chin M et al (2014) The FLUKA code: Developments and Challenges for High Energy and Medical Applications. *Nuclear Data Sheets* 120:211-214

- 21 Sempau J, Acosta E, Baro J, FernandezVarea JM, Salvat F (1997) An algorithm for Monte Carlo simulation of coupled electron-photon transport. Nucl Instrum Meth B 132:377-390
- 22 Baro J, Sempau J, Fernandezvarea JM, Salvat F (1995) PENELOPE: An algorithm for Monte Carlo simulation of the penetration and energy-loss of electrons and positrons in matter. Nucl Instrum Meth B 100:31-46
- 23 Schmidt B, Kalender WA (2002) A fast voxel-based Monte Carlo method for scanner- and patient-specific dose calculations in computed tomography. Phys Med 18:43-53
- 24 Deak P, van Straten M, Shrimpton PC, Zankl M, Kalender WA (2008) Validation of a Monte Carlo tool for patient-specific dose simulations in multi-slice computed tomography. Eur Radiol 18:759-772
- 25 Chen W, Kolditz D, Beister M, Bohle R, Kalender WA (2012) Fast on-site Monte Carlo tool for dose calculations in CT applications. Med Phys 39:2985-2996
- 26 (2001) The EGSnrc code system: Monte Carlo simulation of electron and photon transport. . Technical Report PIRS-701
- 27 (1993) MCNP - A General Monte Carlo N-particle Transport Code. Los Alamos National Laboratory Report
- 28 ImpactMC 1.3.1. CT Imaging, Erlangen, Germany
- 29 Brenner DJ, Doll R, Goodhead DT et al (2003) Cancer risks attributable to low doses of ionizing radiation: assessing what we really know. Proc Natl Acad Sci U S A 100:13761-13766
- 30 Preston DL, Shimizu Y, Pierce DA, Suyama A, Mabuchi K (2003) Studies of mortality of atomic bomb survivors. Report 13: Solid cancer and noncancer disease mortality: 1950-1997. Radiat Res 160:381-407
- 31 Council N (2006) Health risks from exposure to low levels of ionizing radiation: BEIR VII phase 2. The National Academies Press
- 32 Averbeck D (2009) Does scientific evidence support a change from the LNT model for low-dose radiation risk extrapolation? Health Phys 97:493-504
- 33 Grudzenski S, Raths A, Conrad S, Rube CE, Lobrich M (2010) Inducible response required for repair of low-dose radiation damage in human fibroblasts. Proc Natl Acad Sci U S A 107:14205-14210
- 34 Tubiana M, Feinendegen LE, Yang C, Kaminski JM (2009) The linear no-threshold relationship is inconsistent with radiation biologic and experimental data. Radiology 251:13-22

Chapter 3

Dose reduction technologies in CT

The best approach for reducing patient radiation exposure is avoiding unnecessary CT examinations and minimizing multiphase scanning. Before prescribing the patient a CT examination, other techniques like ultrasound (US) and magnetic resonance imaging (MR) should be considered. According to the ICRP, the use of ionizing radiation should result in a sufficient benefit to offset the detriment it causes [1]. However, since CT is a non-invasive diagnostic tool, often a CT scan appears to be necessary to answer a clinical question. Therefore, care must be taken to keep the dose as low as reasonably achievable.

Retakes because of patient movement, scanning the wrong anatomic region or loss of the images when switching hospitals are unnecessary exposures which must be avoided. Furthermore, the scan range should be strictly limited to the region of interest. Avoiding exposures at 140 kVp, except for obese patients, and limiting the tube voltage to 100 kVp for children is a positive evolution in clinical practice. The last years, CT manufacturers have developed a number of radiation dose reduction tools to limit the exposure to the patient even further.

3.1 AUTOMATIC EXPOSURE CONTROL

A large diversity exists in attenuation along the scan direction of the patient. To achieve the same noise level, the abdomen will require more exposure than the neck (Figure 3.1). Moreover, strong variations in radiation absorption occur in the transverse plane, as the tube rotates around the patient; particularly in regions that are elliptical in shape, such as the thorax and the pelvis [2]. For these structures, the attenuation is higher in the lateral direction, compared to the antero-posterior direction (Figure 3.2). Hence, scanning the patient with a fixed tube current will result in an inhomogeneous photon flux at the

detector. Depending on the required diagnostic noise level, the tube current will be determined by the most attenuating region of the scanrange. Therefore, less attenuating regions will receive unnecessary radiation dose. In addition, the reconstructed images will have different noise levels.

Modulation of the X-ray tube current is an effective dose managing method [3]. The dose to the patient can be reduced in less-attenuating or smaller anatomical regions. Lowering the exposure in less-attenuating regions, will lead to an equalized photon flux to the detector for all projections. In this way, similar image quality levels are obtained in all reconstructed images.

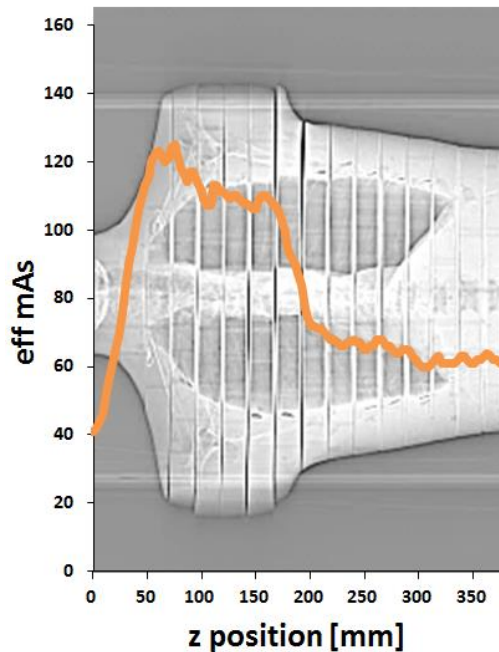


Figure 3.1 Modulation of the X-ray tube current along the length of the patient is an effective dose reducing method. The highest mAs_{eff} values are selected in the shoulder region. However, less attenuation occurs in the neck and the lower thorax. Therefore, the tube current can be reduced in these parts of the patient [4].

There are important differences among CT vendors in the implementation of automatic exposure control systems. Each manufacturer uses another method to define the image quality in the user interface (Table 3.1). In addition, the minimum acceptable image quality differs. A recommended setting is provided, though the user can choose an alternative. To determine the required tube current values, some systems use the attenuation values of only one scan projection radiograph (SPR). Others can combine the data of two orthogonal SPRs. Furthermore, the strength of the modulation algorithms used varies.

Siemens' Care Dose 4D (Siemens Healthcare, Forchheim, Germany) uses the *topogram* to modulate the tube current in the angular and longitudinal directions. Attenuation values and dimensions measured on the topogram(s) are used to determine the size and density of the patient. If only one SPR is available, the attenuation for the complementary projection is estimated taking into account the examined anatomical region and the patient's contour [2]. Next, the exposure values are calculated to ensure the required image quality, given by the *quality reference mAs (QRM)*. This metric is equal to the effective mAs that produces the desired image quality on a standard-sized patient. To provide an image quality consistent with that obtained using the QRM level for a standard-sized patient, the tube current must be modulated to compensate for variations in patient size and attenuation. During the scan, the system will perform on-line feedback loops to fine-tune the predicted tube current values. The transmission values at a given angle are used to optimize the tube current for the projection that will occur 180° later [4].

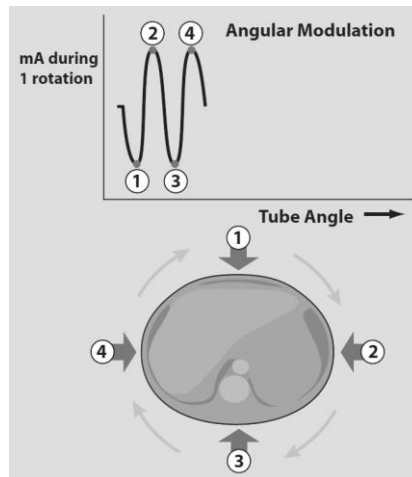


Figure 3.2 Modulation of the X-ray tube current in the transverse plane of the patient can be used as a technique to reduce the dose to the patient. Because of the elliptical shape of the human body, the attenuation in the LAT directions (2 and 4) will be higher compared to the AP directions (1 and 3). Therefore, tube current values can be lowered during the AP projections [5].

SmartmA from **GE** (GE Healthcare, Milwaukee, Wisconsin) only uses the last *scout view* to determine the exposure values. Based on the selected *noise index*, the system computes the required mA values to be used. The noise index value will approximately equal the standard deviation in the central region of the image when a uniform phantom (with the patient's attenuation characteristics) is scanned and reconstructed using the standard reconstruction algorithm. During the scan, on-line adjustment of the predicted tube current values is not possible [5].

Toshiba's Sure Exposure 3D (Toshiba Corporation, Tokyo, Japan) converts the attenuation values of the *scanogram* into water-equivalent thicknesses. In this way, the tube current is modulated to ensure a given image quality, determined by the selected *target noise*, similar to GE's noise index. The obtained exposure values cannot be adjusted during the scan.

Philips CT scanners (Philips Medical Systems, Andover, Massachusetts) are able to modulate the tube current either in the longitudinal (Z-DOM) or the angular (D-DOM) direction. However, both features cannot be used together. D-DOM is carried out online during the scan. The projection data from the previous angles are used to predict the tube current values in the next rotation. A *reference image* from a satisfactory patient exam is stored on the scanner and is used as an image quality metric. Based on the *surview*, mA values are calculated by Z-DOM to provide an image quality consistent with that of the reference image.

The effect of the SPR and the scan direction for different vendors is evaluated in Chapter 6 of this PhD work.

Table 3.1 Image quality metrics used by different manufacturers for the implementation of ATCM.

manufacturer	ATCM	IQ metric
Siemens	CARE Dose 4D	Quality reference mAs
GE	SmartmA	Noise Index
Toshiba	Sure Exposure 3D	Target Noise
Philips	Z-DOM, D-DOM	Reference image

3.2 ORGAN-BASED TUBE CURRENT MODULATION

A particular modification of angular tube current modulation is implemented by Siemens and GE (Table 3.2). Instead of adjusting the exposure in the axial plane to the size of the patient, X-CARE reduces the mA during the anterior third of the tube rotation (120°). In this way, the dose to superficially located organs is reduced. This is particularly interesting for the eyes, thyroid, breasts and testes as these are radiosensitive organs. Because of the

decreased tube current, the amount of photons reaching the detector will be lower and the image quality will deteriorate. Therefore, to preserve image quality, the exposure is increased during the lateral and posterior projections [6]. Figure 3.3 displays the relative distribution of mA values as the X-ray tube rotates around the patient.

Table 3.2 Organ-based tube current modulation aims to lower the dose to anterior organs.

manufacturer	organ-based tube current modulation
Siemens	X-CARE
GE	Organ Dose Modulation
Toshiba	-
Philips	-

For women undergoing a chest CT in supine position, care must be taken to position the breasts. In the study of Taylor et al, no woman had all breast tissue located within the reduced-current zone [7]. The use of a metal-free brassiere during the scan can help positioning the breasts in the reduced-dose zone. Furthermore, scanning the patients in prone position will lead to more centrally located breasts. Nevertheless until now, changing the location of the reduced-current zone is not possible. The mA can only be lowered during the upper positions of the X-ray tube. In Chapter 8 of this PhD dissertation the concept of organ-based tube current modulation is critically evaluated.

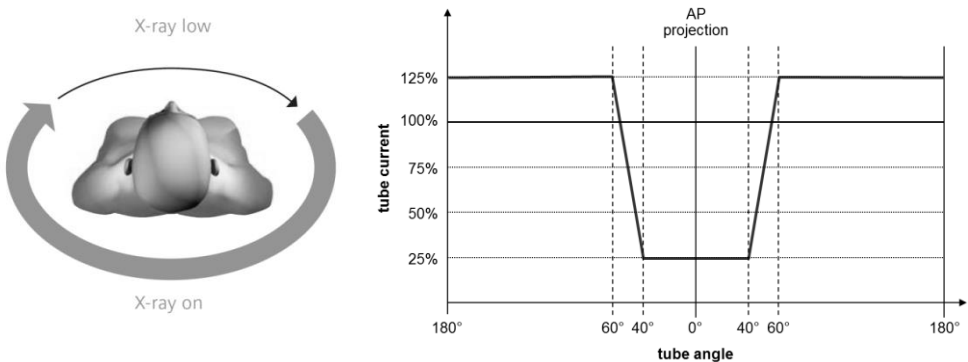


Figure 3.3 X-Care reduces the dose to anteriorly located organs by lowering the tube current during the anterior third of the rotation in the axial plane (120°). To maintain image quality, the tube current is increased during the lateral and posterior third of the body circumference. Relative mA values are shown, normalized to the average tube current during one rotation [8].

3.3 PEAK KILOVOLTAGE OPTIMIZATION

To further reduce the radiation dose to the patient, an automatic selection of the tube potential can be applied. If all other parameters are kept constant, reducing the tube voltage will significantly decrease the radiation dose. The dose to the patient changes roughly with the square of the tube potential [9]. For example, decreasing the tube voltage from 120 to 100 kVp while scanning the patient with a fixed tube current, will result in a dose reduction of 33%. In addition, the relative attenuation of iodine increases as the kVp is decreased. Because the influence of the photoelectric effect becomes more important at lower kVp's, the tissue contrast in the image will improve, even without changing the dose of contrast administered [10]. However, due to the higher absorption of low-energy photons by the patient, the images will contain more noise [11]. Image noise will increase in a non-linear fashion, resulting in a decreased contrast-to-noise ratio (CNR). As a result, when a lower kVp is selected, tube current values must typically be increased to preserve image quality [9].

The dose reducing effect of using a lower kVp is highly dependent on the size of the patient and the diagnostic task [12]. When the patient is too large, the benefit of the improved contrast is negated by the increased level of noise. In this case, the lower tube voltage reduces the image quality compared to a higher tube potential with the same dose. However, if the patient size is below a particular threshold, dose reduction or image quality improvement at the same CTDI can be achieved [11]. Maximum dose savings are seen with CT angiographic studies. Reducing the kVp brings the tube potential closer to the k-edge of iodine, resulting in an increased relative attenuation of the contrast agent. In this way, the CNR will be preserved, despite the increase in image noise, resulting in a significant dose reduction. The dose reducing effect of a lower tube voltage is smaller in non-contrast studies. Here, the improvements in tissue contrast are much less evident and larger compensatory increases in mAs are required to reduce image noise [10].

Table 3.3 Automatic selection of the tube potential is an effective dose reducing tool used by different manufacturers.

manufacturer	automatic kVp selection
Siemens	Care kV
GE	kV Assist
Toshiba	Sure kV
Philips	-

The idea of peak kilovoltage optimization is implemented by all major CT vendors, except Philips (Table 3.3). These tools optimize the dose efficiency without much user interactions. Based on the scanned projection radiograph, the total tissue attenuation along the z-axis of the patient is determined. Next, the tube current values are calculated that would be required for each kVp, taking into account the desired image quality and the amount of contrast agent used. The software then determines which combination of kVp and mAs will result to the lowest patient dose in terms of CTDI [10]. The optimal tube voltage is the one that uses the minimum radiation dose to achieve the desired image quality [12].

3.4 ITERATIVE RECONSTRUCTION

In CT, the traditional reconstruction method is the filtered back projection (FBP), which is relatively sensitive to noise and artefacts. This commonly used algorithm is based on only a single reconstruction. Before the raw data is back projected, a filter is applied with an emphasis on either low or high spatial frequencies. A trade-off between noise and resolution had to be made.

Iterative reconstruction (IR) methods on the other hand, can reduce noise while preserving spatial resolution. As a result, radiation exposures can be lowered to achieve the same image quality as with FBP. The dose reducing potential of IR is dependent on the iterative strength and the initial scan parameters. Dose savings ranging from 27% to 80% are reported in the literature [13,14]. IR algorithms use multiple repetitions in which the current solution converges towards a better image. A schematic overview of the iteration process is given in Figure 3.4. The IR loop starts with an empty image or using prior information from a standard FBP reconstruction. The better the initial images match the object, the faster the loop converges towards a stable solution. Next, a forward projection of the initial image is performed and the artificial raw data is compared to the real measured raw data. A correction term is computed and back projected onto the current image estimate. In this way, the current image estimate is updated and a new iteration is started. The loop is finished when the update for the current image estimate is considered small enough or a fixed number of iterations is reached. In addition, a predefined quality criterion can lead to an early loop exit [15]. Despite the computational demands, the computing power available in a modern processor makes it possible to have reconstruction times acceptable for the clinical workflow. The images obtained by IR are often described as plastic or cartoon-like. This can be overcome by blending the IR output with the original FBP image.

In addition, statistical IR may further reduce the noise in the image, by modelling the photon counting statistics during the acquisition. Projection rays of regions with high attenuation will contain less signal and therefore a higher statistical uncertainty (more

noise). By applying an adaptive denoising algorithm to the raw data, low weight is assigned to projection data with high statistical uncertainty and high weight to data with low statistical uncertainty. In other words, regions with higher attenuation are filtered more strongly compared to regions with lower attenuation [14,16].

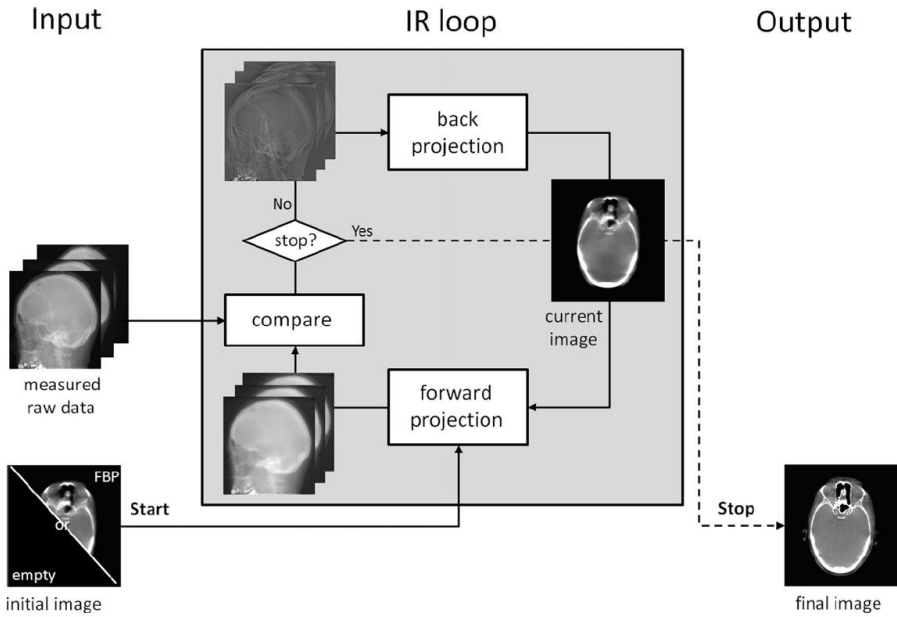


Figure 3.4 Schematic view of the iterative reconstruction method. The current image estimate is forward projected to create artificial raw data. By comparing the artificial and measured raw data, an updated image is computed which subsequently is back projected to the current image estimate. The loop can be started with an empty image or a FBP reconstruction. If a stop criterion is reached, the loop is terminated and the current image estimate becomes the final reconstructed image [15].

The classical FBP and the IR methods described above all assume a point focal spot, a point detector and a monochromatic pencil beam. Model-based IR (MBIR) methods represent the next level of complexity. They are based on the real dimensions of the focal spot and the detector elements. Furthermore, these algorithms may include models of the X-ray beam spectrum, the photon interactions with matter and the imaged object. In this way, imperfect acquisition conditions and artefacts are considered to modify the synthesized images more accurately. However, this comes with a cost of computational

time [17]. An overview of the different iterative methods currently available is given in Table 3.4.

Table 3.4 Overview of the available iterative reconstruction methods.

manufacturer	iterative method	statistical iteration	model-based iteration
Siemens	IRIS	SAFIRE	ADMIRE
GE		ASiR	ASiR-V, Veo
Toshiba	AIDR, AIDR+	AIDR 3D	FIRST
Philips		iDose	IMR

3.5 ADAPTIVE Z-COLLIMATION

A significant dose contribution during spiral CT procedures is due to the z-overscanning effect, as described in Chapter 1. For single-detector row scanners, overscanning is considered negligible. However, the effect increases with the number of detector rows. A promising dose saving method is the concept of adaptive z-collimation. Parts of the X-ray beam exposing tissues outside the volume of interest are blocked, by dynamically adjusted collimators at the start and end of the CT scan (Figure 3.5). The idea of adaptive z-axis collimation is implemented by all major CT vendors (Table 3.5).

Table 3.5 Overview of the different adaptive z-collimation techniques used by CT vendors.

manufacturer	adaptive z-collimation
Siemens	Adaptive Dose Shield
GE	Dynamic Z-axis tracking
Toshiba	Active collimation
Philips	Eclipse DoseRight collimator

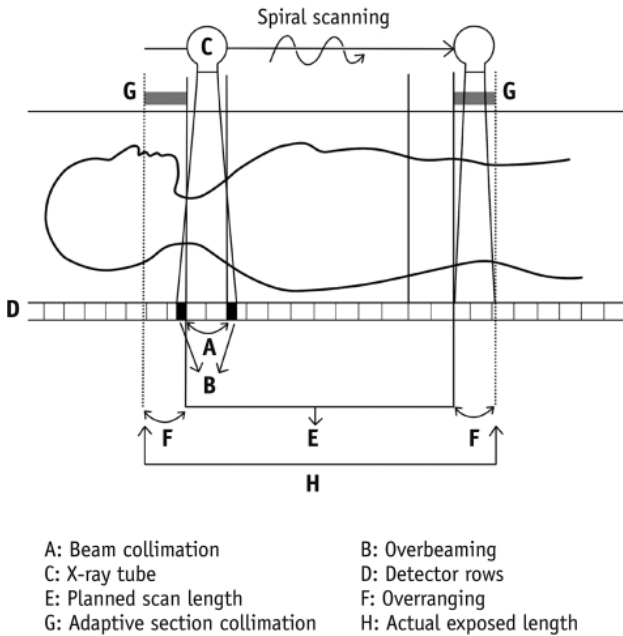


Figure 3.5 By the independent movement of both collimator blocks the overscanning effect is limited [18].

3.6 OTHER DOSE REDUCING TECHNIQUES

Dual-energy CT (DECT) imaging consists in the acquisition of two spectrally distinct attenuation datasets from the same region of interest. A low-energy dataset is acquired at 80 kVp, while a high-energy dataset is acquired at 140 kVp. Current commercially CT scanners use either a dual X-ray source/detector system, each operated at different peak tube potentials or a single X-ray source/detector system. Using only one X-ray tube, a fast kVp switching technique permits that 1/3 of the projections are obtained at 140 kVp, while the rest of the projections are obtained at 80 kVp. Another approach is the use of a single source, but a dual layer of energy-sensitive detectors to identify both low- and high-energy photons simultaneously. With the use of DECT, multiple monochromatic image datasets can be reconstructed. The higher informational content and post-processing flexibility of DECT opens up a dose-saving potential for virtual non-contrast imaging. Many CT exams involve both non-contrast and contrast-enhanced scans. Dual-energy imaging allows the creation of virtual non-contrast images from a post-contrast DECT scan. In this way, the non-contrast scan can be omitted [19].

The detector system is the key component in a CT scanner. Its task is to convert the incoming photons into an electrical signal that can be fed into the image reconstruction

chain. Important properties are high quantum efficiency, large dynamic range and fast signal decay. Conventional CT detectors are solid-state detectors, which uses a two-step process to convert the incoming X-ray intensities into an electric signal. First, the X-rays are converted into visible light in a scintillator layer. Next, the emitted light is converted into an electric current by a photodiode array. In this process, leakage of the scintillation light between adjacent detector pixels will cause optical cross-talk and reduce the sharpness of the reconstructed image. Great expectations have been set for photon-counting detectors (PCDs) due to their potential in dose reduction. They are made of semiconductor materials and are able to directly convert the incoming X-rays into electric signal pulses. In addition, the photon counts can be recorded in multi-energy windows. Although PCDs have not yet been implemented in clinical practice, they can offer a better spatial resolution and the capability to further reduce dose because of their improved quantum efficiency, compared to conventional solid-state detectors [20].

3.7 REFERENCES

- 1 ICRP (2000) Managing Patient Dose in Computed Tomography. ICRP publication 87. Ann ICRP 30
- 2 Rego SL, Yu L, Bruesewitz MR, Vrieze TJ, Kofler JM, McCollough CH (2008) CARE Dose4D Automatic Exposure Control System: Physics Principles and Practical Hints. Mayo Foundation for Medical Education and Research
- 3 McCollough CH, Bruesewitz MR, Kofler JM, Jr. (2006) CT dose reduction and dose management tools: Overview of available options. Radiographics 26:503-512
- 4 Franck C, Bacher K (2016) Influence of Localizer and Scan Direction on the Dose-Reducing Effect of Automatic Tube Current Modulation in Computed Tomography. Radiat Prot Dosimetry. 10.1093/rpd/ncw077
- 5 Bruesewitz MR, Yu L, Vrieze TJ, Kofler JM, McCollough CH (2008) Smart mA - Automatic Exposure Control (AEC): Physics Principles and Practical Hints. Mayo Foundation for Medical Education and Research
- 6 Duan X, Wang J, Christner JA, Leng S, Grant KL, McCollough CH (2011) Dose reduction to anterior surfaces with organ-based tube-current modulation: evaluation of performance in a phantom study. AJR Am J Roentgenol 197:689-695
- 7 Taylor S, Litmanovich DE, Shahrzad M, Bankier AA, Gevenois PA, Tack D (2015) Organ-based tube current modulation: are women's breasts positioned in the reduced-dose zone? Radiology 274:260-266
- 8 Siemens Healthcare, Germany
- 9 Gnannt R, Winklehner A, Eberli D, Knuth A, Frauenfelder T, Alkadhi H (2012) Automated tube potential selection for standard chest and abdominal CT in follow-up patients with testicular cancer: comparison with fixed tube potential. Eur Radiol 22:1937-1945
- 10 Raman SP, Johnson PT, Deshmukh S, Mahesh M, Grant KL, Fishman EK (2013) CT dose reduction applications: available tools on the latest generation of CT scanners. J Am Coll Radiol 10:37-41
- 11 Yu L, Li H, Fletcher JG, McCollough CH (2010) Automatic selection of tube potential for radiation dose reduction in CT: a general strategy. Med Phys 37:234-243
- 12 Bruesewitz MR, Yu L, Leng S et al (2011) Automatic kV Selection for Radiation Dose Reduction in CT: How Does it Work and What Can it Do? Mayo Foundation for Medical Education and Research
- 13 De Crop A, Smeets P, Van Hoof T et al (2015) Correlation of clinical and physical-technical image quality in chest CT: a human cadaver study applied on iterative reconstruction. BMC Med Imaging 15:32
- 14 Geyer LL, Schoepf UJ, Meinel FG et al (2015) State of the Art: Iterative CT Reconstruction Techniques. Radiology 276:339-357
- 15 Beister M, Kolditz D, Kalender WA (2012) Iterative reconstruction methods in X-ray CT. Phys Med 28:94-108
- 16 Kachelriess M, Watzke O, Kalender WA (2001) Generalized multi-dimensional adaptive filtering for conventional and spiral single-slice, multi-slice, and cone-beam CT. Med Phys 28:475-490
- 17 Seibert JA (2014) Iterative reconstruction: how it works, how to apply it. Pediatr Radiol 44 Suppl 3:431-439

- 18 Goo HW (2012) CT Radiation Dose Optimization and Estimation: an Update for Radiologists. *Korean Journal of Radiology* 13:1-11
- 19 Halliburton S, Arbab-Zadeh A, Dey D et al (2012) State-of-the-art in CT hardware and scan modes for cardiovascular CT. *J Cardiovasc Comput Tomogr* 6:154-163
- 20 Wang S, Gao H, Zhang L, Wu D, Xu X (2017) Quasi-monochromatic imaging in x-ray CT via spectral deconvolution using photon-counting detectors. *Phys Med Biol* 62:2208-2223

Chapter 4

Image quality assessment in CT

The exposure to ionizing radiation from medical devices has gained more and more attention in the radiology department [1]. Efforts are made to track the absorbed dose to the patient and to keep these values within dose reference levels (DRLs). However, in order to optimize CT protocols and to keep the resulting doses as low as reasonably achievable (ALARA), image quality (IQ) should be taken into account as well. Depending on the clinical task, an optimal balance between patient dose and IQ must be pursued.

4.1 OBJECTIVE IMAGE QUALITY

CT is a three-dimensional imaging technique in which IQ assessment must be approached with caution. Objective IQ parameters typically use physical metrics, either in the spatial domain or in the frequency domain (Figure 4.1). This duality is due to the fact that some features produce overall responses which are independent of the location in the image, whereas others are spatially correlated [2].

Image signal or intensity (I) and image noise (SD) are key parameters in IQ evaluation. Noise is defined as fluctuations of image intensity values around their mean. Contrast, the mean signal difference between two objects, is the ability to detect intensity or grayscale differences. The contrast-to-noise ratio (CNR) or signal difference to noise ratio (SDNR) is frequently used in IQ assessment and is defined as:

$$CNR = \frac{I_1 - I_2}{SD}$$

Large-area spatial-domain metrics, e.g. noise, contrast and CNR, are easy to compute and provide practical figures of merit in certain cases. However, a more comprehensive set of parameters is required to describe the image statistics more profound.

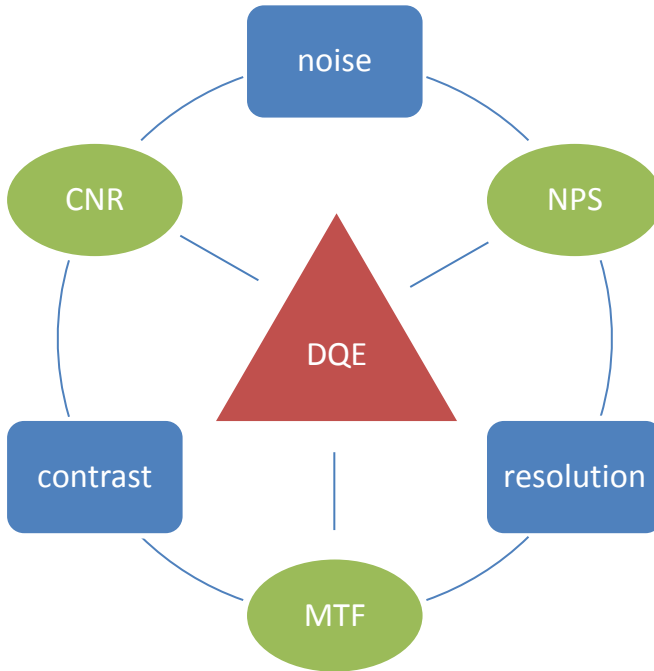


Figure 4.1 Objective image quality metrics used for CT image quality assessment (adapted from [3]).

Measuring the SD in a selected ROI provides only a simple estimate of the image noise level. It does not reflect the image texture, which has a significant effect on the perceived image look and quality. The noise power spectrum (NPS) gives a more complete description as it shows noise variance as a function of spatial frequency. In Figure 4.2 two images of the same homogeneous object are depicted. Coarse grain noise is present in the left image, while the image on the right contains fine grain noise. Although the appearance may be very different, both have equal standard deviations. By looking at the NPS, the differences in noise texture becomes clear. The first image results in the red NPS-curve, dominating the low spatial frequencies, while the black curve originates from the second image. In the latter, the NPS is shifted towards higher frequencies.

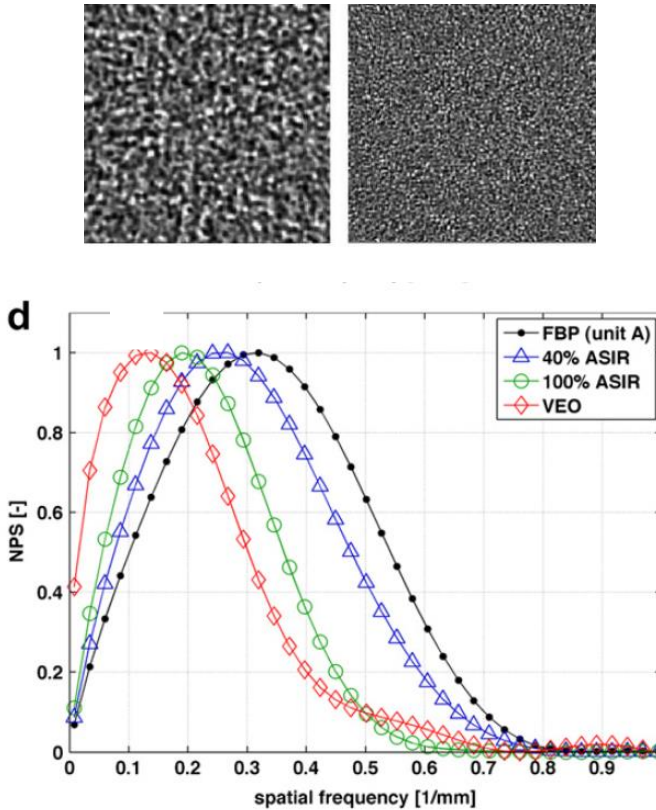


Figure 4.2 Top: two images of a homogenous object with the same SD. Bottom: The corresponding noise power spectra. The left image contains more low frequency noise (red NPS), while the high frequency noise dominates in the right image (black NPS) [4]

The spatial resolution or sharpness is related to the level of detail that can be seen in the image. It is defined as the ability to distinguish two separate objects and is directly linked to the pixel size, the reconstruction kernel, the focal spot size of the X-ray tube as well as the hardware properties of the detector [2]. It is possible to detect details which are smaller than the pixel size if the signal is large enough to significantly affect the gray value of that pixel. Resolution can be assessed in a simple way by counting the number of line pairs per mm in the image domain. However, this technique is biased by observer subjectivity and provides little information of system spatial resolution beyond a limiting value [5]. In the frequency domain, resolution is commonly estimated with the modulation transfer function (MTF). The MTF provides a measure of how well the system transfers contrast across spatial frequencies [6]. The curve is calculated from the point spread function (PSF), the response of the system to a metal bead in the spatial domain (Figure 4.3). In practical measurements, the point stimulus should be 5-10 times smaller than the

width of the detector element [7]. The higher the MTF, the better the spatial resolution. Typically, results of MTF calculations are expressed in a scalar form as MTF_{50} or MTF_{10} values, i.e. the frequencies at which the MTF drops to 50% or 10%.

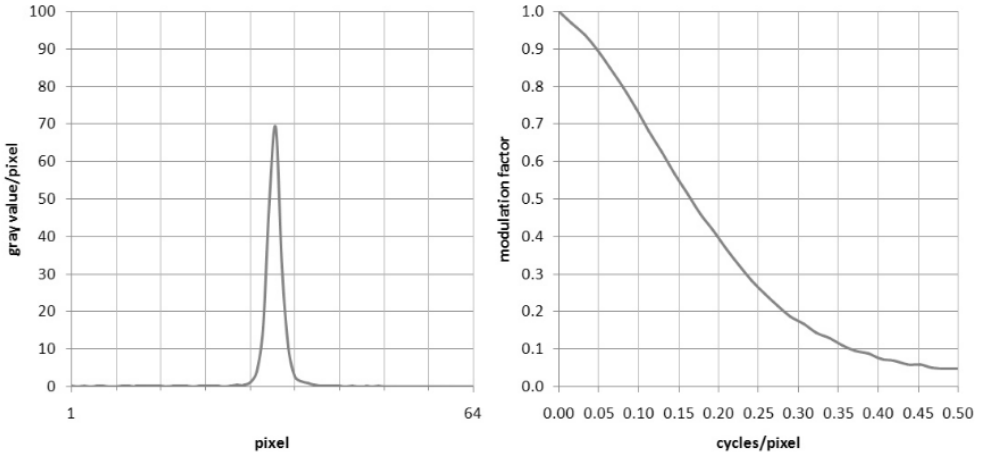


Figure 4.3 The modulation transfer function (right) is calculated from the Fourier transformation of the point spread function (left). It depicts how well the system transfers contrast across spatial frequencies.

For small objects, the contrast is strongly influenced by the spatial resolution. Approximately, contrast is related to the integral of the MTF squared [8]. The equivalent of the CNR in the frequency domain can be expressed as:

$$NEQ = \frac{MTF^2}{NPS}$$

This metric is called the noise-equivalent quanta (NEQ) and reflects the number of photons contributing to the image.

Finally, the detective quantum efficiency (DQE) describes the overall efficiency of a CT system by making the ratio between the number of photons used to generate an image (NEQ) and the incoming number of photons to the detector Q :

$$DQE = \frac{MTF^2}{NPS * Q}$$

The DQE describes the effectiveness of an imaging system, relative to an ideal detector. This quantity is of high importance since the radiation dose to the patient can only be kept

as low as possible if the DQE is made as close to unity as possible. DQE is widely used in medical imaging as a fundamental metric of detector performance.

4.2 SUBJECTIVE IMAGE QUALITY

During the development of CT technology, where performance between different units could vary drastically, the objective metrics described above were quite useful. However, the sensitivity of these methods is rather limited for newer systems, and the non-linearity of iterative reconstruction algorithms makes this approach difficult to implement [2]. Complementing the physical-technical parameters, the assessment by observers is a subjective way to evaluate the quality of an image.

Contrast-detail (CD) analysis is a conceptual visual method for combining the spatial resolution and contrast in the presence of noise. Visual analysis of low contrast detectability can be performed with a Catphan[®] phantom. The low contrast module (CTP515) contains supra-slice targets of different diameters and contrasts (Figure 4.4). Each contrast level (0.3, 0.5 and 1%) holds 9 inserts with decreasing diameters (15, 9, 8, 7, 6, 5, 4, 3 and 2mm).

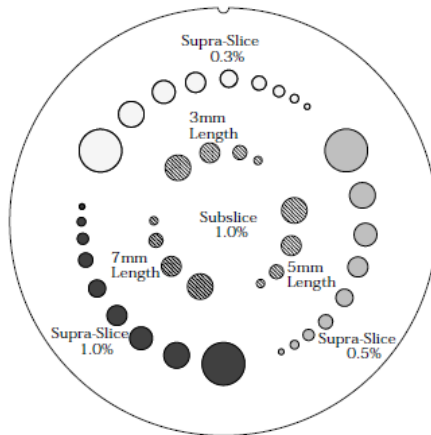


Figure 4.4 Low contrast module (CTP515) of the Catphan[®] phantom containing supra-slice contrast targets [9].

A human observer can determine the number of targets visible for each contrast level and a quantification of CD can be done by calculating the inverse image quality figure:

$$IQF_{inv} = \frac{100}{\sum_{i=1}^3 C_i * D_i}$$

D_i represents the smallest visible target at a given contrast level C_i . A completely invisible contrast level results in a D_i of 20mm.

Both clinical and phantom images can be assessed using the receiver operating characteristics (ROC) paradigm. When an observer is asked to detect a signal in an image, the response is a degree of belief that the signal is present: a low response value corresponds to the conviction that the signal is absent, whereas a high value denotes the conviction that the signal is present. If the detectability experiment is performed with a significant number of observers, the probability of a response can be plotted for those images that do not contain a signal and for those that do contain a signal (Figure 4.5). Next, a threshold (λ_c) is chosen above which a positive decision is made. The area under the signal-absent curve below λ_c is called the true negative fraction (TNF) or specificity. The true positive fraction (TPF) or sensitivity represents the area under the signal-present curve above the threshold. Changing λ_c changes the balance between sensitivity and specificity. Increasing one parameter leads to a decrease of the other. In the visualization of the ROC curve all possible combinations of TPF and false positive fraction (FPF = 1 - TNF) are plotted while λ_c changes from the lowest to the highest possible value. The area under the ROC curve is a concise description of the diagnostic performance of a system. The diagonal associated with pure guessing (worst performance) bisects the ROC box and the area under it is 0.5. Best performance corresponds to an area of 1.

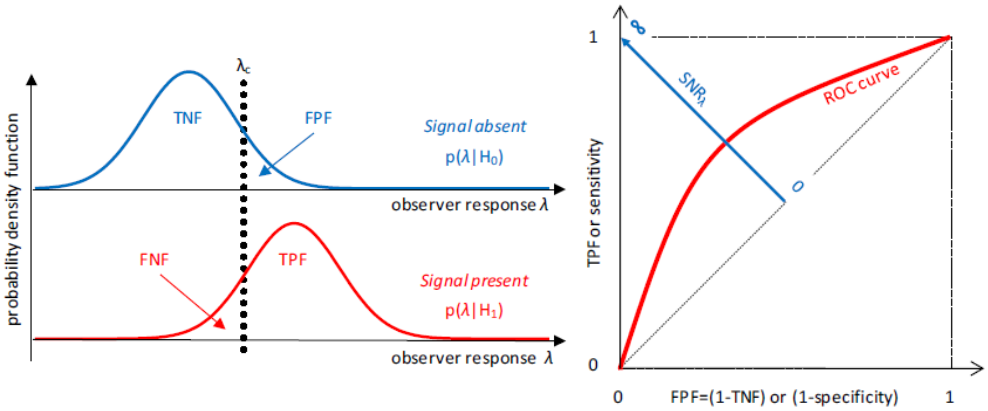


Figure 4.5 left: Probability density functions of the response to signal absent and signal present images. right: A ROC curve plots the true positive fraction (TPF or sensitivity) versus the false positive fraction (FPF or 1-specificity) [2].

To avoid the complexity associated with ROC experiments, more simplified methods have been developed. In Chapter 7 of this PhD work, an absolute Visual Grading Analysis (VGA) based on observer readings was used to assess the image quality of chest CT scans. Experienced radiologists were asked to score clinical datasets based on the European Guidelines for Quality Criteria for Computed Tomography [10]. Nine structures were rated on a four-level Likert scale, ranging from 1: the structure is not visible, to 4: the structure is very well reproduced. For each reader a VGA score (VGAS) was calculated:

$$VGAS = \frac{\sum G_{r,s}}{N_R N_S}$$

With N_S the number of structures, N_R the number of readers and $G_{r,s}$ the individual ratings of a given reader for a particular structure. A visual grading analysis provides information on the acceptability of the appearance of a clinical CT dataset and how the anatomical structures are visualised.

4.3 AUTOMATIC IMAGE QUALITY EVALUATION

The objective IQ metrics and CD analysis described above have to be quantified on technical phantoms, which do not represent the human anatomy. To measure the clinical performance of a CT system, ROC and VGA studies are currently the most used techniques in the literature [2,8]. However, these methods require a large amount of patient data. In addition, the evaluation of CT images by human observers is a time-consuming work.

An alternative approach can be automatic image quality scoring [11,12]. In Chapter 7 of this PhD dissertation, the algorithm of Kortenesniemi et al was used to quantify the IQ of a CT dataset [13]. The obtained Image Quality score (IQs) is mainly based on image noise. However, unlike global noise measurements performed in selected ROIs in the image, the method assesses local standard deviations (SD) in the neighbourhood of every pixel. A square 3x3 mask acts as a smoothing filter and is moved around each pixel in the image to 9 possible locations as illustrated in Figure 4.6.

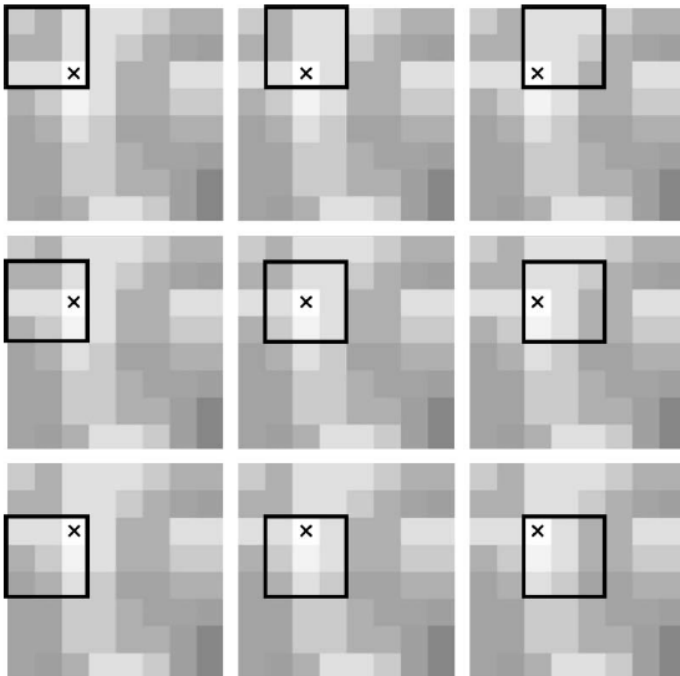


Figure 4.6 Nine possible locations of the moving filter mask for each pixel in the image [13].

For each position, the standard deviation in the mask is calculated and the location with the smallest SD is chosen. This minimum SD value and its corresponding mean pixel value are stored in a minimum SD matrix S and a mean intensity matrix M , respectively. The process is repeated for every pixel in the original image. An example of the mean intensity matrix M and the minimum SD matrix S of a CT image is shown in Figure 4.7

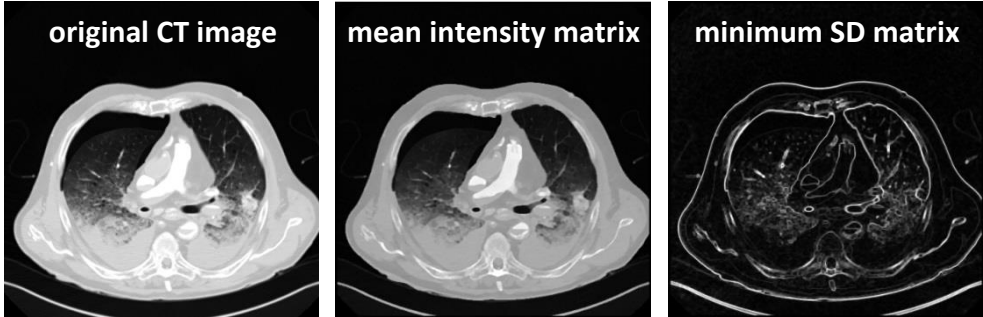


Figure 4.7 Example of an original CT image (left) together with its mean intensity matrix M (middle) and minimum SD matrix S (right).

The image quality score (IQs) is then determined from the matrix S as:

$$IQs = \frac{n_{sel}}{\sum_{i,j} \sqrt{S_{i,j}}}$$

with $S_{i,j}$ all elements of the minimum SD matrix that fulfil two selection criteria:

- 1) If the corresponding element in the mean intensity matrix has a value below -500 HU, $S_{i,j}$ is excluded from the calculation as these pixels belong to the surrounding air and not to the object of interest.
- 2) The influence of edges is minimized by taking only those pixels into account whose minimum SD value is below the 95th percentile of the fitted log-normal distribution of S (Figure 4.8).

n_{sel} are the number of pixels in the selection. The higher the IQs, the better the image quality.

An image quality metric is only useful when it generates a clearly understandable output and when it is able to cover different reconstruction methods. Therefore, the value can be normalized (nIQs) with a reverse sigmoid model, to provide values between 0 and 1:

$$nIQs = \frac{1}{1 + m \cdot \exp(-r \cdot IQs)}$$

In addition, the metric can be calibrated with respect to a reference image. To this end, the parameters m and r are determined from clinical images as:

$$m = \exp\left(\ln\left(\frac{1-k}{k}\right) \cdot \frac{IQ_{S_{0.5}}}{IQ_{S_{0.5}} - IQ_{S_k}}\right)$$

$$r = \ln\left(\frac{1-k}{k}\right) \cdot \frac{1}{IQ_{S_{0.5}} - IQ_{S_k}}$$

For a given modality and reconstruction method, an nIQs of 0.5 is assigned to a reference image with a corresponding IQs value $IQ_{S_{0.5}}$. Likewise, IQ_{S_k} corresponds to the IQ score of an image that just meets the diagnostic requirements and is given an nIQs of k . The parameter k will delineate the linear part of the sigmoid model and the reference value will be located in the middle of the linear slope, as can be seen in Figure 4.9.

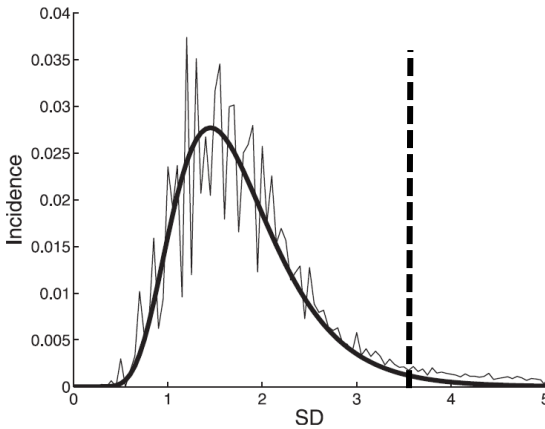


Figure 4.8 Histogram of the minimum SD matrix and fitted log-normal distribution. Only those pixels with a minimum SD below the 95th percentile ($SD = 3.55$, dashed line) are considered in the calculation of the Image Quality score [13].

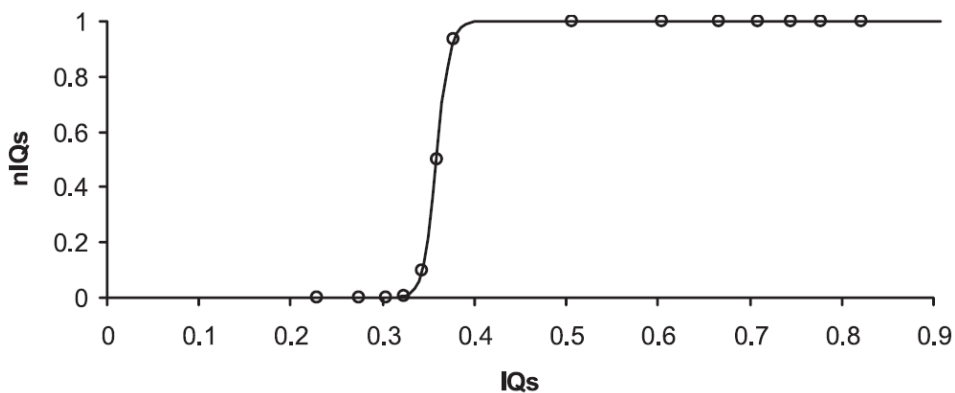


Figure 4.9 Normalized sigmoid model with $k=0.1$. Normalization of the Image Quality score generates a clearly understandable output. The nIQs values will range from 0 to 1 and a predefined reference image will result in a normalized score of 0.5 [13].

4.4 REFERENCES

- 1 McCollough CH (2016) The Role of the Medical Physicist in Managing Radiation Dose and Communicating Risk in CT. *AJR Am J Roentgenol* 206:1241-1244
- 2 Verdun FR, Racine D, Ott JG et al (2015) Image quality in CT: From physical measurements to model observers. *Phys Med* 31:823-843
- 3 Marsh DM, Malone JF (2001) Methods and materials for the measurement of subjective and objective measurements of image quality. *Radiat Prot Dosimetry* 94:37-42
- 4 Mieville FA, Gudinchet F, Brunelle F, Bochud FO, Verdun FR (2013) Iterative reconstruction methods in two different MDCT scanners: physical metrics and 4-alternative forced-choice detectability experiments--a phantom approach. *Phys Med* 29:99-110
- 5 Friedman SN, Fung GS, Siewerdsen JH, Tsui BM (2013) A simple approach to measure computed tomography (CT) modulation transfer function (MTF) and noise-power spectrum (NPS) using the American College of Radiology (ACR) accreditation phantom. *Med Phys* 40:051907
- 6 Richard S, Husarik DB, Yadava G, Murphy SN, Samei E (2012) Towards task-based assessment of CT performance: system and object MTF across different reconstruction algorithms. *Med Phys* 39:4115-4122
- 7 Bushberg JT (2012) *The essential physics of medical imaging*, 3rd edn. Wolters Kluwer Health/Lippincott Williams & Wilkins, Philadelphia
- 8 Beutel J (2000) *Handbook of medical imaging*. SPIE Press, Bellingham, Wash.
- 9 (2012) *Catphan 500 and 600 Manual*. The Phantom Laboratory
- 10 Commission of the European Communities (1999) *European guidelines on quality criteria for computed tomography* (EUR 16262).
- 11 Christianson O, Winslow J, Frush DP, Samei E (2015) Automated Technique to Measure Noise in Clinical CT Examinations. *AJR Am J Roentgenol* 205:W93-99
- 12 Tian X, Samei E (2016) Accurate assessment and prediction of noise in clinical CT images. *Med Phys* 43:475
- 13 Kortensniemi M, Schenkel Y, Salli E (2008) Automatic image quality quantification and mapping with an edge-preserving mask-filtering algorithm. *Acta Radiol* 49:45-55

Chapter 5

Aim and outline of the thesis

CT instrumentation plays an essential role in the radiology department. In contrast with conventional radiography, CT provides three-dimensional views of the organ or body region of interest. Unfortunately, the absorbed radiation doses involved in CT imaging are significantly higher than in conventional X-ray procedures. As a result, CT examinations are the most important contributors to medical radiation exposure worldwide [1-4]. The aim of this PhD thesis was to assess the performance of computed tomography (CT) systems in terms of patient dose and image quality (IQ).

To reduce patient radiation dose and to optimize image quality in CT, manufacturers implemented automatic tube current modulation (ATCM) in computed tomography systems. The overall dose-reducing effect of ATCM is demonstrated in the literature [5-9]. However, it remains unclear what the most optimal scan protocol is when using ATCM. Therefore, the purpose of the first study of this PhD work was to assess the role of the localizer and the scan direction in the process of automatic tube-current modulation. The findings of this study are described in Chapter 6: *Influence of localizer and scan direction on the dose-reducing effect of automatic tube current modulation in computed tomography*.

Apart from patient dose, IQ analysis is essential in the optimization process. An optimal balance between patient dose and image quality should be pursued. In most studies, CT image quality is based on noise measurements in a limited selection of predefined regions of interest [10-12]. As a result, only a fraction of the image dataset is actually evaluated. Alternatively, subjective image quality evaluations from observers are used, but these studies are very time consuming [13,14]. The goal of the second study of this PhD thesis was to evaluate an automatic IQ scoring tool for use in clinical practice with CT thorax examinations and evaluating the full dataset. The outcome of this work is described in

Chapter 7: *Evaluation of automatic image quality assessment in chest CT – A human cadaver study.*

Organ-based tube current modulation (OBTCM), a modification of ATCM, aims to lower the dose to superficial organs [15-17]. The exposure is reduced as the X-ray tube passes over the anterior surface of the patient. However, to preserve image quality, the tube current must increase during the posterior projections. The dose-reducing efficacy of OBTCM is critically assessed in Chapter 8: *Patient-specific dose and risk estimation for organ-based tube current modulation in chest CT.* The aim of the study was to evaluate the extent of the breast dose reduction for female patients in chest CT. The possible dose increase to the posterior organs was calculated and differences in radiation-induced cancer risks were estimated.

In the last study of this dissertation a clinically applicable and easy-to-use metric is proposed to estimate patient-specific organ doses and risks. The work focuses on paediatric CT examinations of the thorax, abdomen and pelvis. Children are found to be more sensitive to radiation-induced cancers compared to adults [1]. Moreover, they have a longer life span during which the long-term effects of earlier exposure may manifest. The results of this work are presented in Chapter 9: *The role of Size-Specific Dose Estimate (SSDE) in patient-specific organ dose and cancer risk estimation in paediatric chest and abdominopelvic CT examinations.*

5.1 REFERENCES

- 1 UNSCEAR (2008) Sources and effects of ionizing radiation. Report to the General Assembly of the United Nations. United Nations, New York
- 2 HSE (2009) Population Dose from CT Scanning, Ireland
- 3 NCRP (2009) Ionizing Radiation Exposure of the Population of the United States. NCRP Report 160, Bethesda MD
- 4 PHE (2010) Frequency and Collective Dose for Medical and Dental X-ray Examinations in the UK (HPA-CRCE-012), United Kingdom
- 5 Greess H, Wolf H, Baum U et al (2000) Dose reduction in computed tomography by attenuation-based on-line modulation of tube current: evaluation of six anatomical regions. *Eur Radiol* 10:391-394
- 6 Kalender WA, Wolf H, Suess C (1999) Dose reduction in CT by anatomically adapted tube current modulation. II. Phantom measurements. *Med Phys* 26:2248-2253
- 7 Kalra MK, Maher MM, Toth TL, Kamath RS, Halpern EF, Saini S (2004) Comparison of Z-axis automatic tube current modulation technique with fixed tube current CT scanning of abdomen and pelvis. *Radiology* 232:347-353
- 8 Rizzo S, Kalra M, Schmidt B et al (2006) Comparison of angular and combined automatic tube current modulation techniques with constant tube current CT of the abdomen and pelvis. *AJR Am J Roentgenol* 186:673-679
- 9 Tack D, De Maertelaer V, Gevenois PA (2003) Dose reduction in multidetector CT using attenuation-based online tube current modulation. *AJR Am J Roentgenol* 181:331-334
- 10 Vollmar SV, Kalender WA (2008) Reduction of dose to the female breast in thoracic CT: a comparison of standard-protocol, bismuth-shielded, partial and tube-current-modulated CT examinations. *Eur Radiol* 18:1674-1682
- 11 Gandhi D, Crotty DJ, Stevens GM, Schmidt TG (2015) Technical Note: Phantom study to evaluate the dose and image quality effects of a computed tomography organ-based tube current modulation technique. *Med Phys* 42:6572-6578
- 12 Akai H, Kiryu S, Shibata E et al (2016) Reducing CT radiation exposure with organ effective modulation: A retrospective clinical study. *Eur J Radiol* 85:1569-1573
- 13 Beutel J (2000) Handbook of medical imaging. SPIE Press, Bellingham, Wash.
- 14 Verdun FR, Racine D, Ott JG et al (2015) Image quality in CT: From physical measurements to model observers. *Phys Med* 31:823-843
- 15 Duan X, Wang J, Christner JA, Leng S, Grant KL, McCollough CH (2011) Dose reduction to anterior surfaces with organ-based tube-current modulation: evaluation of performance in a phantom study. *AJR Am J Roentgenol* 197:689-695
- 16 Ketelsen D, Buchgeister M, Fenchel M et al (2012) Automated computed tomography dose-saving algorithm to protect radiosensitive tissues: estimation of radiation exposure and image quality considerations. *Invest Radiol* 47:148-152
- 17 Seidenfuss A, Mayr A, Schmid M, Uder M, Lell MM (2014) Dose reduction of the female breast in chest CT. *AJR Am J Roentgenol* 202:W447-452

Part II

Original research

Chapter 6

Influence of localizer and scan direction on the dose-reducing effect of automatic tube current modulation in computed tomography

Caro Franck¹ and Klaus Bacher¹

¹ Department of Basic Medical Sciences
Ghent University

ABSTRACT

The purpose of this study was to investigate the influence of the localizer and scan direction on the dose-reducing efficacy of the automatic tube current modulation (ATCM) in computed tomography (CT). Craniocaudal and caudocranial chest CT scans, based on anterior–posterior (AP), posterior–anterior (PA), lateral (LAT) or dual AP/LAT localizers, of an anthropomorphic phantom containing thermoluminescent dosimeters (TLDs), were made on three Siemens systems. TLD readings were converted to lung and thyroid doses. A second dose estimation was performed based on Monte Carlo simulations. In addition, the ATCM behaviour of GE and Toshiba was evaluated based on AP, PA and LAT localizers. Compared with AP, tube currents of PA and AP/LAT scans were on average 20 % higher and 40 % lower, respectively, for the Siemens systems. Consequently, thyroid and lung doses increased with 60 % with a PA instead of an AP/LAT scan, with significant differences in image noise. Moreover, the thyroid dose halves by taking the scan in caudocranial direction. Noise values were not significantly different when changing scan direction.

INTRODUCTION

To reduce patient radiation dose and to optimise image quality in computed tomography (CT), automatic tube current modulation (ATCM) systems were adapted by the manufacturers[1-4]. By modulating the tube current along the length axis of the patient, a constant image noise can be obtained throughout the patient[5]. The tube current is adapted based on a projection radiograph (localizer), taken prior to the actual CT scan in either the anterior–posterior (AP), posterior–anterior (PA) or lateral (LAT) direction. As a result, the dose to the patient is lowered in less attenuating or smaller anatomical regions, e.g. lungs and neck.

The overall dose-reducing effect of ATCM is shown in several studies[3,6-9]. However, only a few publications investigated the behaviour of the ATCM systems in detail[10-14]. Only recently, the effect of the localizer acquisition on radiation dose associated with ATCM was addressed in more detail[14]. However, it remains unclear if the latter results are applicable for other CT systems as well. Up to now, the impact of the scan direction on CT radiation exposure is unknown.

In 2012, the European Commission published their most recent criteria for acceptability of medical radiological equipment (RP 162)[15]. The only criterion to be met for ATCM is that ‘absence of automatic dose modulation in new equipment specified more than one year after the publication of RP 162 is unacceptable’[15]. Since tube current modulation is now available and frequently used in all new CT equipment, it is worthwhile to investigate if performance evaluation of ATCM systems is necessary as part of a quality assurance programme.

The goal of this study was to investigate the influence of the localizer and the CT scan direction on the dose-reducing effect of the ATCM in chest CT.

MATERIALS AND METHODS

Automatic tube current modulation

The ATCM systems of five selected CT scanners from three different vendors [Siemens (A), GE (B) and Toshiba (C)] were evaluated.

With Siemens’ CARE Dose 4D, the topogram is initially used for estimating the attenuation levels along the PA and LAT directions of the patient and predicting the required tube

current for each table position. During each tube rotation of the acquisition, real-time feedback determines higher-order corrections to the estimated tube current for each subsequent rotation. The on-line feedback system reads the transmission values at a given angle and uses that information to predict the optimal tube current for the projection that will occur 180° later in the tube rotation[16].

GE's SmartmA determines the tube current based on the scout image of the patient. For any given z-location, the system estimates the attenuation level and the oval ratio from the scout. The attenuation level reflects the density and size of the patient. The oval ratio reflects how circular or elliptical the patient is at that level and is estimated from brightness and width information in the scout image. The system will then use the oval ratio and attenuation level to determine the appropriate tube current. It is not possible to adjust the tube current during the scan acquisition. No data of the last 180° are used for the up-coming modulation[17].

Sure Exposure from Toshiba tailors the tube current along the longitudinal direction of the patient to account for variations in size and density. The system also modulates the tube current to account for variations in patient shape and density in the axial plane. To accomplish this, Sure Exposure determines the relative attenuation of a patient from a scanogram and converts this information into a water-equivalent thickness. There is no on-line feedback to adjust the tube current during the CT acquisition.

Scan protocols

The different CT scanners, together with the scanning parameters used, are specified in Table 1. The z-axis geometric efficiency values of all used collimations were higher than 80 %. Prior to the start of this study, all CT scanners passed a quality control test according to RP 162[15]. In order to mimic the ATCM in clinical conditions, CT scans of the thoracic region of an anthropomorphic RANDO phantom (Alderson, Long Beach, CA, USA) were obtained. The latter phantom represents the reference male, according to the ICRP[18]. The phantom was scanned from the chin to the middle of the liver (Sections 9–23), resulting in a scan range of 375 mm. For each CT scan, the centre of the anthropomorphic phantom was positioned in the isocentre.

On each of the five CT systems, both craniocaudal and a caudocranial chest scans were performed with ATCM based on either an AP, PA or LAT localizer acquisition. In addition, scans in both directions, based on a dual AP/LAT or PA/LAT localizer, were made on all three systems from Vendor A. Mean volume computed tomography dose index ($CTDI_{vol}$) values of the different CT acquisitions are presented in Table 2.

For each of the acquisitions, tube current values were extracted from the axial DICOM images and effective mAs per slice values were calculated as follows:

$$mAs_{eff} = \frac{mA * s}{Pitch}$$

These values were then plotted against their respective positions along the scan direction. As a direct comparison of the mAs_{eff} values of the different systems was not of prior interest in this study, the effective mAs values of the Siemens Definition AS, Siemens Biograph mCT 20, GE Discovery 750 HD and Toshiba Aquilion 32 acquisitions were scaled as such that the mean $CTDI_{vol}$ of their AP craniocaudal scan was equal to that of the Siemens Definition Flash. Correction factors are given in Table 2.

Table 1 Scanning parameters used with the different CT scan models

CT scan model	kVp	Rotation time (ms)	Pitch	Collimation (mm)	Geometric efficiency	Slice width (mm)	FOV (mm)	ATCM system	Image quality
Vendor A: Siemens									
Definition AS	120	330	0.9	40 x 0.6	0.85	3	500	CARE Dose 4D	Quality ref mAs = 90
Definition Flash	120	330	0.9	64 x 0.6	0.89	3	500	CARE Dose 4D	Quality ref mAs = 90
Biograph mCT 20 ^a	120	330	0.9	64 x 0.6	0.80	3	500	CARE Dose 4D	Quality ref mAs = 90
Vendor B: GE									
Discovery 750 HD	120	900	1.375	64 x 0.625	0.93	2.5	500	SmartmA	40-360 mA; NI=54.93
Vendor C: Toshiba									
Aquilion 32	120	500	0.844	32 x 0.5	0.82	3	500	Sure Exposure	SD = 12

^aPET/CT

Table 2 CTDI_{vol} (mGy) values of the different acquisitions and their correction factors

		Caudocranial	Craniocaudal				Correction
		AP	AP	PA	LAT	AP/LAT	factor
Vendor A							
Siemens	Definition Flash	6.8	6.7	8.1	4.3	4.1	-
Siemens	Definition AS	6.2	6.1	8.2	4.4	4.1	1.10
Siemens	Biograph mCT 20	6.5	6.5	8.6	5.5	4.3	1.03
Vendor B							
GE	Discovery 750 HD	3.0	3.0	3.9	3.4	-	2.24
Vendor C							
Toshiba	Aquilion 32	22.5	20.8	22.1	18.2	-	0.32

Dose calculations

The impact of the localizer and CT scan direction on thyroid and lung dose was investigated on the Siemens Definition Flash system.

Thermoluminescent dosimeters

In a first approach, thermoluminescent dosimeters (TLDs) were positioned in predrilled holes of the RANDO phantom. The TLDs had a diameter of 5 mm, a thickness of 1 mm and consisted of lithium fluoride, doped with magnesium and titanium (LiF:Mg,Ti) (MTS-N, TLD Poland, Kraków, Poland). A calibration in air was performed in the Laboratory of Standard Dosimetry (Department of Basic Medical Sciences, Ghent University, Belgium). For this purpose, an X-ray tube was used at 120 kVp to deliver a given dose to the TLDs.

For the organ dose calculations, 54 TLDs were used: 2 in the thyroid and 42 equally distributed in both lungs. The remaining TLDs were kept in the same conditions as the other TLDs, without irradiating. Their mean readout was used as background signal to correct the other readings. A conversion factor of 1.08 Gy Gy^{-1} was used to calculate tissue dose from the measured dose in air [19].

Monte Carlo simulations

As a second approach, Monte Carlo simulations of the different CT acquisitions were performed. To this end, ImpactMC 1.5.1 (CT Imaging, Erlangen, Germany) was used, a validated and patient-specific dose calculation tool[20-22].

A voxel model was created, using 512 x 512 axial DICOM images of the entire RANDO phantom, with a voxel size of 0.98 x 0.98 x 3 mm³. The images were recorded on a 64-slice Siemens Definition Flash CT (Siemens Medical Solutions, Erlangen, Germany). Then, the geometry of the scanner was build: centre of rotation (COR), collimation, distance focus to COR, bow tie filter and 120 kVp X-ray spectrum. The extracted mAs per slice values were imported in the software. Next, a 3D dose distribution was generated, considering all relevant interaction processes and dose depositions of a large number of photons (10⁹): photoelectric effect, Compton and Rayleigh scattering[21,22]. In this way, the dose in each voxel of the model can be assessed, and organ doses can be calculated. The thyroid and the lungs were manually delineated on the original images. These regions of interest (ROIs) were then used to determine the mean thyroid and lung dose on the output images of the simulation software.

The simulation software was calibrated based on the air kerma measured free in air in the isocentre of the CT scanner. For this purpose, a pencil ionisation chamber was used (Xi CT detector, Unfors RaySafe, Billdal, Sweden).

Image noise

In the images of the anthropomorphic phantom, 60 ROIs were defined, equally distributed over 3 different anatomical locations: neck, shoulders and lower thorax. Image noise in the anthropomorphic phantom was then determined by means of the standard deviation (SD) of the measured Hounsfield units (HU) in these ROIs. For each anatomical location (neck, shoulders, lower thorax), image noise was compared between the two scan directions, using a Wilcoxon signed-rank test. The comparison between the five craniocaudal scans, based on different localizers, was made with a Kruskal–Wallis test. A p-value of < 0.05 was regarded as statistically significant.

RESULTS

Tube current modulation behaviour

All three systems from Vendor A (Definition AS, Definition Flash and Biograph mCT 20) realised a nearly identical variation of the effective mAs per slice at different positions along the anthropomorphic phantom. Therefore, only the results for the Definition Flash are shown (Figures 1a and 2a).

The ATCM curves resulting from a craniocaudal CT scan based on an AP localizer image are shown in grey circles in Figure 1. With Vendor A (Figure 1a), the exposure starts with a minimum value in the neck region. A steep increase is noticed, and the maximum value is reached when scanning the shoulders. Finally, when reaching the lower thorax, the exposure is decreased again.

Compared with Vendor A, the ATCM behaviour of Vendor B (Figure 1b) is smoother, and the effective mAs value variation range is smaller. Nevertheless, the ATCM system reacts as expected based on the attenuation of the different anatomical regions. With Vendor C (Figure 1c), large oscillations in effective mAs values were revealed throughout the scan range. Furthermore, the exposure was increased to a maximum at a position of 30 mm below the shoulders. In addition, a steep exposure decrease in the abdomen was observed. The latter observations do not comply with the actual differences in tissue densities.

Apart from a craniocaudal CT scan, caudocranial acquisitions were acquired as well. The ATCM results of these scans, based on an AP localizer, are shown in white triangles in Figure 1. Since the phantom was not moved after the craniocaudal scan and scan parameters were not altered, similar ATCM behaviour was expected. However, a shift of 50 mm was noticed with Vendor A, when the phantom was scanned in the other direction. For scans based on other localizers, similar differences were observed when the scan direction was changed.

With the caudocranial acquisition, the build-up towards the high-current zone of the shoulders started already in the lower thorax region, resulting in higher mAs_{eff} values, compared with the craniocaudal scan. However, lower exposure values were selected in the neck, with the caudocranial acquisition. With Vendor B, the differences in ATCM behaviour for the two scan directions were smaller, but still noticeable. With Vendor C, the differences were negligible.

Large differences in selected exposure values were noticed, when a craniocaudal scan was based on another localizer. The results are displayed in Figure 2. With Vendor A, when the

scan was based on a PA or dual AP/LAT localizer, mean mAs_{eff} was 20 % higher and 40 % lower, respectively, compared with an AP acquisition. On the other hand, with Vendor B, exposure values were on average 30 % higher for a PA and 10 % higher for a LAT acquisition, with respect to an AP localizer. With Vendor C, ATCM behaviour was similar for scans based on a PA or AP localizer. However, exposure values were 20 % lower when the scan was based on a LAT instead of an AP localizer. With Vendor A, the lowest mAs_{eff} values were selected when a dual localizer was used, with no significant difference between an AP/LAT or a PA/LAT combination. Furthermore, mAs_{eff} values selected with a LAT localizer were closest to these recorded with a dual localizer (6 % average difference).

Dose

Organ dose measurements for the five different scan acquisitions with the Definition Flash are summarised in Table 3. A good agreement was found between the TLD and Monte Carlo methods (2 % average difference). The thyroid dose was reduced by ~50 %, when taking an AP-based scan in the caudocranial instead of the craniocaudal direction. For a craniocaudal scan, both lung and thyroid doses were reduced by ~60 % when based on a dual AP/LAT localizer, instead of a single PA acquisition.

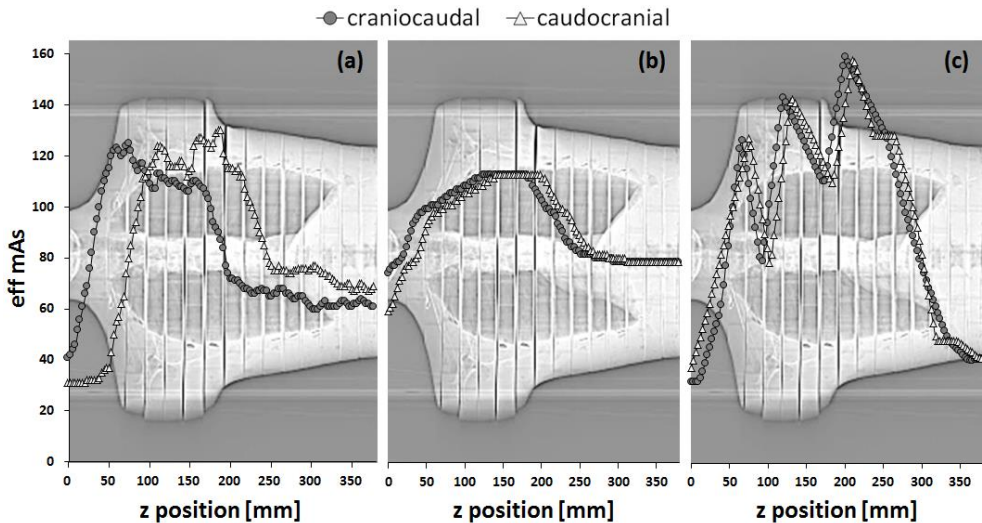


Figure 1 Effective mAs per slice values, as a function of slice position along the z -axis of the scanner, for the (a) Siemens Definition Flash, (b) GE Discovery 750 HD and (c) Toshiba Aquilion 32 CT. Chest scans of an anthropomorphic phantom were made in craniocaudal (*grey circles*) and caudocranial (*white triangles*) direction, based on an AP localizer. The mAs_{eff} values of the GE and Toshiba acquisitions were scaled, as such that the mean $CTDI_{vol}$ of their craniocaudal scan was equal to that of the Siemens Definition Flash.

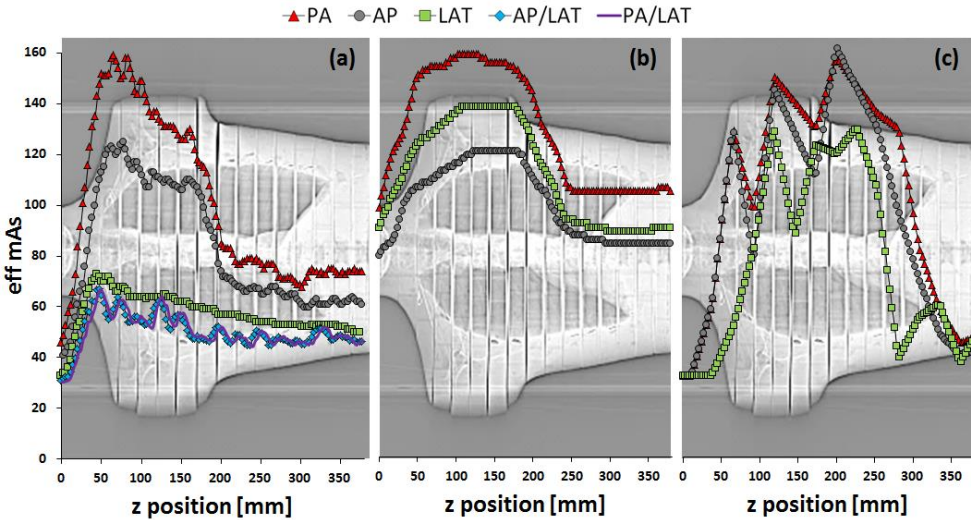


Figure 2 Effective mAs per slice values, as a function of slice position along the z-axis of the scanner, for the (a) Siemens Definition Flash, (b) GE Discovery 750 HD and (c) Toshiba Aquilion 32 CT. Chest scans of an anthropomorphic phantom were made in de craniocaudal direction, based on a PA (triangles), AP (circles), LAT (squares), combined AP/LAT (diamonds) or PA/LAT (full line) localizer image. The mAs_{eff} values of the GE and Toshiba acquisitions were scaled, as such that their mean $CTDI_{vol}$ of the AP scan was equal to that of the Siemens Definition Flash.

Image noise

Mean image noise in three anatomical regions (neck, shoulders and lower thorax) for the five different scan acquisitions with the Definition Flash is shown in Table 3. No significant differences in image noise were found between AP-based scans in different directions. However, when a craniocaudal scan was based on other localizers, significant differences in image noise were found in the neck and shoulder region.

Table 3 Dose and image noise measurements for the Siemens Definition Flash

	caudocranial		craniocaudal		
	AP	AP	PA	LAT	AP/LAT
TLD dose [mGy]					
Thyroid	5.3	10.1	13.3	7.2	5.4
Lung	9.8	9.2	13.2	7.1	6.1
MC dose [mGy]					
Thyroid	5.7	10.2	12.6	7.4	5.6
Lung	10.7	9.5	11.5	6.4	4.8
Image noise [HU]					
Neck	10.2	9.2	8.7	9.7	10.8
Shoulders	15.4	15.6	14.6	17.1	18.8
Lower thorax	14.8	15.7	15.0	16.7	18.1

DISCUSSION

In CT imaging, the use of ATCM systems is becoming a routine practice. Many studies address the dose-reducing effect of ATCM[3,6-9]. For chest CT, dose reductions up to 22 % were reported[9]. However, only few studies focus on the exact ATCM system performance.

In current study, the tube current modulation is behaving as expected with a chest protocol for all CT scanners under investigation. The lowest mA is found in the neck region, a steep increase towards the shoulders is noticed and lower tube current values are selected for the lower thorax region. However, large oscillations were observed with Vendor C. This behaviour was stated before by Sookpeng et al.[12] An increase in the mA values is noticed within, and even after, the shoulder region. Next, in the lower thorax, tube current values drop to a level comparable with the neck region. Nonetheless, since the upper abdomen is larger and more attenuating than the neck, higher mA values should be selected in this region.

It was shown that both the localizer acquisition and the CT scan direction have an important influence on the dose-reducing effect of ATCM. For Vendor A, the thyroid dose was reduced by ~50 % when the scan was performed in the caudocranial instead of the craniocaudal direction, without significant differences in image noise. Large dose differences were found when the ATCM was based on different localizers. A 60 % lung and thyroid dose reduction was achieved when the CT scan was based on a dual localizer acquisition instead of a single PA projection. These findings are in line with Pourjabbar et al.[23], showing an overestimation of patient size on radiographs due to magnification. By

acquiring two orthogonal radiographs, the patient size and attenuation level can be estimated more accurately. Hence, selected mAs values and patient doses will be lower, when based on a dual instead of a single localizer. The study of Singh et al. confirms this: lower $CTDI_{vol}$ values were seen when two orthogonal localizer radiographs were acquired, instead of a single AP or PA localizer[14].

The present study has some limitations. First, overscanning and overbeaming effects are not specifically taken into account in the Monte Carlo simulations. Therefore, simulated thyroid doses might be underestimated. Furthermore, since the exact structure of the bow tie filter is confidential information of the manufacturer, a predefined filter is used for the Monte Carlo simulations. Performing the simulations with a system-specific bow tie filter will lead to more accurate results[24-26].

CONCLUSIONS

Current study shows that there is a strong need for ATCM performance evaluation to assure optimal dose reduction for the patient and to keep exposures to ionising radiation as low as reasonably achievable (ALARA principle). Optimisation of CT protocols has to be done with respect to scan direction and localizer acquisition. In practice, the evaluation of ATCM can be performed by a medical physics expert at acceptance testing of a new CT scanner. In this work, an anthropomorphic RANDO phantom was used to study ATCM behaviour. However, cylindrical PMMA phantoms of different sizes, as used for CTDI measurements, could be used instead.

FUNDING

This work was supported by the Agency for Innovation by Science and Technology (IWT) (Grant Number 121663).

REFERENCES

- 1 Kalender WA, Wolf H, Suess C, Gies M, Greess H, Bautz WA (1999) Dose reduction in CT by on-line tube current control: principles and validation on phantoms and cadavers. *Eur Radiol* 9:323-328
- 2 Gies M, Kalender WA, Wolf H, Suess C (1999) Dose reduction in CT by anatomically adapted tube current modulation. I. Simulation studies. *Med Phys* 26:2235-2247
- 3 Kalender WA, Wolf H, Suess C (1999) Dose reduction in CT by anatomically adapted tube current modulation. II. Phantom measurements. *Med Phys* 26:2248-2253
- 4 McCollough CH, Bruesewitz MR, Kofler JM, Jr. (2006) CT dose reduction and dose management tools: overview of available options. *Radiographics* 26:503-512
- 5 Kalra MK, Maher MM, Toth TL et al (2004) Techniques and applications of automatic tube current modulation for CT. *Radiology* 233:649-657
- 6 Kalra MK, Maher MM, Toth TL, Kamath RS, Halpern EF, Saini S (2004) Comparison of Z-axis automatic tube current modulation technique with fixed tube current CT scanning of abdomen and pelvis. *Radiology* 232:347-353
- 7 Tack D, De Maertelaer V, Gevenois PA (2003) Dose reduction in multidetector CT using attenuation-based online tube current modulation. *AJR Am J Roentgenol* 181:331-334
- 8 Rizzo S, Kalra M, Schmidt B et al (2006) Comparison of angular and combined automatic tube current modulation techniques with constant tube current CT of the abdomen and pelvis. *AJR Am J Roentgenol* 186:673-679
- 9 Greess H, Wolf H, Baum U et al (2000) Dose reduction in computed tomography by attenuation-based on-line modulation of tube current: evaluation of six anatomical regions. *Eur Radiol* 10:391-394
- 10 Goo HW, Suh DS (2006) The influences of tube voltage and scan direction on combined tube current modulation: a phantom study. *Pediatr Radiol* 36:833-840
- 11 Tsalafoutas IA, Varsamidis A, Thalassinou S, Efstathopoulos EP (2013) Utilizing a simple CT dosimetry phantom for the comprehension of the operational characteristics of CT AEC systems. *Med Phys* 40:1119-18
- 12 Sookpeng S, Martin CJ, Gentle DJ (2013) Comparison of different phantom designs for CT scanner automatic tube current modulation system tests. *J Radiol Prot* 33:735-761
- 13 Bosmans H, Lemmens K, Malone J, Oyen R (2013) Quality assurance in CT with the Belgian protocol and the new European acceptability criteria. *Radiat Prot Dosimetry* 153:197-205
- 14 Singh S, Petrovic D, Jamnik E et al (2014) Effect of localizer radiograph on radiation dose associated with automatic exposure control: human cadaver and patient study. *J Comput Assist Tomogr* 38:293-298
- 15 RP (2012) Criteria for acceptability of medical radiological equipment used in diagnostic radiology, nuclear medicine and radiotherapy. Radiation Protection 162. Office for Official Publications of the European Communities
- 16 Rego SL, Yu L, Bruesewitz MR, Vrieze TJ, Kofler JM, McCollough CH (2008) CARE Dose4D Automatic Exposure Control System: Physics Principles and Practical Hints. Mayo Foundation for Medical Education and Research

- 17 Bruesewitz MR, Yu L, Vrieze TJ, Kofler JM, McCollough CH (2008) Smart mA - Automatic Exposure Control (AEC): Physics Principles and Practical Hints. Mayo Foundation for Medical Education and Research
- 18 ICRP (2002) Basic anatomical and physiological data for use in radiological protection: reference values. A report of age- and gender-related differences in the anatomical and physiological characteristics of reference individuals. ICRP Publication 89. Ann ICRP 32:5-265
- 19 Ma CM, Seuntjens JP (1999) Mass-energy absorption coefficient and backscatter factor ratios for kilovoltage x-ray beams. Phys Med Biol 44:131-143
- 20 Schmidt B, Saltybaeva N, Kolditz D, Kalender WA (2013) Assessment of patient dose from CT localizer radiographs. Med Phys 40:084301
- 21 Deak P, van Straten M, Shrimpton PC, Zankl M, Kalender WA (2008) Validation of a Monte Carlo tool for patient-specific dose simulations in multi-slice computed tomography. Eur Radiol 18:759-772
- 22 Chen W, Kolditz D, Beister M, Bohle R, Kalender WA (2012) Fast on-site Monte Carlo tool for dose calculations in CT applications. Med Phys 39:2985-2996
- 23 Pourjabbar S, Singh S, Padole A, Saini A, Blake MA, Kalra MK (2014) Size-specific dose estimates: Localizer or transverse abdominal computed tomography images? World J Radiol 6:210-217
- 24 Boone JM (2010) Method for evaluating bow tie filter angle-dependent attenuation in CT: theory and simulation results. Med Phys 37:40-48
- 25 McKenney SE, Nosratieh A, Gelskey D et al (2011) Experimental validation of a method characterizing bow tie filters in CT scanners using a real-time dose probe. Med Phys 38:1406-1415
- 26 Whiting BR, Evans JD, Dohatcu AC, Williamson JF, Politte DG (2014) Measurement of bow tie profiles in CT scanners using a real-time dosimeter. Med Phys 41

Chapter 7

Evaluation of automatic image quality assessment in chest CT – A human cadaver study

Caro Franck¹, An De Crop², Bieke De Roo³, Peter Smeets³, Merel Vergauwen³, Tom Dewaele³, Mathias Van Borsel^{3,4}, Eric Achten³, Tom Van Hoof¹, Klaus Bacher¹

¹ Department of Basic Medical Sciences
Ghent University, Belgium

² Radiology Department
AZ Delta, Belgium

³ Radiology Department
Ghent University Hospital, Belgium

⁴ Radiology Department
Sint-Jozefskliniek Izegem, Belgium

ABSTRACT

Purpose The evaluation of clinical image quality (IQ) is important to optimize CT protocols and to keep patient doses as low as reasonably achievable. Considering the significant amount of effort needed for human observer studies, automatic IQ tools are a promising alternative. The purpose of this study was to evaluate automatic IQ assessment in chest CT using Thiel embalmed cadavers.

Methods Chest CT's of Thiel embalmed cadavers were acquired at different exposures. Clinical IQ was determined by performing a visual grading analysis. Physical-technical IQ (noise, contrast-to-noise and contrast-detail) was assessed in a Catphan phantom. Soft and sharp reconstructions were made with filtered back projection and two strengths of iterative reconstruction. In addition to the classical IQ metrics, an automatic algorithm was used to calculate image quality scores (IQs). To be able to compare datasets reconstructed with different kernels, the IQs values were normalized.

Results Good correlations were found between IQs and the measured physical-technical image quality: noise ($\rho = -1.00$), contrast-to-noise ($\rho = 1.00$) and contrast-detail ($\rho = 0.96$). The correlation coefficients between IQs and the observed clinical image quality of soft and sharp reconstructions were 0.88 and 0.93, respectively.

Conclusions The automatic scoring algorithm is a promising tool for the evaluation of thoracic CT scans in daily clinical practice. It allows monitoring of the image quality of a chest protocol over time, without human intervention. Different reconstruction kernels can be compared after normalization of the IQs.

INTRODUCTION

The exposure to ionising radiation from medical devices has gained more and more attention over the past few years [1,2]. Different dose management solutions are now widely used to track the patient's dose in terms of $CTDI_{vol}$ or size-specific dose estimate (SSDE) [3-5]. These tools help to maintain radiation doses within the dose reference levels (DRLs). However, lowering the dose to the patient is not straightforward. The evaluation of image quality (IQ) is equally important to optimize CT protocols and to keep doses as low as reasonably achievable (ALARA). An optimal balance has to be found between the patient's dose and the image quality of the acquired dataset.

Several standardized methods exist to express physical-technical IQ. With the use of dedicated phantoms, traditional objective metrics can be evaluated. These include image noise, contrast-to-noise, contrast-detail and spatial resolution. Although it is common practice to specify the performance of diagnostic systems in physical-technical terms, it is complicated to translate these metrics to clinical performance [6]. A standardized phantom (e.g. Catphan®) can be used to perform quality control of CT scanners over time, but does not represent the patient's anatomy. Using anthropomorphic phantoms and task based IQ criteria is necessary to optimize CT protocols. Translating the clinical question to a set-up with an anthropomorphic phantom is the most difficult step in these kind of studies.

Several approaches exist to measure the clinical IQ of a CT scanner. Receiver operating characteristic (ROC) studies and visual grading analyses (VGA) are currently the most used techniques to quantify the diagnostic performance of a system [6,7]. Since anthropomorphic phantoms are not patient-specific, the use of real patient data can be considered. However, ROC and VGA studies require clinical images of a large number of patients which is often not feasible. The evaluation of CT images by human observers is a valuable yet time-consuming technique. Moreover, subtle decreases in IQ over time may not be noticed by a human observer.

Considering the significant amount of time and effort needed for human observer studies, automatic IQ scoring tools are a promising alternative [8-10]. These tools allow the evaluation of a clinical dataset without human interaction. Instead, the images are scored based on a preprogrammed algorithm, implemented in the CT software. The obtained IQ figure can be stored in a database, together with the delivered dose ($CTDI_{vol}$). In this way, the balance between dose and IQ can be monitored over time using quality management software. Alerts for changes in both IQ and dose can be set, so that adjustments can be made if necessary.

In this study, the automatic scoring algorithm proposed by Kortensniemi et al was used to evaluate the IQ of a CT dataset [8]. The method allows an automatic analysis of the IQ,

without human intervention. To evaluate the performance of the algorithm, chest CT's of Thiel embalmed cadavers were made. Using the Thiel technique, organs and tissues are extremely well preserved in terms of flexibility and plasticity [11,12]. This is in sharp contrast to the classical formol embalming.

The aim of this study was to evaluate an automatic image quality scoring tool for use in clinical practice for chest CT scans.

MATERIAL AND METHODS

Image acquisition

All scans were performed on a Siemens Somatom Definition Flash CT scanner. Scan parameters were 120 kVp, 330 ms rotation time, 38.4 mm collimation and 0.9 pitch. Using tube current modulation (TCM), chest CT scans of all three lung ventilated Thiel embalmed cadavers were made. Increasing reference mAs values from 12 to 150 mAs were selected for each cadaver, resulting in $CTDI_{vol}$ values ranging from 0.84 to 11.59 mGy (Table 1). Next, scans of the Catphan[®] phantom were acquired at fixed exposures, corresponding to the mean mAs values recorded in the different Thiel body's at different ref mAs settings. This resulted in increasing fixed exposure values from 12 to 200 mAs (Table 1). Standard 512x512 DICOM images were reconstructed with a FOV of 38 cm and a slice thickness of 3 mm using medium smooth and very sharp kernels. Both filtered back projection (FBP) and iterative reconstruction (SAFIRE) techniques were used. Two different strengths of SAFIRE were set, resulting in 6 data sets for each CT acquisition (B30, I30/1, I30/3, B70, I70/1 and I70/3). The acquired images were viewed on a 30 inch, 3 MP high-contrast colour monitor (Barco MDCC 6130DL, Kortrijk, Belgium) at optimal lightning conditions, according to the AAPM TG18 report [13]. Maximum luminance was 400 cd/m² and ambient lighting levels were below 50 lux.

Table 1 Ref mAs settings used for scanning the chest region of the Thiel embalmed cadavers. In addition, the corresponding mean mAs and $CTDI_{vol}$ values are shown. The resulting mean mAs values of the different ref mAs setting were used to acquire scans of the Catphan® phantom at fixed exposures.

ref mAs	mean mAs	$CTDI_{vol}$
12	12	0.84
30	34	2.05
60	67	4.08
90	103	6.18
120	152	8.35
150	200	11.59

Catphan phantom

The Catphan® 504 phantom was used to evaluate the physical-technical image quality. Image noise σ was measured in the uniform acrylic background of four consecutive slices of the CT number accuracy module (CTP404). The SD of the pixel intensities in a circular region of interest (ROI) of 10 mm diameter was acquired. The contrast-to-noise ratio's (CNR) for teflon (bone equivalent material) relative to acrylic (soft tissue equivalent material), air relative to acrylic and teflon relative to air were calculated in four consecutive slices of the CTP404 module:

$$CNR = \frac{S_1 - S_2}{\sigma}$$

S_1 and S_2 are the mean pixel intensities in HU for teflon, acrylic or air. Mean pixel values were measured in circular ROIs with a diameter of 10 mm. The low contrast module, used for contrast-detail (CD) analysis, includes supra-slice targets of different diameters and contrasts (CTP515). Each contrast level (0.3, 0.5 and 1 %) holds 9 inserts with decreasing diameters (15, 9, 8, 7, 6, 5, 4, 3 and 2 mm). Seven experienced medical physicists determined the number of targets visible for each contrast level. To be able to compare the contrast-detail images in a quantitative way, the inverse image quality figure was used [14]:

$$IQF_{inv} = \frac{100}{\sum_{i=1}^3 C_i D_i}$$

With D_i the diameter of the smallest visible target at a given contrast level C_i . A completely invisible contrast level results in a D_i of 20 mm. The IQF_{inv} scores were averaged over the seven readers.

Thiel embalmed cadavers

The study had ethical approval for the use of human cadavers. Following the methodology of Prof. Em. Walther Thiel [11,12], three cadavers (2 male, 1 female) were embalmed. The embalment methods have previously been described by De Crop et al [15]. After ventilating the lungs by performing a tracheotomy in combination with balloon ventilation, chest CT scans were acquired. Previous studies confirmed the equivalency of thorax images of patients and Thiel embalmed cadavers [15,16].

The acquired CT datasets were scored by four experienced radiologists (6 to 25 years of experience). The scoring criteria, based on the European Guidelines on Quality Criteria for Computed Tomography [17], are listed in Table 2. All criteria were evaluated on predefined slices of the Thiel stacks. Each structure was rated on a four-level Likert scale, as indicated in Table 3. Next, for each reader, an absolute VGA score (VGAS) was calculated as:

$$VGAS = \frac{\sum_{s=1}^S \sum_{t=1}^T G_{abs,s,t}}{S * T}$$

Where S and T are the number of structures and Thiel body's, respectively 9 and 3. $G_{abs,s,t}$ is the rating for a particular structure (s) and Thiel body (t) [18]. The stacks were shown in a random order and blinded for acquisition and reconstruction parameters. A detail of a Thiel cadaver CT image is shown in Fig. 1.

In addition, background noise was defined as SD of the pixel intensities in a 100 cm² ROI, located in the air surrounding the cadaver images.

Table 2 Image quality criteria used for scoring of the chest CT images. The criteria are based on the European Guidelines on Quality Criteria for Computed Tomography [17].

Criterion no.	Description
1	Visually sharp reproduction of a nodular hypodense structure in a high density area such as an alveolus in consolidated lung parenchyma
2	Visually sharp reproduction of a nodular hypodense structure in a low density area such as normal lung parenchyma
3	Visually sharp reproduction of nodular hyperdense structure in a low density area such as a vessel in aerated lung parenchyma
4	Visually sharp reproduction of an inter- or intralobular septum
5	Visually sharp reproduction of the bronchial wall
6	Visually sharp reproduction of the lung fissure
7	Visually sharp reproduction of a peripheral pulmonary artery branch
8	Visually sharp reproduction of fibrous strands
9	Visually sharp reproduction of the parietal and or visceral pleura

Table 3 Rating used to evaluate the chest CT scans of the Thiel embalmed cadavers.

Rating	The structure in the image is:
1	Not visible
2	Poorly reproduced
3	Adequately reproduced
4	Very well reproduced

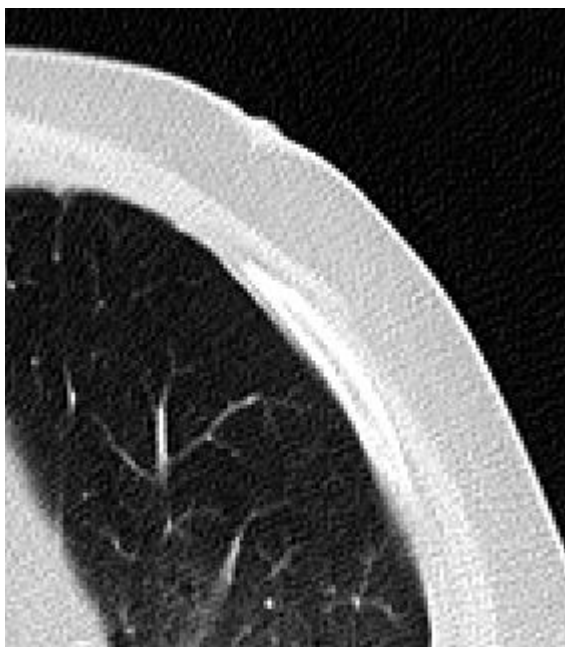


Figure 1 Detail of a Thiel cadaver CT image, illustrating normal lung parenchyma, vessels in aerated lung parenchyma, inter- and intralobular septa and visceral pleura.

Image quality score

In addition to the conventional image quality metrics, the method described by Kortensniemi et al was used to quantify the IQ of a CT dataset [8]. This filtering algorithm uses a moving square mask to create a map of filtered local intensity and noise values. With these data, image quality scores (IQs) are calculated. The higher the IQs, the better the image quality. The algorithm was built in ImageJ (version 1.50e, National Institute of Health, USA), using its macro language. It allows an automatic analysis of a CT dataset, without human intervention.

IQs values were calculated on four consecutive slices of the Catphan CTP404 and CTP515 modules. Mean results were used to compare with the noise, CNR and contrast-detail analysis. In addition, IQs values were calculated on all slices of the Thiel stacks. Mean results were compared with the visual grading analysis.

To be able to compare datasets reconstructed with different kernels, normalized image quality scores (nIQs) were calculated, according to the method of Kortensniemi et al [8]. To this end a reverse sigmoid model was applied, using 2 boundary conditions. An image series with a VGAS of 3, meaning the structures in the dataset are adequately reproduced,

was given a normalized IQ score of 0.5. This value is located in the middle of the sigmoid model, so that deviations from it should fall in the linear part around this reference value. To delineate the linear part of the sigmoid model, a nIQs score of 0.1 was assigned to a CT dataset with a VGAS of 2: a series that just meets the diagnostic requirements. After the normalisation step, the IQ scores will vary between 0 and 1, which simplifies the interpretation.

Statistical analysis

Intraclass correlation coefficients were calculated to assess the inter-observer agreement for IQF_{inv} and VGAS values. To measure the strength and direction of association between two variables, Spearman's rank correlation coefficient (Spearman's ρ) was calculated. A 95% confidence interval was used for all statistical measures. All calculations were performed with IBM SPSS Statistics for Windows (version 23.0, released 2013, IBM corp., NY, USA).

RESULTS

Intraclass correlation coefficients for the IQF_{inv} and VGAS scorings were 0.962 and 0.919, respectively. These findings indicate an excellent agreement between the different readers.

To evaluate the automatic calculation of an image quality score for a CT dataset, the correlation with noise, CNR, IQF_{inv} and VGAS was evaluated. Different exposure values and reconstruction kernels were analysed. A total of 6 mAs settings and 6 reconstruction filters were used, resulting in 36 data points for each IQ metric. Correlations were calculated separately for FBP and SAFIRE images (Table 4). An excellent correlation was found between image noise and IQs ($\rho = -1.000$, $p < 0.001$, Fig. 2), which is comparable to the results of Kortensniemi et al [8]. All three CNR's resulted in a correlation coefficient of 0.999 ($p < 0.001$), as shown in Fig. 3. For the CD analysis, a correlation coefficient of 0.955 and 0.952 was observed, using the smooth (Fig. 4) and sharp (Fig. 5) kernels respectively ($p < 0.001$).

Table 4 Spearman's rank correlation coefficients, calculated separately for filtered back projected (FBP) and iteratively reconstructed (SAFIRE) images.

correlation of IQs with:	Spearman's ρ		
	FBP	SAFIRE	FBP + SAFIRE
image noise	-1.000	-1.000	-1.000
CNR			
teflon-acrylic	1.000	1.000	0.999
air-acrylic	1.000	1.000	0.999
teflon-air	1.000	1.000	0.999
IQ_{inv}			
smooth kernels	1.000	0.958	0.955
sharp kernels	1.000	0.935	0.952
Background noise			
smooth kernels	-0.886	-0.762	-0.695
sharp kernels	-1.000	-0.825	-0.774
VGAS			
smooth kernels	0.943	0.902	0.880
sharp kernels	1.000	0.972	0.928

When scanning the Thiel embalmed cadavers, a negative correlation was found between background noise and VGAS. Results are shown separately for soft ($\rho = -0.695$, $p < 0.01$) and sharp ($\rho = -0.774$, $p < 0.001$) reconstruction kernels in Figures 6 and 7. Comparing VGAS with mean IQs values, calculated only on the selected slices used for the visual grading study resulted in a correlation coefficient of 0.814 and 0.914, respectively for soft and sharp reconstructions ($p < 0.001$). Including the whole stack of Thiel images in the IQs calculation resulted in even better correlations ($\rho = 0.880$ for soft kernels and $\rho = 0.928$ for sharp kernels, $p < 0.001$). The results of the latter calculations are displayed in Figures 8 and 9.

Smooth and sharp reconstruction kernels show different correlations between IQs and VGAS. This means that a direct comparison of the IQ of different filters is not possible when using IQs as a parameter. To overcome this issue, the image quality scores were normalized, using a sigmoid model. The relationship between IQs and nIQs is displayed in Fig. 10, both for smooth and sharp reconstructions. Fig. 11 shows the correlation between nIQs and VGAS ($\rho = 0.910$, $p < 0.001$).

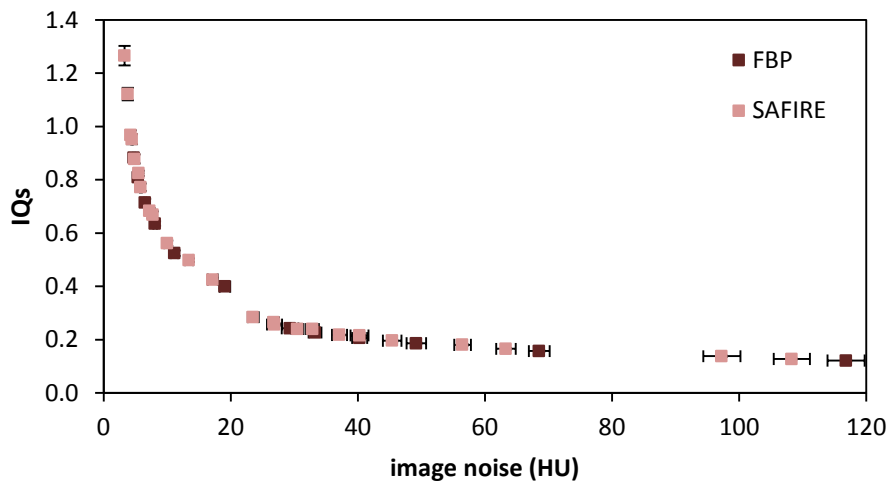


Figure 2 Image quality score (IQs) as a function of image noise. To measure SD, a circular ROI of 10 mm was used in the uniform acrylic background of the Catphan[®] CTP404 module. Scans were made at fixed exposure values increasing from 12 to 200 mAs. Both FBP and SAFIRE reconstructions were made (B30, B70, I30/1-3 and I70/1-3). Error bars in the x and y direction represent the SD between noise measurements and IQs calculations on four consecutive slices.

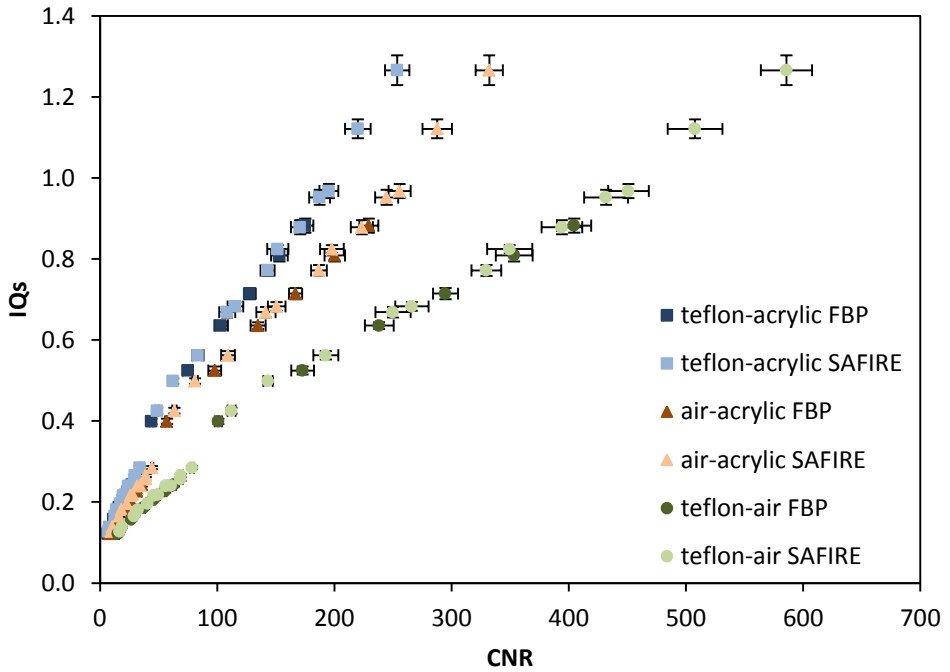


Figure 3 Image quality score (IQs) as a function of contrast-to-noise (CNR) for teflon relative to acrylic, air relative to acrylic and teflon relative to air. Mean pixel values were measured in circular ROIs with a diameter of 10 mm in the Catphan[®] CTP404 module. Scans were made at fixed exposure values increasing from 12 to 200 mAs. Both FBP and SAFIRE reconstructions were made (B30, B70, I30/1-3 and I70/1-3). Error bars in the x and y direction represent the SD between CNR and IQs calculations on four consecutive slices.

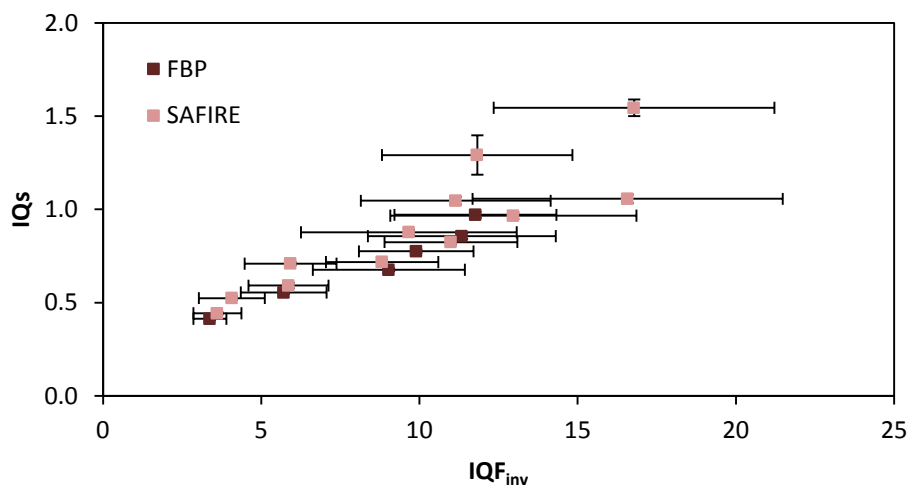


Figure 4 Image quality score (IQs) as a function of mean inverse quality figure (IQF_{inv}). Scans of the CTP515 module were made at fixed exposure values increasing from 12 to 200 mAs. Smooth reconstructions with both FBP and SAFIRE techniques were made (B30 and I30/1-3). Error bars in the x direction represent the SD between the 7 readers. Error bars in the y direction represent the SD between the IQs calculations on four consecutive slices of the Catphan® CTP515 module.

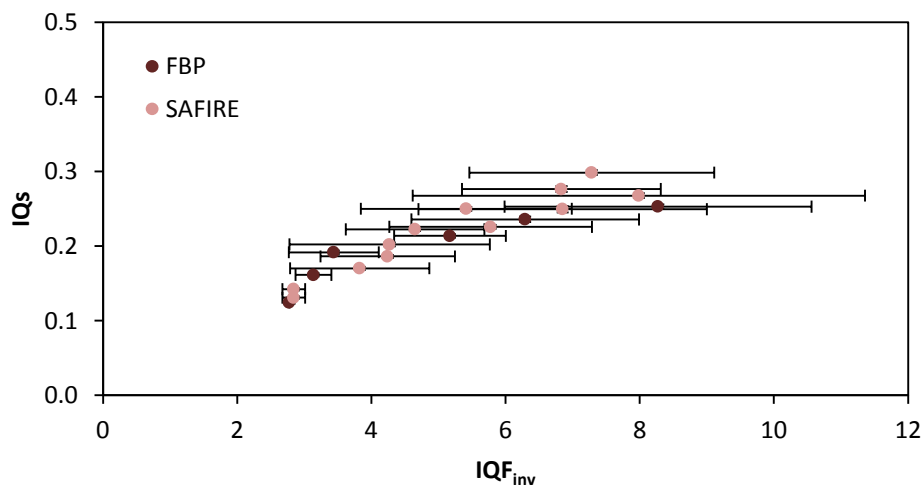


Figure 5 Image quality score (IQs) as a function of mean inverse quality figure (IQF_{inv}). Scans of the CTP515 module were made at fixed exposure values increasing from 12 to 200 mAs. Sharp reconstructions with both FBP and SAFIRE techniques were made (B70 and I70/1-3). Error bars in the x direction represent the SD between the 7 readers. Error bars in the y direction represent the SD between the IQs calculations on four consecutive slices of the Catphan® CTP515 module.

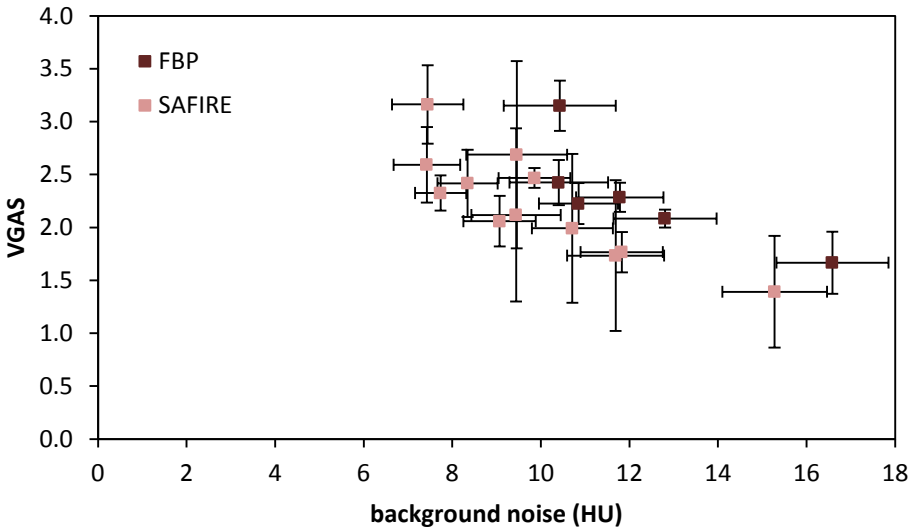


Figure 6 Mean visual grading analysis (VGAS) as a function of background noise. Thiel embalmed cadavers were scanned with increasing reference mAs values from 12 to 150 mAs. Results of the smooth kernels with both FBP and SAFIRE techniques are shown (B30, I30/1 and I30/3). Error bars in the x direction represent the SD between background noise measurements on the different slices of the Thiel stacks. Error bars in the y direction represent the SD between the scoring of the different radiologists.

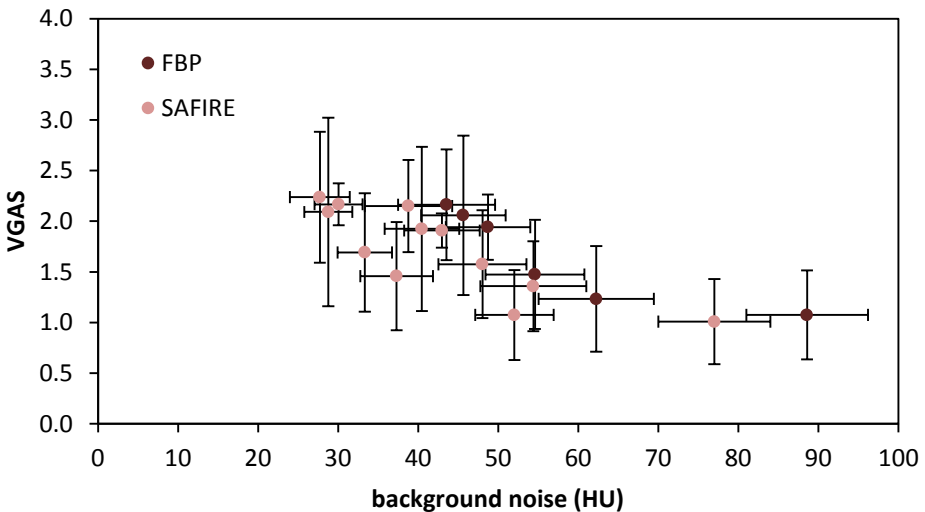


Figure 7 Mean visual grading analysis (VGAS) as a function of background noise. Thiel embalmed cadavers were scanned with increasing reference mAs values from 12 to 150 mAs. Results of the sharp kernels with both FBP and SAFIRE techniques are shown (B70, I70/1 and I70/3). Error bars in the x direction represent the SD between background noise measurements on the different slices of the Thiel stacks. Error bars in the y direction represent the SD between the scoring of the different radiologists.

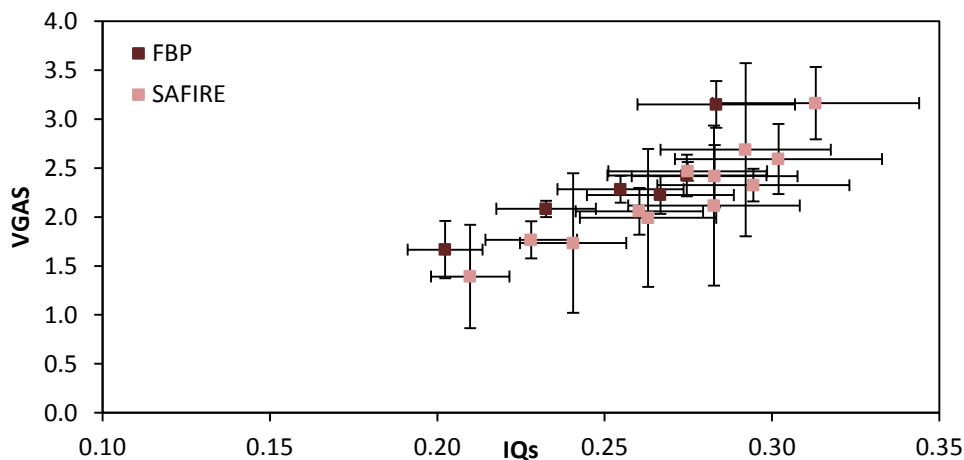


Figure 8 Mean visual grading analysis (VGAS) as a function of image quality score (IQs). Thiel embalmed cadavers were scanned with increasing reference mAs values from 12 to 150 mAs. Results of the smooth kernels with both FBP and SAFIRE techniques are shown (B30, I30/1 and I30/3). Error bars in the x direction represent the SD between the IQs calculations on the different slices of the Thiel stacks. Error bars in the y direction represent the SD between the scoring of the different radiologists.

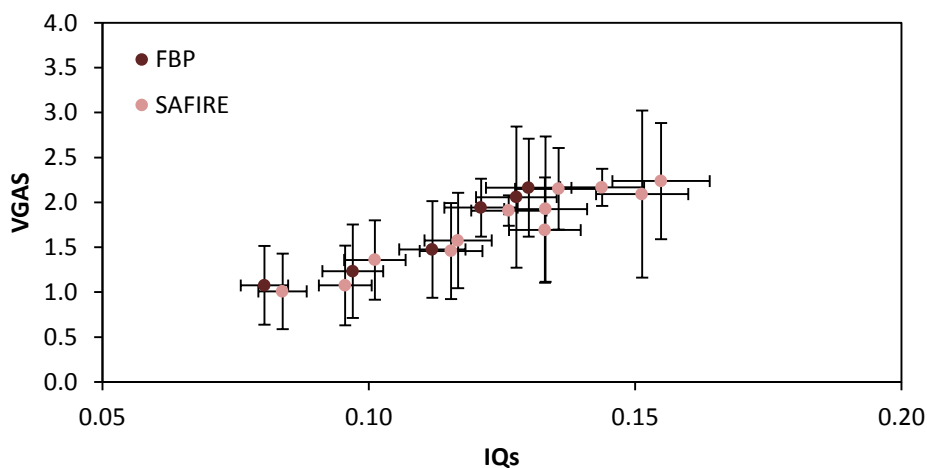


Figure 9 Mean visual grading analysis (VGAS) as a function of image quality score (IQs). Thiel embalmed cadavers were scanned with increasing reference mAs values from 12 to 150 mAs. Results of the sharp kernels with both FBP and SAFIRE techniques are shown (B70, I70/1 and I70/3). Error bars in the x direction represent the SD between the IQs calculations on the different slices of the Thiel stacks. Error bars in the y direction represent the SD between the scoring of the different radiologists.

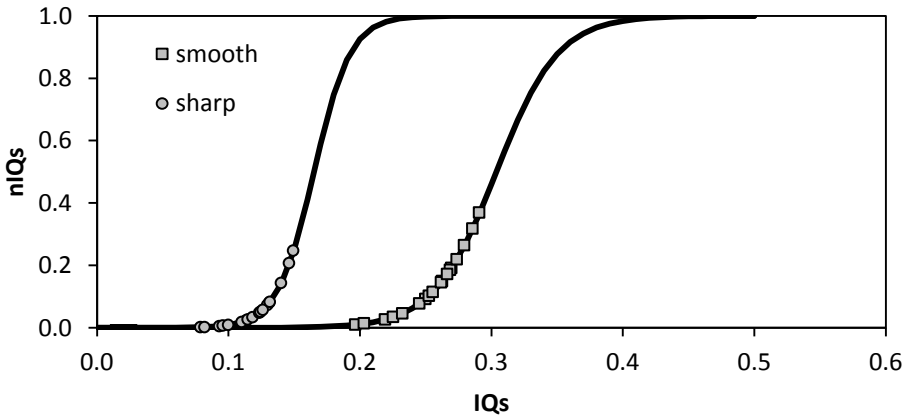


Figure 10 Normalizing sigmoid model (solid line) and normalized image quality score (nIQs) as a function of image quality score (IQs). The IQ scores were calculated on axial CT images of the Thiel embalmed cadavers, reconstructed with both FBP and SAFIRE kernels. Results for the smooth (B30, I30/1 and I30/3; squares) and sharp (B70, I70/1, I70/3; circles) reconstruction filters are shown separately. The bodies were scanned with increasing reference mAs values from 12 to 150 mAs.

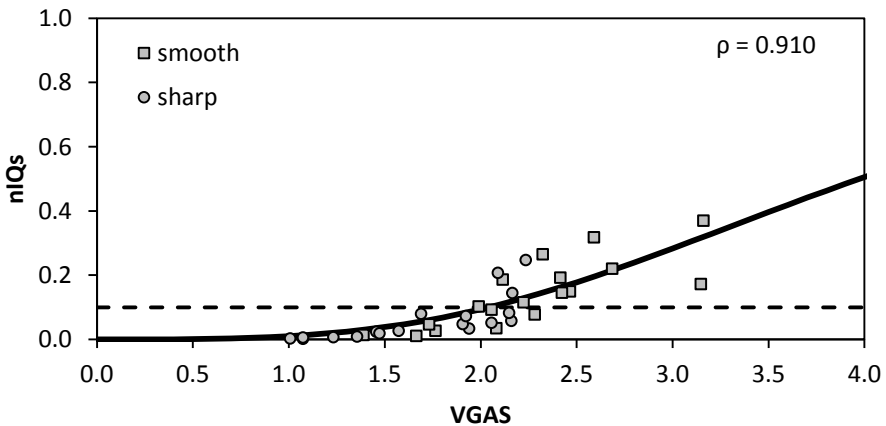


Figure 11 Normalized image quality score (nIQs) as a function of mean visual grading analysis (VGAS). Images with an nIQs of less than 0.1 (dashed line) do not meet the diagnostic requirements. Thiel embalmed cadavers were scanned with increasing reference mAs values from 12 to 150 mAs. Results for the smooth (B30, I30/1 and I30/3; squares) and sharp (B70, I70/1, I70/3; circles) reconstruction filters are shown. The regression curve $nIQs = VGAS^a / (VGAS^a + b)$ was fitted to the data. ρ = Spearman's rank correlation coefficient ($p < 0.001$).

DISCUSSION

Our study focuses on the evaluation of IQ in chest CT, by using the method of Kortensniemi et al [8]. This automatic algorithm calculates an image quality score (IQs) for each acquired dataset. The tool requires no human interaction and can run in the background on the CT console. The authors showed a correlation between IQs and image noise [8]. However, it was unclear to what extent this methodology was suitable for IQ evaluation in clinical practice. Therefore, our study is an addition to the research of Kortensniemi et al, using human cadavers to mimic clinical conditions. To our knowledge, the relationship between IQs and clinical IQ, expressed as VGAS, was never assessed before.

Several studies tried to determine the link between clinical and physical-technical IQ in thoracic CT imaging [9,10,15]. Christianson et al developed an automated algorithm to measure noise in CT images [9]. Although the proposed method can be used for protocol optimization, the authors did not take into account the clinical IQ of the recorded datasets. In the study of Tian and Samei another technique to measure quantum noise in clinical CT images was proposed [10]. Both above-mentioned studies do not allow a direct comparison of datasets reconstructed with different kernels. Sharp reconstructions will have a better spatial resolution, compared to smooth reconstructions. However, as a compromise, these datasets will appear more noisy. Depending on the clinical task, sharp kernels may be preferred, despite the increase in image noise. Using the methods of Christianson and Tian, sharp reconstructions will unfairly be classified as images of lesser quality.

Using human cadavers, De Crop et al reported good correlations between VGAS on the one hand and noise, CNR and contrast-detail on the other hand [15]. However, the used physical metrics are calculated using technical phantoms. As a consequence, evaluating a clinical dataset with the proposed technique requires additional phantom scans.

Our goal was to evaluate an automatic IQ scoring tool for use in clinical practice with chest CT scans. First, a Catphan study was set up for performance evaluation of the algorithm. Next, the automatic scoring algorithm was applied on clinical images of Thiel embalmed cadavers. An addition to the study of Kortensniemi et al is the inclusion of iteratively reconstructed images in our manuscript. In order to compare our findings, correlations were calculated separately for FBP and SAFIRE images (Table 4). As the exposure to the patient increases, the amount of noise in the image will diminish. If SAFIRE is used, the image noise will further decrease, smoothing the image at the expense of spatial resolution [19]. If the amount of noise in the image is reduced, IQs values will be higher. However, iterative reconstructions alter the image texture in different clinically relevant contrast and detail levels. A blotchy image quality impression is commonly reported by radiologists and this effect is more marked when a greater iterative strength is applied

[20]. Therefore, using SAFIRE, the observed IQ, expressed as IQ_{inv} or VGAS, will not follow the same trend as the IQs scores. This can explain the different correlations for FBP and iterative algorithms (Table 4).

Our study showed excellent correlations between image noise and CNR on the one hand and IQs on the other hand. These findings confirm the results of Kortesiani et al [8]. The observed relationships were expected, as the calculation of IQs is based mainly on local standard deviations. Our results suggest that manually selecting ROIs in a technical phantom to evaluate noise and CNR is no longer necessary. An automatic IQs calculation can be sufficient. In addition, IQs correlates highly with the contrast-detail analysis, performed by 7 experienced human readers (Figures 4-5, Table 4). Image noise reduces the detectability of low contrast objects [6]. Therefore, contrast-detail is dependent on the amount of noise in the image which can explain the observed correlation.

The relationship between IQs and clinical IQ, expressed as VGAS, was investigated. Performing the automatic analysis only on the slices of the Thiel cadavers used in the visual grading study, resulted in strong correlations with VGAS. Including all images of each Thiel stack, correlates even stronger with the observed clinical image quality. The latter method, which will be used in clinical routine, is shown in Figures 8 and 9. Sharp reconstructions generate more noisy images, yet increase the spatial resolution. Despite the increased noise, contrast-detail inserts are still detectable to a certain extent. For some clinical tasks, the IQ will improve by using a sharp kernel. This can explain the different correlations for both filters, noticed in the contrast-detail study, background noise measurements and VGA analysis.

As a consequence, it is not possible to use IQs as a parameter to compare different reconstruction kernels. Normalizing the image quality score is a possible solution. In this study the normalization was done using a dataset that just meets the diagnostic requirements ($VGAS = 2$) and a reference dataset ($VGAS = 3$). A normalized IQs (nIQs) of respectively 0.1 and 0.5 was assigned to these acquisitions. The criteria used to calculate VGAS consist of a mix of low- and high-contrast structures (Table 2). Therefore, using VGAS as a parameter in the normalization model is a well-considered choice.

Our study demonstrates the use of an image quality score in clinical routine. The (n)IQs score can be stored in a database and used to monitor the IQ performance over time. The scores can be compared to a reference image or to other score values from patients scanned with the same protocol. Subtle changes in IQ may not be noticed by a human observer, but can be detected by setting appropriate alerts in a quality management environment.

Finally, we assessed the possibility of using background noise as a simple metric to evaluate the IQ of a CT dataset. The observer performance (VGAS) correlated more strongly with IQs than with background noise. Monitoring IQ using background noise should be used with care. Because of the nonstationarity of CT noise in the reconstructed

images, measuring noise is location dependent [21,22]. Changes in IQ in the centre of the image are not necessarily reflected in the air signal, surrounding the patient. The results of this study indicate that IQs is preferable to background noise as a parameter for automatic evaluation of CT image quality.

The use of unenhanced images can be seen as a limitation. It is possible that the correlation between IQs and VGAS is influenced by the use of contrast agents. Because edges and high-noise areas are excluded from the calculation, the effect of contrast agents on the IQs will be rather small. However, using enhanced images can result in a significant improvement of the image quality.

In conclusion, the automatic scoring algorithm is a promising tool for the evaluation of thoracic CT scans in daily clinical practice. It allows monitoring of the image quality of a chest protocol over time, without human intervention. Different reconstruction kernels can be compared after normalization of the image quality score.

FUNDING

This work was supported by the Agency for Innovation by Science and Technology (IWT) [grant number 121663].

REFERENCES

- 1 Brenner DJ (2010) Slowing the Increase in the Population Dose Resulting from CT Scans. *Radiat Res* 174:809-815
- 2 McCollough CH (2016) The Role of the Medical Physicist in Managing Radiation Dose and Communicating Risk in CT. *AJR Am J Roentgenol* 206:1241-1244
- 3 (2016) DoseWatch. GE Healthcare. Available via http://www3.gehealthcare.com/en/products/dose_management/dosewatch/. Accessed 01.12.2016
- 4 (2015) TQM Dose. Qaelum NV, Leuven, Belgium. Available via <http://www.qaelum.com/>. Accessed 01.12.2016
- 5 (2016) Radimetrics Enterprise Platform. Bayer HealthCare LLC. Available via <https://www.radiologysolutions.bayer.com/products/ct/dosemanagement/rep/>. Accessed 01.12.2016
- 6 Verdun FR, Racine D, Ott JG et al (2015) Image quality in CT: From physical measurements to model observers. *Phys Med* 31:823-843
- 7 Beutel J (2000) Handbook of medical imaging. SPIE Press, Bellingham, Wash.
- 8 Kortensniemi M, Schenkel Y, Salli E (2008) Automatic image quality quantification and mapping with an edge-preserving mask-filtering algorithm. *Acta Radiol* 49:45-55
- 9 Christianson O, Winslow J, Frush DP, Samei E (2015) Automated Technique to Measure Noise in Clinical CT Examinations. *AJR Am J Roentgenol* 205:W93-99
- 10 Tian X, Samei E (2016) Accurate assessment and prediction of noise in clinical CT images. *Med Phys* 43:475
- 11 Thiel W (1992) The preservation of complete cadavers without loss of natural color. *Annals of Anatomy-Anatomischer Anzeiger* 174:185-195
- 12 Thiel W (2002) Comment on the preservation of complete cadavers according to W. Thiel. *Annals of Anatomy-Anatomischer Anzeiger* 184:267-269
- 13 Samei E, Badano A, Chakraborty D et al (2005) Assessment of display performance for medical imaging systems: executive summary of AAPM TG18 report. *Med Phys* 32:1205-1225
- 14 Thijssen M, Bijkerk K, van der Burght R (1998) Manual Contrast-Detail Phantom Artinis CDRAD type 2.0.
- 15 De Crop A, Smeets P, Van Hoof T et al (2015) Correlation of clinical and physical-technical image quality in chest CT: a human cadaver study applied on iterative reconstruction. *BMC Med Imaging* 15:32
- 16 De Crop A, Bacher K, Van Hoof T et al (2012) Correlation of contrast-detail analysis and clinical image quality assessment in chest radiography with a human cadaver study. *Radiology* 262:298-304
- 17 Commission of the European Communities (1999) European guidelines on quality criteria for computed tomography (EUR 16262).
- 18 Commission of the European Communities (1990) CEC quality criteria for diagnostic radiographic images and patient exposure trial (EUR 12952 EN).
- 19 Beister M, Kolditz D, Kalender WA (2012) Iterative reconstruction methods in X-ray CT. *Phys Med* 28:94-108

- 20 Ghetti C, Palleri F, Serreli G, Ortenzia O, Ruffini L (2013) Physical characterization of a new CT iterative reconstruction method operating in sinogram space. *J Appl Clin Med Phys* 14:4347
- 21 Hsieh J (1997) Nonstationary noise characteristics of the helical scan and its impact on image quality and artifacts. *Med Phys* 24:1375-1384
- 22 Zeng R, Gavrielides MA, Petrick N, Sahiner B, Li Q, Myers KJ (2016) Estimating local noise power spectrum from a few FBP-reconstructed CT scans. *Med Phys* 43:568

Chapter 8

Patient-specific dose and risk estimation for organ-based tube-current modulation in chest CT

Caro Franck¹, Peter Smeets², Lore Lapeire³, Eric Achten², Klaus Bacher¹

¹ Department of Medical Physics
Ghent University, Belgium

² Radiology Department
Ghent University Hospital, Belgium

³ Department of Medical Oncology
Ghent University Hospital, Belgium

ABSTRACT

Purpose To retrospectively assess the potential dose reduction to the thyroid and breasts in chest CT, using organ-based tube-current modulation (OBTCM). Posterior organs in the field of view are analysed and overall lifetime attributable risk (LAR) of cancer induction and mortality is evaluated.

Materials and Methods The location of the breasts with respect to the reduced tube-current zone was determined. Using Monte-Carlo simulations, patient-specific dose distributions of chest CT scans were calculated for 50 female patients (mean age $53.7y \pm 17.5$, range 20-80y). The potential dose reduction of OBTCM was assessed. In addition, simulations of clinical OBTCM scans were made for 17 female patients (mean age $43.8y \pm 17.1y$, range 20-69y). LAR of cancer incidence and mortality was estimated according to BEIR-VII. Image quality (IQ) between standard and OBTCM scans was compared.

Results No women had all breast tissue within the reduced tube-current zone. Clinical observed dose reductions were 18% (thyroid) and 9% (breasts) whereas lung, liver and kidney doses increased with 17%, 11% and 26%, respectively. Overall, the difference in LAR for cancer incidence was not statistically significant ($p=0.06$) between conventional and OBTCM scanning. IQ improved with OBTCM ($p<.01$).

Conclusion The potential benefit of OBTCM to the female breast in chest CT is overestimated as the reduced tube-current zone is too limited. Despite a 9% reduction of the breast dose, posterior organs will absorb to 26% more dose, resulting in no additional benefit for reduction of radiation induced malignancies.

INTRODUCTION

Significant differences exist in sensitivity to radiation induced cancer among the organs and tissues of the human body (1). The thyroid and female breast show a relatively high radiosensitivity, whereas muscles and connective tissue have a relatively low susceptibility to ionizing radiation. In 2007, the International Commission on Radiological Protection increased the tissue weighting factor for the breasts from 0.05 to 0.12, stating breast tissue is more sensitive to ionising radiation than previously assumed [1].

To keep the risks as low as reasonably achievable, in mammography screening, the average glandular dose per acquisition is kept below 2.5mGy [2]. On the other hand, in chest CT, the breasts are located in the FOV and receive significantly higher doses in the range of 10-15mGy [3,4].

With organ-based tube-current modulation (OBTCM), the exposure is decreased when the x-ray tube passes over the anterior surface of the patient. In this way, the dose to the breast can be limited. However, to preserve image quality, the total exposure during one rotation has to be equal to the exposure of scans without OBTCM enabled. Therefore, the tube-current is increased during posterior projections, leading to a photon flux at the detector equivalent to scans without OBTCM [5-7].

Significant dose reductions for anteriorly positioned organs using the OBTCM technique have been stated in literature [5,6,8,9]. In particular, reported breast dose reductions vary from 16 to 50% (Table 1). However, all of these studies are based on measurements and calculations in anthropomorphic phantoms, which differ from clinical reality. In fact, the breast position in phantoms is typically centred anteriorly and does not reflect the real breast position in women lying in a supine position [10,11]. In the study of Taylor et al, none of the women had all breast tissue within the reduced-dose zone, raising substantial concerns regarding the potential of OBTCM to reduce CT irradiation of breast tissue successfully [11].

In addition, at the expense of the reduced exposure of anteriorly positioned organs like breasts and thyroid, doses to posterior tissues will increase [9]. As a result, it is unclear what will be the overall effect of OBTCM on the risk of radiation induced malignancies compared to conventional CT scan techniques [5].

To our knowledge patient-specific dosimetry data linked to OBTCM is missing in the literature. Therefore, the aim of the study was to assess the impact of OBTCM on patient dose and radiation risks for women undergoing chest CT by means of Monte-Carlo simulations and individualized patient voxelmodels.

Table 1 Organ dose reduction using OBTCM, reported in the literature. Negative values indicate a dose increase.

	dose reduction with OBTCM (%)				
	thyroid	breast	lung	liver	kidney
Ketelsen et al [6]	20	35	-2	19	
Gandhi et al [12]		29	1		
Euler et al [10]		16			
Wang et al [9]		39			
Vollmar and Kalender [8]		50			
Present study	18	9	-17	-11	-26

MATERIALS AND METHODS

Organ-based tube-current modulation

The OBTCM system under investigation (X-CARE, Siemens Healthcare, Germany), aims to lower the radiation dose delivered to anteriorly located organs (e.g. eye lenses, thyroid and breasts). Within a range of 80° the tube-current is limited to 25% of the mean value. Posteriorly, within a range of 240° , the exposure is increased to 125% to compensate for the reduced photon flux at the detector. On either side of the patient, a transition of 20° exists between the low and high current zone. According to the manufacturer, this transition occurs linear, so that 100% of the mean value is reached at 55° on either side of the patient. A schematic overview of the angular tube-current modulation used by X-CARE is given in Figure 1.

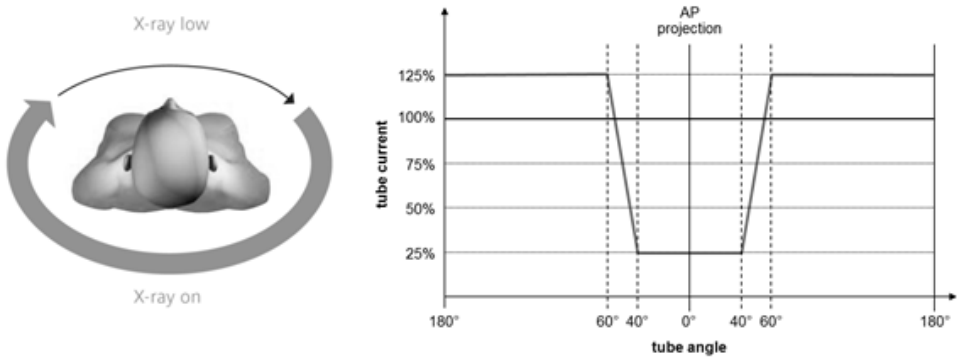


Figure 1 X-Care reduces the dose to anteriorly located organs by lowering the tube-current in the axial plane within a range of 80°. To maintain image quality, the tube-current is increased during the lateral and posterior part of the body circumference. Relative mA values are shown, normalized to the average tube-current during one rotation (data from Siemens Healthcare, Germany).

Patients and voxelized phantoms

For the individualized dose calculations of chest CTs, patient-specific voxelmodels were set up based on clinical CT data. The retrospective use of the CT images was approved by the institutional ethical committee.

As in conventional chest CT the image data are limited to the thoracic region, no image information is available regarding the rest of the body. Therefore, non-contrast-enhanced chest-abdomen-pelvis (CAP) CT scans were selected, used for follow-up of oncologic patients with sarcomas. In our institution this scan is performed in two acquisitions: a chest scan starting from the lung apex to the kidneys, followed by an abdominopelvic scan with image coverage defined from the liver top to the ischium. As a result, the created voxelmodels cover a significant fraction of the total body which is important (1) to accurately incorporate scatter in the dose calculations and (2) to calculate organ doses out of the field-of-view (FOV).

Standard CT acquisition

In this study, CAP CT images of 50 consecutive female patients (mean age 53.7 ± 17.5 y, range 20-80y; mean BMI 24.9 ± 4.3 , range 17.9-37.8) were collected in the PACS system. Scanning parameters of the chest acquisition include 120kVp, 330ms rotation time, 170 quality ref mAs (QRM), 38.4mm collimation, 0.9 pitch and 3mm slice thickness. All scans were performed on a Definition Flash CT, using tube-current modulation (CareDose4D, Siemens Healthcare, Germany). With the available CAP datasets, a patient-specific 3D voxelmodel was created for each subject. The models ranged from the lung apex to the ischium with a voxelsize of $0.7 \times 0.7 \times 3.0 \text{mm}^3$. Exposure data in the DICOM header of the images were used as input for the Monte-Carlo simulations.

OBTCM CT acquisition

In our hospital, the X-CARE algorithm was gradually introduced in the CT acquisitions of female patients for oncologic staging purposes. Scanning parameters were 120kVp, 285ms rotation time, 170 QRM, 38.4mm collimation, 0.6 pitch and 3mm slice thickness.

For 17 of the 50 female patients (mean age 43.8 ± 17.1 y, range 20-69y; mean BMI 24.9 ± 4.9 , range 17.9-37.8) data of both a OBTCM CAP CT scan and a CT scan with conventional TCM approximately 6 months earlier were available. From the OBTCM data, patient-specific voxelmodels were created in a similar way as for the standard acquisitions and OBTCM exposure data were retrieved from the DICOM headers.

Monte-Carlo simulation

To estimate organ doses, resulting from the acquired chest scans, Monte-Carlo simulations were performed. The validated patient-specific dose calculation software ImpactMC [13] was used to this end [14-16]. A schematic overview of the selected patients and the performed simulations is given in Figure 2.

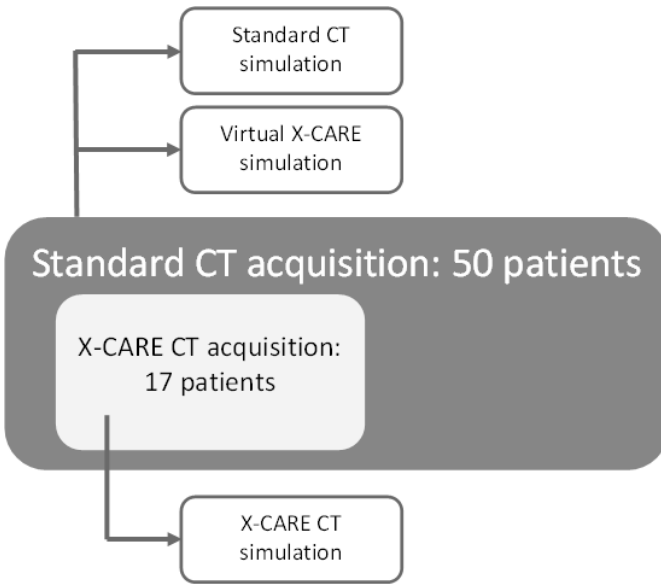


Figure 2 Schematic overview of the performed CT acquisitions and simulations.

Z-axis TCM was integrated for all simulations by extracting mA/slice values from the DICOM headers. With a slice thickness of 3mm and a table feed of 34.56mm, 11 exposure values were extracted per rotation. Modulation in the transverse plane, according to Figure 1, was applied for X-CARE. Finally, a 3D dose distribution was generated, considering all relevant interaction processes and dose depositions of a large number of photons (10^9). This includes photoelectric effect, Compton and Rayleigh scattering [14,15].

In the present study, three chest scans were simulated: (1) the standard acquisition, performed on the complete population of 50 patients; (2) a virtual X-CARE scan, using the same voxelmodels and parameters as in (1) but with XY-modulation as depicted in Figure 1 and (3) the clinical X-CARE acquisition, performed on 17 patients that actually received an OBTCM scan. The second simulation shows the potential dose reduction, while the third simulation demonstrates the use of X-CARE in clinical practice.

Organ dose and risk estimation

Organs in the FOV (thyroid, breasts, lungs, liver and kidneys) were delineated manually on the original images of all patients. These regions of interests (ROIs) were used to determine mean organ doses on the output of the simulations. All other tissue was classified as remainder. Individual overall lifetime attributable risk (LAR) of cancer incidence and mortality was estimated according to the BEIR-VII models [17]. Age-dependent incidence and mortality rates were taken into account.

Breast angle

Internal and external angles for left and right breasts were measured according to the method of Taylor et al (Figure 3) [11]. The vertex was placed on the isocenter of the image, one side of the angle along the y-axis and the other along the tangential line with the inner and outer aspects of the glandular tissue.

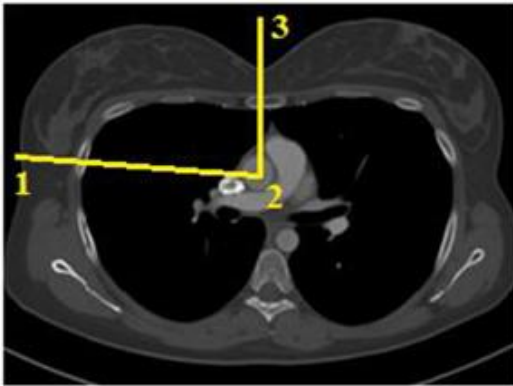


Figure 3 Internal and external breast angles were measured by placing the vertex (2) on the isocenter of the image. One side of the angle was aligned along the y-axis (3) and the other side along the tangential line with the inner or outer aspects of the glandular breast tissue (1).

Image quality evaluation

To objectively assess the image quality (IQ) of the acquired CT examination, an overall image noise index score was calculated based on an edge-preserving mask algorithm on the full image data set, as described in [18]. This validated method allows clinical IQ evaluation of chest scans [19] as an alternative for noise evaluation in predefined ROIs.

Statistical analysis

Organ doses, LARs and IQ scores were compared using a Wilcoxon signed-rank test for matched samples. A p-value <0.05 was regarded as significant. Statistical tests and post-hoc power analyses were performed with SPSS and G*power respectively [20-22].

RESULTS

Internal and external angle measurements for left and right breasts are shown in Figure 4. Mean external and internal angles were $83^{\circ}\pm 7^{\circ}$ and $22^{\circ}\pm 13^{\circ}$ for the left breast and $84^{\circ}\pm 8^{\circ}$ and $16^{\circ}\pm 11^{\circ}$ for the right breast, showing none of the women had all breast tissue located within the reduced dose zone.

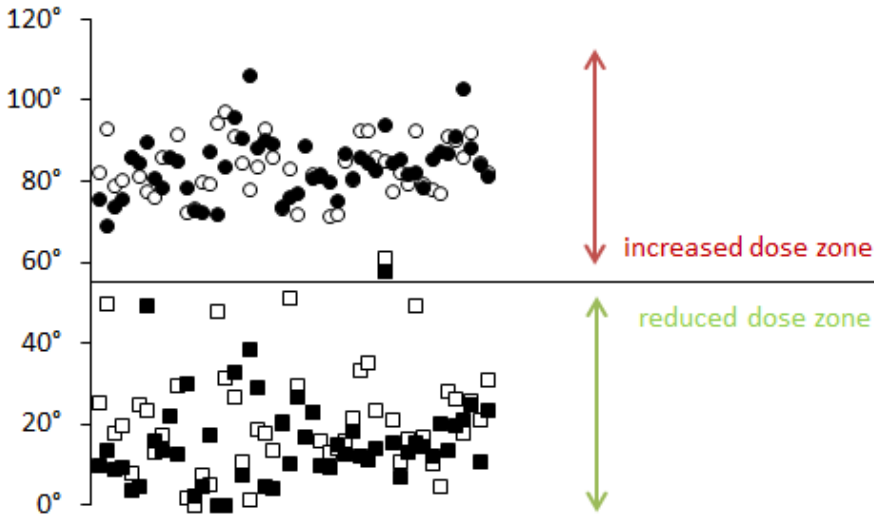


Figure 4 Internal (squares) and external (circles) angle measurements for the left (white) and right breast (black). On either side of the patient, the tube-current is limited to 25-100% of the mean value within a range of 55°. The tube-current is increased to 100-125% during the remaining lateral and posterior projections.

Mean organ doses of standard and virtual X-CARE scans of 50 patients are displayed in Table 2 and Figure 5. The OBTCM simulation resulted in a statistically significant dose reduction to the thyroid (28%), breasts (18%), lungs (4%) and liver (10%) ($p < .001$). A statistically significant increase in kidney dose of 6% is observed ($p < .001$).

Table 2 Mean organ dose and potential mean % dose reduction. Standard chest scans and virtual X-CARE simulations are compared. Negative values indicate a dose increase. Dose differences are statistically significant ($n = 50, p < .001$).

n = 50	organ dose (mGy)		Potential dose reduction %
	standard acquisition	virtual X-CARE	
thyroid	18 ± 8	13 ± 5	28 ± 4
breast	15 ± 5	12 ± 4	18 ± 4
lung	14 ± 5	13 ± 4	4 ± 3
liver	13 ± 4	12 ± 4	10 ± 4
kidney	11 ± 3	12 ± 4	-6 ± 7

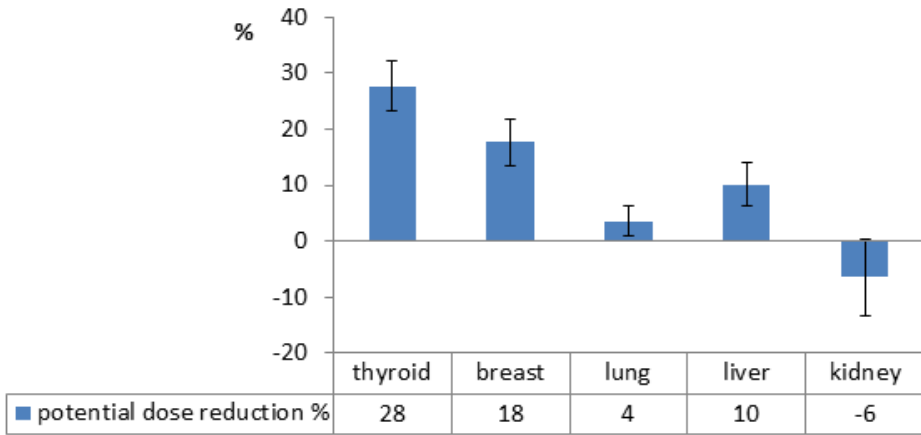


Figure 5 Mean dose differences between standard chest scans and theoretical X-CARE simulations. The same patient voxelmodels and acquisition parameters were used for both simulations. Modulation in the transverse plane was applied for the X-CARE simulations, according to Figure 1. Positive values represent a dose reduction using X-CARE, whereas negative values indicate a dose increase. Dose differences are statistically significant (n = 50, p < .001).

Table 3 presents the mean organ doses of standard CT and clinically performed X-CARE scans in 17 patients. Virtual X-CARE simulation results of the same patients are shown for comparison. Dose differences between standard and OBTCM, displayed in Table 2 and Figure 6, were statistically significant (p<.05). The observed dose reductions were 18% (thyroid) and 9% (breasts). Lung, liver and kidney dose increased with 17%, 11% and 26% respectively.

Table 3 Mean organ dose and mean % dose reduction. Standard chest scans and X-CARE simulations are compared. To compute the potential dose reduction, the same patient voxelmodels and scan parameters are used as for the standard scans. The clinical dose reduction is based on the available CT data of 17 patients. Negative values indicate a dose increase. Dose differences are statistically significant (n = 17, p < .05).

n = 17	organ dose (mGy)			Potential dose reduction (%)	Clinical dose reduction (%)
	standard acquisition	virtual X-CARE	X-CARE acquisition		
thyroid	21 ± 8	15 ± 6	17 ± 7	28 ± 5	18 ± 32
breast	17 ± 3	14 ± 3	16 ± 3	18 ± 3	9 ± 10
lung	15 ± 3	14 ± 3	17 ± 3	4 ± 2	-17 ± 19
liver	15 ± 3	13 ± 1	16 ± 2	10 ± 4	-11 ± 14
kidney	13 ± 1	14 ± 1	16 ± 2	-4 ± 3	-26 ± 18

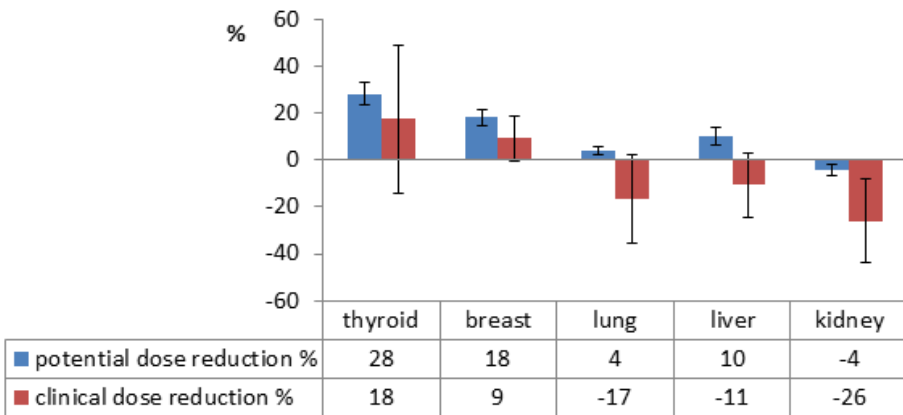


Figure 6 Mean dose differences between standard chest scans and X-CARE simulations. The comparison with the theoretical X-CARE simulations is depicted in blue, where the same patient voxelmodels and acquisition parameters were used as for the standard scans. Clinical X-CARE simulations (red) are based on the available CT data of 17 patients. Modulation in the transverse plane was applied for all X-CARE simulations, according to Figure 1. Positive values represent a dose reduction using X-CARE, whereas negative values indicate a dose increase. Dose differences are statistically significant (n = 17, p < .05).

Overall, the acquisitions with clinically performed OBTCM resulted in no significant differences in LAR for cancer incidence as compared to the conventional scan technique ($p=.062$). A small but significant increase in LAR mortality ($p<.01$) was calculated (Table 4). However, significance was achieved with an extremely low statistical power (0.34).

Table 4 Mean LAR of cancer incidence and mortality. Standard chest scans and X-CARE simulations are compared.

n=17	mean	SD	p-value
	‰	‰	
LAR incidence			0.062
standard acquisition	1.08	0.64	
X-CARE acquisition	1.16	0.67	
LAR mortality			0.006
standard acquisition	0.60	0.23	
X-CARE acquisition	0.67	0.25	

IQ evaluation revealed a significant improved noise parameter when scanning with OBTCM (average improvement of the IQ scores of 7% , $p<.01$, statistical power 0.99).

DISCUSSION

With a calculated breast dose of 15mGy, our study is in line with previous results for chest CT found in the literature, where doses range from 10 to 28mGy [3,4,23-25]. These numbers are 4 to 11 times higher than the EUREF limiting value of 2.5mGy for average glandular dose in screening mammography [2]. Since the breasts are rarely the object of interest in chest scans, concern is raised about the elevated population risk of breast cancer incidences from CT. OBTCM aims to lower the exposure to anterior organs thus reducing the absorbed breast dose. Our goal was to critically assess the efficacy of OBTCM in chest CT for female patients. Doses to all relevant organs in the FOV are calculated and overall risk of cancer incidence and mortality is evaluated. To our knowledge, no patient studies exist assessing the increased dose to the posterior organs resulting OBTCM scans. Our work uses clinical data to create patient-specific voxelized models and to assess individual organ doses. Moreover, scans with and without OBTCM are performed on the same subjects.

X-CARE reduces the exposure during anterior tube positions, within a range of 80°. Yet breast tissue in supine positioned women is more lateral and extends beyond this decreased current zone. Figure 3 confirms the results of Taylor [11], showing none of the women had all breast tissue located within the reduced dose zone. Wearing a brassiere increases the percentage of breast tissue within this region and, therefore, improves the performance of OBTCM. According to the study of Seidenfuss, women with cup size E have the largest effect of wearing a brassiere, increasing the rate of breast tissue that was affected by OBTCM from 30% to 83% [7].

Dose reduction to the female breast using OBTCM and the resulting increase to posterior organs is investigated in the literature with anthropomorphic phantoms [5,6,8,9,12]. Duan et al indicated a rise in posterior surface dose, suggesting a possible lung dose increase [5], whereas Wang et al reported an elevated dose to the spine and lungs with OBTCM [9]. Since the weighting factors for breast, bone marrow and lung are equal [25], the effective dose for a chest CT may not necessarily decrease even though the exposure from the anterior direction is decreased with OBTCM [9]. To determine the overall risk of cancer induction and mortality, several dose calculation tools exist [26-28]. However, these do not allow for TCM in the transverse plane so reducing the exposure during the anterior projections and evaluating the effect of OBTCM is not possible. Furthermore, these calculations are based on pre-tabulated results from Monte-Carlo simulations performed on one female phantom. Considering the diversity among the BMI, cup size and anatomy of the female population, a significant error could be introduced in the obtained results. These drawbacks may be addressed with full Monte-Carlo simulations using models that are specific for each individual patient [29]. To this end, the patient's clinical CT data can be used as a voxelmodel so that all relevant organs can be delineated [14,30].

The Monte-Carlo technique allowed to simulate the potential dose reduction of the X-CARE technique using the exposure parameters (kVp, rotation time, QRM, collimation, pitch and slice thickness) as used for conventional CT scanning, but taking into account the angular TCM for the X-CARE simulations as described in Figure 1. The obtained results showed potential dose reductions for thyroid, breasts, lungs and liver. Since none of the glandular tissue is fully located in the reduced current zone (Figure 4), the potential dose reduction to the female breasts (18%) is less than to the thyroid (28%). Liver dose was reduced (10%) by the use of X-CARE, whereas the dose to the kidneys increases with 7%. Although a possible lung dose increase was suggested by [5], our study predicts a reduction of 4% with OBTCM.

However, when the real clinical exposure data from OBTCM CT scans are used, other conclusions are found. First of all, an overall increase in $CTDI_{vol}$ was noticed between standard and X-CARE acquisitions. Even though kVp, QRM, beam collimation and reconstructed slice thickness were maintained, an average increase in exposure values of 15% was noticed. Wang et al observed a comparable rise in mAs of 5%-10%, with a maximum of 20% [9]. Whereas in the transverse plane TCM adjusts the exposure

according to the size and density of the patient for each projection, OBTCM only uses two different exposure values per rotation (Figure 1). In this way, OBTCM is less dose efficient because the exposure values are defined a priori and not adjusted angularly for each patient's specific shape and attenuation. Since the QRM is maintained for both acquisitions, the same IQ-level is requested. Because of the differences in dose efficiency, this can result in an increased $CTDI_{vol}$ for OBTCM [9]. The overall increase in $CTDI_{vol}$ results in less dose reduction as compared to the theoretical X-CARE simulations previously performed. Dose reductions to superficial and anterior located organs are still observed, yet to a lesser extent. Thyroid dose decreases with 18%, whereas the reduction to the breasts is only 9%. Doses to other relevant organs in de FOV increased with the use of X-CARE. Liver, lungs and kidneys experience an increase of 11%, 17% and 26% respectively. An overview of the dose reducing potential of OBTCM reported in the literature is given in Table 1. All studies were performed on anthropomorphic phantoms where the breasts are typically centred anteriorly and fully located in the reduced current zone [6,8-10,12]. The real position of the breasts in women lying supine is more lateral and explains the lower potential for breast dose reduction observed in the present study.

As stated before, the overall risk for a chest CT may not necessarily decrease with the use of OBTCM [9]. With X-CARE the focus is put on breast and thyroid dose reduction. However, it is shown in our study that liver, lung and kidney dose will increase. To determine the overall risk of radiation induced malignancies, from an OBTCM-based examination, LAR for cancer induction and mortality were calculated for all patients. Our data suggests no significant overall benefit for radiation induced cancer risks when comparing OBTCM with standard CT acquisitions. Mortality risks were significantly higher in the X-CARE group, but the differences are associated with an extremely low statistical power. Consequently, conclusions about mortality risk estimates should be taken with care.

Apart from dose, image quality should be taken into account when evaluating new technologies. Studies on anthropomorphic phantoms found no significant differences in objective IQ between scans with and without OBTCM [5,6,8]. However, these conclusions are based on noise measurements in predefined ROIs. The method used in this study is based on the local SD of every pixel in the entire image. A clear link with subjective clinical IQ in chest CT is described before [19]. Despite the same QRM, the results of the IQs analysis show an improvement of the IQ in the X-CARE group. This can be explained by the increased rise in $CTDI_{vol}$. Consequently, if one aims for the same IQ-level for both standard and OBTCM acquisition, X-CARE exposure values could be reduced.

One of the limitations of our study was the absence of angular TCM information for the standard acquisitions. After extracting the exposure values from the DICOM headers of the available CT datasets, angular TCM was applied to the X-CARE simulations, according to Figure 1, yet no information was available about the in-plane TCM of standard scans. It is possible to determine the exposure values for each projection using the raw data.

However, this information was no longer available during our retrospective study. The number of extracted exposure values (11) per rotation was considered sufficient to simulate the CT acquisitions. In addition, bone marrow dose was not calculated directly, yet included in the remainder. Our study focuses on overall risk estimations, without assessing LAR of individual organs.

In conclusion, the potential benefit of OBTCM to the female breast in chest CT is overestimated as the reduced tube-current zone is too limited. Despite a 9% reduction of the breast dose as observed in our population, posterior organs will absorb to 26% more dose, resulting in no overall benefit for radiation induced cancer risks.

REFERENCES

- 1 (2007) The 2007 Recommendations of the International Commission on Radiological Protection. ICRP publication 103. *Ann ICRP* 37:1-332
- 2 Perry N, Broeders M, de Wolf C, Tornberg S, Holland R, von Karsa L (2008) European guidelines for quality assurance in breast cancer screening and diagnosis. Fourth edition--summary document. *Ann Oncol* 19:614-622
- 3 Gu J, Bednarz B, Caracappa PF, Xu XG (2009) The development, validation and application of a multi-detector CT (MDCT) scanner model for assessing organ doses to the pregnant patient and the fetus using Monte Carlo simulations. *Phys Med Biol* 54:2699-2717
- 4 Zhang Y, Li X, Segars WP, Samei E (2012) Organ doses, effective doses, and risk indices in adult CT: comparison of four types of reference phantoms across different examination protocols. *Med Phys* 39:3404-3423
- 5 Duan X, Wang J, Christner JA, Leng S, Grant KL, McCollough CH (2011) Dose reduction to anterior surfaces with organ-based tube-current modulation: evaluation of performance in a phantom study. *AJR Am J Roentgenol* 197:689-695
- 6 Ketelsen D, Buchgeister M, Fenchel M et al (2012) Automated computed tomography dose-saving algorithm to protect radiosensitive tissues: estimation of radiation exposure and image quality considerations. *Invest Radiol* 47:148-152
- 7 Seidenfuss A, Mayr A, Schmid M, Uder M, Lell MM (2014) Dose reduction of the female breast in chest CT. *AJR Am J Roentgenol* 202:W447-452
- 8 Vollmar SV, Kalender WA (2008) Reduction of dose to the female breast in thoracic CT: a comparison of standard-protocol, bismuth-shielded, partial and tube-current-modulated CT examinations. *Eur Radiol* 18:1674-1682
- 9 Wang J, Duan X, Christner JA, Leng S, Yu L, McCollough CH (2011) Radiation dose reduction to the breast in thoracic CT: comparison of bismuth shielding, organ-based tube current modulation, and use of a globally decreased tube current. *Med Phys* 38:6084-6092
- 10 Euler A, Szucs-Farkas Z, Falkowski AL et al (2016) Organ-based tube current modulation in a clinical context: Dose reduction may be largely overestimated in breast tissue. *Eur Radiol* 26:2656-2662
- 11 Taylor S, Litmanovich DE, Shahrzad M, Bankier AA, Gevenois PA, Tack D (2015) Organ-based tube current modulation: are women's breasts positioned in the reduced-dose zone? *Radiology* 274:260-266
- 12 Gandhi D, Crotty DJ, Stevens GM, Schmidt TG (2015) Technical Note: Phantom study to evaluate the dose and image quality effects of a computed tomography organ-based tube current modulation technique. *Med Phys* 42:6572-6578
- 13 ImpactMC, CT Imaging GmbHCT Imaging, 1.6, Erlangen, Germany
- 14 Chen W, Kolditz D, Beister M, Bohle R, Kalender WA (2012) Fast on-site Monte Carlo tool for dose calculations in CT applications. *Med Phys* 39:2985-2996
- 15 Deak P, van Straten M, Shrimpton PC, Zankl M, Kalender WA (2008) Validation of a Monte Carlo tool for patient-specific dose simulations in multi-slice computed tomography. *Eur Radiol* 18:759-772

- 16 Schmidt B, Kalender WA (2002) A fast voxel-based Monte Carlo method for scanner- and patient-specific dose calculations in computed tomography. *Phys Med* 18:43-53
- 17 Council N (2006) Health risks from exposure to low levels of ionizing radiation: BEIR VII phase 2. The National Academies Press
- 18 Kortensniemi M, Schenkel Y, Salli E (2008) Automatic image quality quantification and mapping with an edge-preserving mask-filtering algorithm. *Acta Radiol* 49:45-55
- 19 Franck C, De Crop A, De Roo B et al (2017) Evaluation of automatic image quality assessment in chest CT – A human cadaver study. *Phys Med* 36:32-37
- 20 IBM SPSS Statistics for Windows, IBM corp, 23.0, NY, USA
- 21 Faul F, Erdfelder E, Buchner A, Lang AG (2009) Statistical power analyses using G*Power 3.1: tests for correlation and regression analyses. *Behav Res Methods* 41:1149-1160
- 22 Faul F, Erdfelder E, Lang AG, Buchner A (2007) G*Power 3: a flexible statistical power analysis program for the social, behavioral, and biomedical sciences. *Behav Res Methods* 39:175-191
- 23 Griglock TM, Sinclair L, Mench A et al (2015) Determining Organ Doses from CT with Direct Measurements in Postmortem Subjects: Part 1--Methodology and Validation. *Radiology* 277:463-470
- 24 Sinclair L, Griglock TM, Mench A et al (2015) Determining Organ Doses from CT with Direct Measurements in Postmortem Subjects: Part 2--Correlations with Patient-specific Parameters. *Radiology* 277:471-476
- 25 ICRP (2000) Managing Patient Dose in Computed Tomography. ICRP publication 87. *Ann ICRP* 30
- 26 ImPACT. Available via www.impactscan.org. Accessed 20/03/2017
- 27 ImpactDose, CT Imaging GmbH, Erlangen, Germany
- 28 CT-Expo, Medizinische Hochschule, Hannover, Germany
- 29 Tian X, Li X, Segars W, Paulson E, Frush D, Samei E (2014) Pediatric Chest and Abdominopelvic CT: Organ Dose Estimation Based on 42 Patient Models. *Radiology* 270:535-547
- 30 Li X, Samei E, Segars WP, Sturgeon GM, Colsher JG, Frush DP (2011) Patient-specific Radiation Dose and Cancer Risk for Pediatric Chest CT. *Radiology* 259:862-874

Chapter 9

The role of Size-Specific Dose Estimate (SSDE) in patient-specific organ dose and cancer risk estimation in paediatric chest and abdominopelvic CT examinations

Caro Franck¹, Charlot Vandevoorde¹, Ingeborg Goethals², Peter Smeets³, Eric Achten³, Koenraad Verstraete³, Hubert Thierens¹, Klaus Bacher¹

¹ Department of Basic Medical Sciences
Ghent University

² Nuclear Medicine Department
Ghent University Hospital

³ Radiology Department
Ghent University Hospital

ABSTRACT

Objectives To develop a clinically applicable method to estimate patient-specific organ and blood doses and lifetime attributable risks (LAR) from paediatric torso CT examinations.

Methods Individualized voxel models were created from full body CT data of 10 paediatric patients (2–18 years). Patient-specific dose distributions of chest and abdominopelvic CT scans were simulated using Monte Carlo methods. Blood dose was calculated as a weighted sum of simulated organ doses. LAR of cancer incidence and mortality were estimated, according to BEIR-VII. A second simulation and blood dose calculation was performed using only the thoracic and abdominopelvic region of the original voxel models. For each simulation, the size-specific dose estimate (SSDE) was calculated.

Results SSDE showed a significant strong linear correlation with organ dose ($r>0.8$) and blood dose ($r>0.9$) and LAR ($r>0.9$). No significant differences were found between blood dose calculations with the full-body voxel models and the thoracic or abdominopelvic models.

Conclusion Even though clinical CT images mostly do not cover the whole body of the patient, they can be used as a voxel model for blood dose calculation. In addition, SSDE can estimate patient-specific organ and blood doses and LAR in paediatric torso CT examinations.

INTRODUCTION

CT examinations are the most important contributors to medical radiation exposure. Despite the fact that only 6 % of the radiological examinations are CT scans, up to 60 % of the radiation dose in medical imaging is delivered by CT [1-4]. Ionizing radiation can cause DNA double-strand breaks in the patient's cells, which are occasionally misrepaired, leading to the induction of cancer [5]. Therefore, concern is raised about the elevated population risk of cancer incidences from CT X-ray exposure. These risks are particularly important for the paediatric population. For about 25 % of all cancers (e.g. leukaemia and thyroid, skin, breast, and brain cancer) children are more radiosensitive than adults [6]. Moreover, they have a longer life span during which the long-term effects of earlier exposure may manifest. So it is necessary to have accurate patient dose estimates to optimize CT scan protocols and to minimize these potential risks.

Volume CT dose index ($CTDI_{vol}$) and dose length product (DLP) are frequently used as dose indicators for CT examinations. To incorporate the patient's size, $CTDI_{vol}$ can be scaled according to the methodology of AAPM Task Groups 204 and 220 [7,8], resulting in a size-specific dose estimate (SSDE). Nevertheless, in order to make conclusions about potential radiation risks associated with CT examinations, accurate individual organ dose estimations need to be available. Dose calculation tools, based on anthropomorphic phantoms, can be used for this purpose. However, for application in paediatric radiology, only standard patient sizes at discrete reference ages can be selected with these software tools [9-12]. Therefore, the use of a more realistic representation of the human anatomy, using a patient-specific voxel geometry, is more appropriate [13]. The latter individualized 3D voxel models can be created based on clinically available CT data of the patient. As the clinical CT range mostly does not cover the whole body of the patient, the created individualized voxel models lack important information on many organs and tissues. It is unclear to what extent this limitation will result in inaccuracies in the risk estimation.

To quantify the radiation effects due to CT examinations, biomarkers in the blood can be used. For example, γ -H2AX foci are formed at sites of DNA double-strand breaks, as a cellular response to ionizing radiation exposure. This can be quantified in the patient's blood lymphocytes, by immunofluorescence microscopy [14], which makes blood dose an important dose quantity. Several studies found a correlation between X-ray induced DNA damage and the patient's blood dose [15-18].

The study's purpose was to estimate patient-specific organ and blood doses and LAR from paediatric chest and abdominopelvic CT examinations, based on (1) full-body voxel models; (2) partial voxel models, limited to the patient's scan range; (3) SSDE, a clinically applicable and easy-to-use metric.

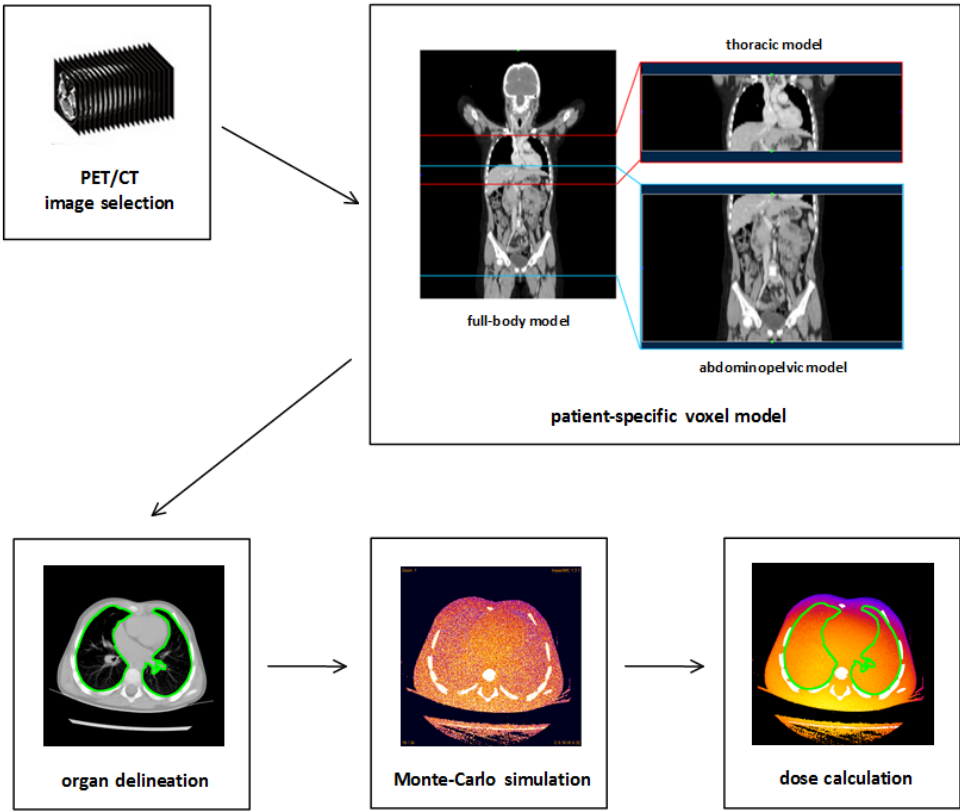


Fig. 1 Full-body CT images were used to create patient-specific 3D voxel models: a full-body, a thoracic, and an abdominopelvic model. Next, individual organs were delineated and used to calculate mean organ doses on the output images of the Monte Carlo simulations

MATERIALS AND METHODS

Patients and voxelized phantoms

Our approach is seen in Fig. 1. We retrospectively used the available full-body CT images from 10 paediatric patients, acquired during PET/CT in the follow-up for non-Hodgkin's lymphoma. The images were recorded on a 16-slice Philips Gemini (Philips Healthcare, the Netherlands). The CT examinations showed no organ disorders or abnormalities. The

subjects were five boys and five girls (range 2–18 years) and were chosen to resemble standard sizes (Table 1). The BMI of the selected patients was representative of their age, according to ICRP 89 [19]. The use of the images was approved by the institutional ethical committee. With these data, a patient-specific 3D full-body voxel model (B) was created for each subject, based on 512×512 DICOM images, with $1.17 \times 1.17 \times 5 \text{ mm}^3$ voxel size.

In conventional CT, the available image data are limited to the patient's scan range, and no information exists regarding the rest of the body. Therefore, two additional voxel models were created for each subject, using only the thoracic (T) and the abdominopelvic region (A) of the original full-body voxel models, to mimic clinical practice (Fig. 1).

Table 1 Summary of study population

Age (years)	Gender	Height (cm)	Weight (kg)	BMI (kg/m ²)
2	F	96	11	11.9
4	M	100	12	12.0
4	F	111	19	15.4
5	M	116	18	13.4
9	F	135	32	17.6
11	M	148	31	14.2
14	M	174	50	16.5
15	F	170	53	18.3
17	F	162	57	21.7
18	M	173	73	24.4

Monte Carlo simulations

Next, to estimate the dose in these voxel models, we performed Monte Carlo simulations. To this end, we used ImpactMC 1.3.1 (CT Imaging, Erlangen Germany), a validated patient-specific dose calculation tool [20-22]. The software calculates a 3D dose distribution in the patient-specific voxel model, considering all relevant photon interaction processes [20,21]. In this way, the dose in each voxel of the model can be assessed and organ and tissue doses can be calculated. The simulation software was calibrated, based on the air kerma measured free-in-air in the isocenter of the CT gantry. For this purpose, a pencil ionization chamber was used (RaySafe Xi CT detector, RaySafe Sweden).

The patient-specific voxel models were imported in the ImpactMC software to simulate fictitious CT examinations. A Siemens Somatom Definition Flash CT (Siemens Medical Solutions, Germany) was modelled in the simulation software: centre of rotation (COR), collimation, distance focus to COR, shaping filter and X-ray spectrum were specified. Helical scans were simulated at 80, 100 and 120 kVp. Scan time was 330 ms, FOV 500 mm, collimation 38.4 mm and pitch 0.9 (Table 2). Nowadays, tube current modulation (TCM) is employed for most paediatric clinical protocols. In order to integrate this technique in the simulation software, mA/slice values were extracted for each patient from the DICOM headers of the recorded CT images. For the abdominopelvic scan, the simulation started at the liver top and ended at the ischium. For the chest simulation, the image coverage was defined from the lung apex to the top of the adrenal glands. Finally, 3D dose distributions were calculated, by simulating the interactions and dose depositions of a large number of photons ($> 10^9$) in the voxel model.

Organ and blood dose calculation

Individual organs were delineated manually on the original PET/CT images by a medical physicist and validated by an expert. These regions of interest (ROIs) were then used to determine mean organ doses on the output images of the simulation software. All other tissue was classified as remainder and its dose was scaled according to the patient's total body weight.

Blood dose was calculated according to ICRP 89 as the weighted sum of the simulated individual doses to the delineated organs (+ remainder) listed in Table 3 [19]. A second, simplified calculation was performed by including only heart, lungs and liver (+ remainder), as they are the three largest blood-containing organs in the human body [19].

$$D_{blood} = \sum_{i=1}^n w_i * D_i$$

Where $n=11$ (10 organs + remainder) or $n=4$ (3 organs + remainder). The blood content, w_i , in percentage of total blood volume for each organ i is listed in Table 3 [19]. In this way, three models for blood dose calculation were used in this study: (1) the full-body voxel model with 10 delineated organs (B); (2) the thoracic/abdominopelvic region of the full-body voxel model with 10 delineated organs (T/A) and (3) the thoracic/abdominopelvic region of the full-body voxel model with three delineated organs (T_{simpl}/A_{simpl}). A non-parametric Kruskal-Wallis test was used to compare the different models.

Table 2 Summary of exposure parameters for abdominopelvic and chest CT simulations

Parameter	abdominopelvic			chest		
	80	100	120	80	100	120
peak kilovoltage (kVp)	80	100	120	80	100	120
tube current (mA)	TCM			TCM		
rotation time (ms)	330			330		
pitch	0.9			0.9		
beam collimation (mm)	38.4			38.4		
scan FOV (mm)	500			500		
scan start	liver top			lung apex		
scan end	ischium			adrenal glands top		

TCM tube current modulation

Table 3 Blood content in percentage of total blood volume [19]

organ	blood content (%)
heart	10.00
liver	10.00
lungs	12.50
remainder	67.50
urinary bladder	0.02
colon	2.20
stomach	1.00
thyroid	0.06
gonads	0.04 ^a
kidneys	2.00
spleen	1.40
remainder	60.78 ^a

^aData are given for males. For females, blood content of gonads and remainder is respectively 0.02 % and 60.80 %

LAR

In addition to the organs used for the blood dose calculation, bone structures were delineated and bone marrow dose was calculated, taking into account the bone marrow

distribution as a function of age in humans [23]. Differences in photon absorption between bone and bone marrow were corrected by means of the mass absorption coefficient ratio of soft tissue and bone [24]. Furthermore, breasts were defined in the female voxel models. Next, individual overall LAR of cancer incidence and mortality was estimated, according to the BEIR VII risk models [25]. Gender- and age-dependent incidence and mortality rates within the Euro-American population were taken into account. The estimates are obtained as combined estimates based on relative risk and absolute risk transport and have been adjusted by a dose and dose rate effectiveness factor (DDREF) of 1.5, except for leukaemia, which is based on a linear-quadratic model. To determine intermediate age points, quadratic fits were applied. Doses and LAR were multiplied for each organ and summed to obtain overall LAR.

SSDE

Based on the AAPM Report No. 204 [7], the size-specific dose estimate was calculated at each position z along the longitudinal scan direction. Recently, a new size metric was proposed by the AAPM taking into account the X-ray attenuation of the patient: the water equivalent diameter (D_w) [8]. The $SSDE(z)$ is calculated as:

$$SSDE(z) = a * e^{-bD_w} * CTDI_{vol}(z)$$

Where a and b are exponential fit coefficients, depending on the diameter of the PMMA phantom (either 16 or 32 cm) used to measure the $CTDI_{vol}$ [7]. The mean SSDE over the entire scan range is then determined as:

$$\overline{SSDE} = \frac{\sum_{z=1}^N SSDE(z)}{N}$$

Where N is the total number of images.

RESULTS

Fig. 2 displays estimated organ doses as a function of SSDE, based on $CTDI_{vol,16}$ ($SSDE_{16}$). Thoracic and abdominopelvic simulations are shown separately and were performed with the full-body voxel model at three different kVp's. Thyroid dose was negligible for abdominopelvic simulations, as well was colon, bladder, and gonad dose for chest

simulations. Correlations were very high ($r>0.9$, $p<.001$) for organs in the FOV: heart and lung for thorax; liver, stomach, spleen, kidney, colon, and bladder for abdomen. Lower correlations were found for organs partially irradiated with the abdominopelvic or chest simulations ($r>0.8$, $p<.001$).

No significant differences in blood dose calculations were found between the full-body model, the thoracic model and the simplified thoracic model ($p=.78$). Similar conclusions were obtained for the abdominopelvic simulations ($p=.46$).

Blood dose calculations for the simulated chest and abdominopelvic CT examinations are presented as a function of the patient's SSDE in Fig. 3. Each graph includes chest and abdominopelvic CT simulations for all 10 patients (male and female) with the full-body voxel model. The patient's blood dose shows a strong linear relationship with the patient's $SSDE_{16}$ ($r>0.9$, $p<.001$). Similar conclusions were found, based on the 32 cm phantom ($SSDE_{32}$).

Overall LAR of cancer incidence and mortality of the simulated chest and abdominopelvic CT examinations are presented as a function of $SSDE_{16}$ in Figs. 4 and 5. The results are shown separately for males and females. Each graph includes chest or abdominopelvic CT simulations with the full body voxel model. LAR shows a strong linear relationship with the patient's $SSDE_{16}$ ($r>0.9$, $p<.001$). Similar results were found, based on $SSDE_{32}$ and summarized in Table 4.

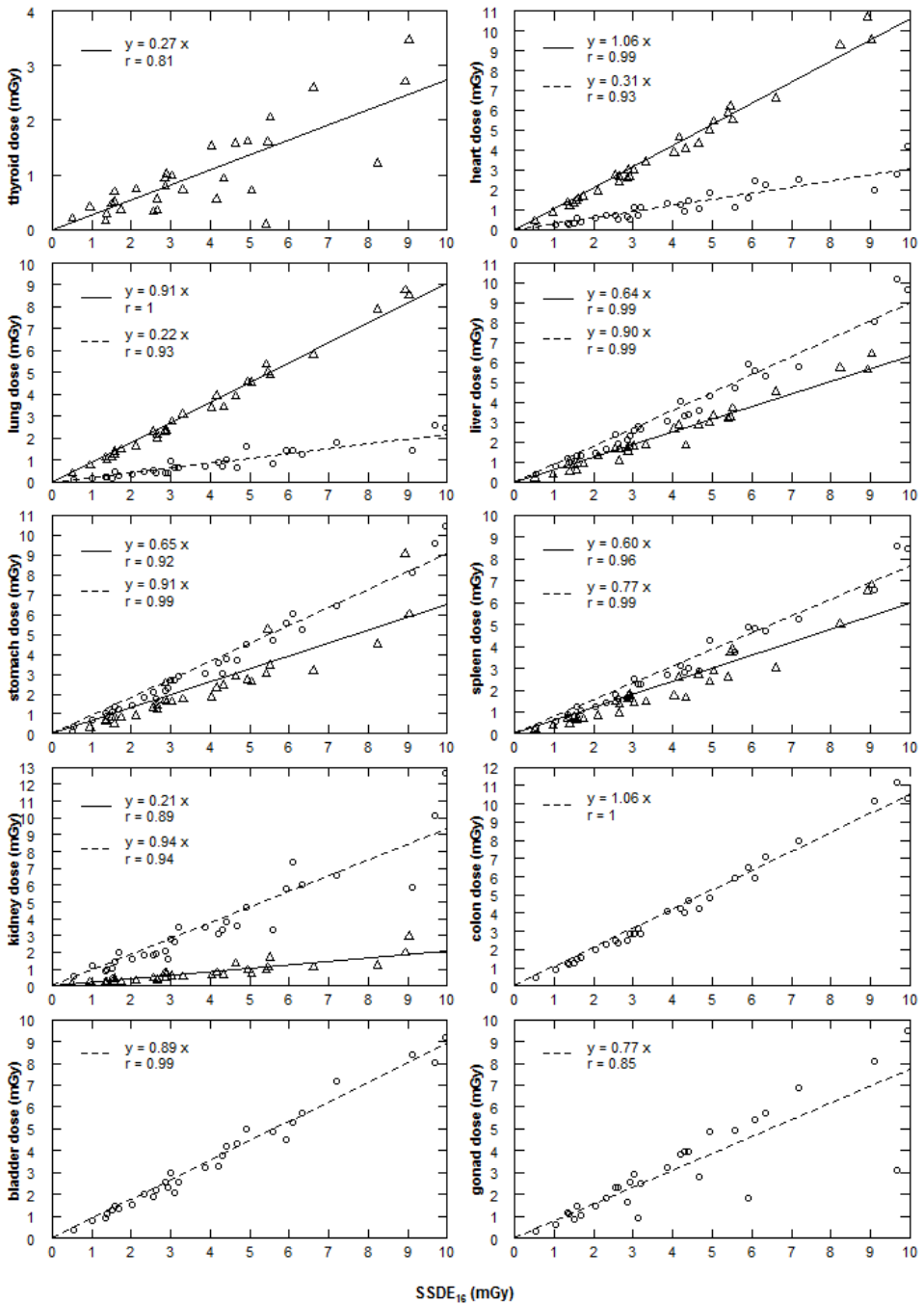


Fig. 2 Estimated organ doses as a function of size-specific dose estimate, based on CTDI_{vol,16} (SSDE₁₆). Organ doses are calculated with the full-body voxel model. Plot points are patient-specific organ doses for chest (*triangles*) and abdominopelvic (*circles*) simulations at 80, 100 and 120 kVp. Lines are linear fits $D_{\text{organ}} = a \cdot \text{SSDE}_{16}$ to the data. r =Pearson sample correlation coefficient ($p < .001$)

DISCUSSION

Our goal was to define a method to estimate patient-specific organ and blood doses and cancer risks from paediatric chest and abdominopelvic CT examinations. It must be emphasized that the purpose of this study was not to calculate doses and risks from the 10 selected subjects, but to develop an easy-to use and clinically applicable method for dose and LAR estimation. Head and neck CTs are more common in the paediatric population than examinations of the torso. Nevertheless, because SSDE was not developed for head scans [7], our research is based on thoracic and abdominopelvic simulations. This study focuses on children, since dose reduction in paediatric radiology is a top priority [5,12,26,27].

Care must be taken when making conclusions about risk estimates. Physical quantities, in particular absorbed organ dose, are well-defined and can be estimated accurately. However, risk is a derived attribute, which is not measurable. Therefore, significant uncertainties might be associated with lifetime attributable risk models. Our study is based on the report of BEIR VII, yet other risk models exist [6,28]. The uncertainties involved in the risk estimations presented by Figs. 4 and 5 are related to the lack of information on the dose response in the low-dose range on the one hand and to the uncertainties on the BEIR VII estimations on the other hand. Despite the uncertainties on the LAR values of Figs. 4 and 5, we included BEIR VII risk estimations as they provide the best possible age/gender-specific risk estimation available at the moment. However, the BEIR VII committee estimates that the excess cancer mortality due to radiation can be estimated within a factor of two (at 95% confidence level) [25]. In order to determine the variation in LAR, depending on the patient's age, we calculated LAR of cancer mortality of the 11-year-old, assuming the patient to be 5 years younger/older (Table 5). The maximum difference in LAR, relative to the calculations with the real age of the patient, was 22 %. These variations lie within the uncertainties of the BEIR VII report.

Several dose calculation tools exist to estimate organ doses, e.g. ImPact (www.impactscan.org), ImpactDose (CT Imaging GmbH, Erlangen, Germany) and CT-Expo (Medizinische Hochschule, Hannover, Germany). However, since these calculations are based on pre-tabulated results from Monte Carlo simulations, the selectable anthropomorphic phantoms are limited to newborn, child (1, 5, 10 and 15 years), adult male and adult female. Considering the diversity among the anatomy of paediatric patients, it is impossible to represent the whole population with only a few phantom models. With predefined anthropomorphic phantoms, organ size and location in the body is not in accordance with the anatomy of the patient. In addition, there may be disagreement in patient positioning and uncertainty in the start and end position of the scan region. Moreover, the existing dose calculation tools do not compute the dose to the

bone because the latter is not used to calculate effective dose, according to the ICRP103 [29]. Therefore, calculating the remainder, as it is used in the blood dose calculation, continues to be an issue with these software tools. These drawbacks may be addressed only with models that are specific for each individual patient [30]. To resolve this, the patient's clinical CT data can be used as a voxelized phantom model [20,30,31]. A drawback might be that there is no information available outside the patient's scan range. Consequently, the model will consist of incomplete organs at the periphery of the volume. In addition, no scatter can occur outside the model. To overcome this, we used clinical CT data from patients who underwent a whole body PET/CT examination, to estimate the contribution from scattered photons.

The method of SSDE, described by the AAPM task group, estimates the average dose to the patient, in the centre of the scanned region (along the z-axis). It does not allow the estimation of individual organ doses [7]. The data in Fig. 2 emphasize this by means of the slope of the different linear fits. For organs in the beam of an abdominopelvic scan, SSDE overestimates organ dose on average with 11 %. Overall, a strong to very strong linear correlation was found between SSDE and individual organ doses. Correlations were stronger for in-beam organs ($r > 0.9$) than for organs on the periphery or outside the scan range ($r > 0.8$). The superficial location, small size, and the fact that the organ was outside the FOV of the chest simulation, explains the weaker correlation for thyroid dose in comparison with other organs. Nevertheless, conclusions about organ doses can be made on the basis of SSDE, by taking into account a linear correction factor.

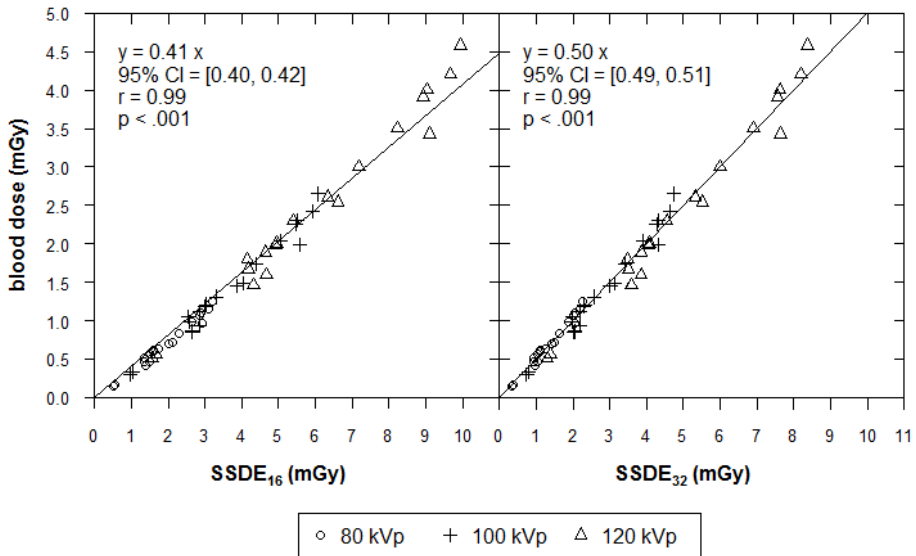


Fig. 3 Estimated blood dose (D_{blood}) as a function of size-specific dose estimate (SSDE), based on $\text{CTDI}_{\text{vol},16}$ and $\text{CTDI}_{\text{vol},32}$. Blood dose is calculated with the full-body voxel model. Plot points are patient-specific blood doses for chest and abdomen simulations at 80, 100 and 120 kVp. Lines are linear fits $D_{\text{blood}} = a \cdot \text{SSDE}$ to the data. r = Pearson sample correlation coefficient

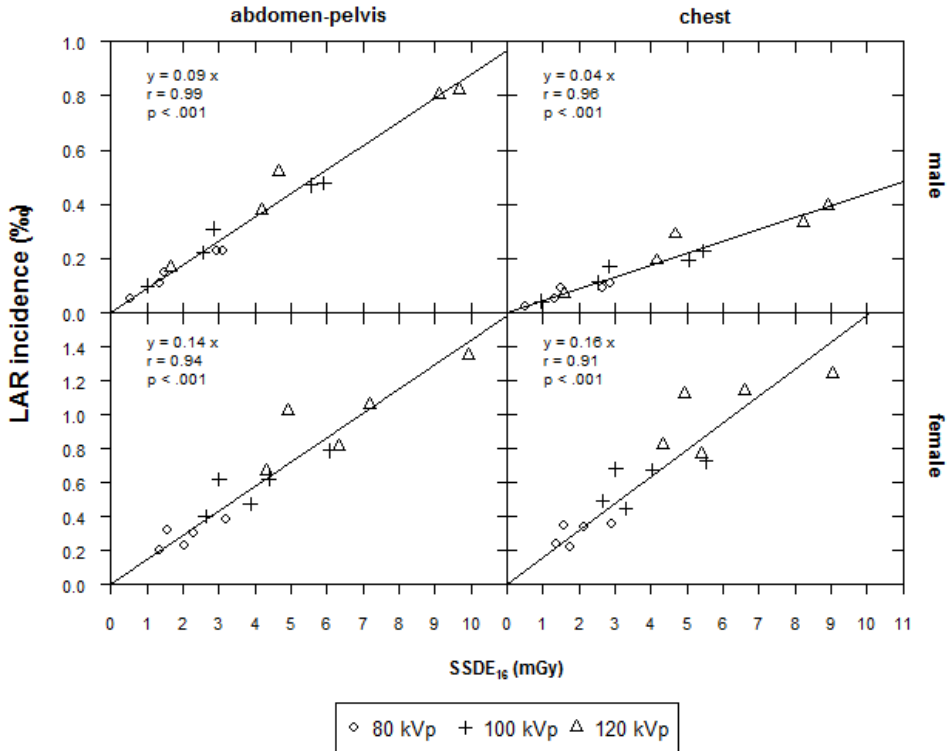


Fig. 4 Overall LAR of cancer incidence, according to the BEIR VII model as a function of size-specific dose estimate, based on $CTDI_{vol,16}$ ($SSDE_{16}$). LAR is calculated with the full-body voxel model. Plot points are LAR of cancer incidence for abdominopelvic (a and c) and chest (b and d) simulations at 80, 100 and 120 kVp. Results are shown separately for males (a and b) and females (c and d). Lines are linear fits $LAR_{incidence} = a * SSDE$ to the data. r = Pearson sample correlation coefficient

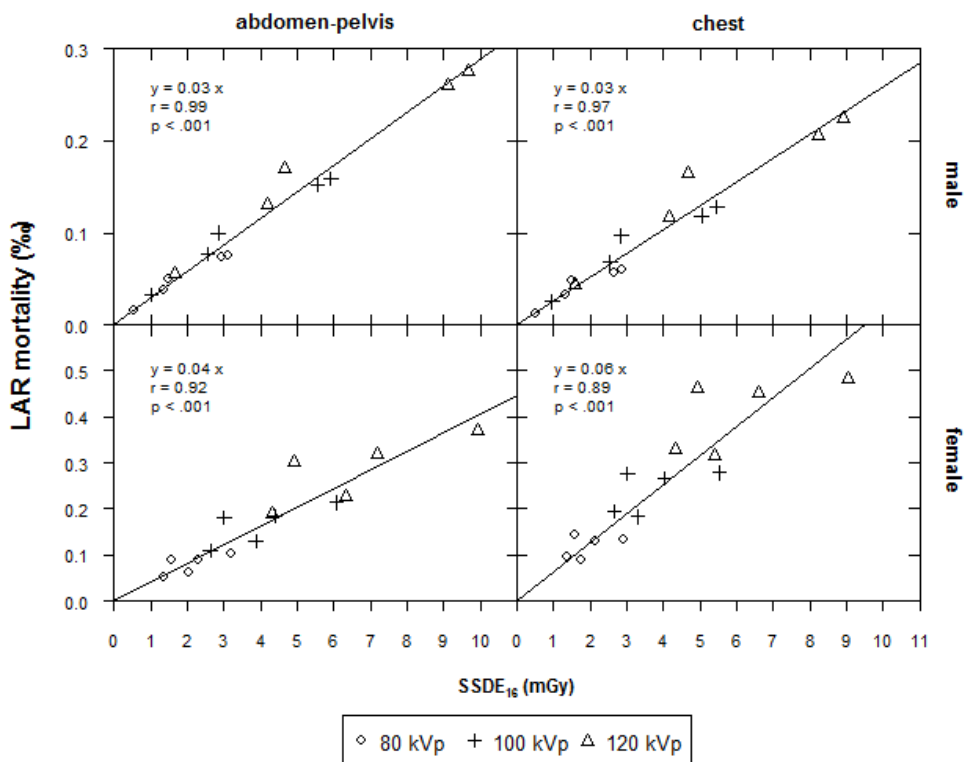


Fig. 5 Overall LAR of cancer mortality, according to the BEIR VII model as a function of size-specific dose estimate, based on CTDI_{vol,16} (SSDE₁₆). LAR is calculated with the full-body voxel model. Plot points are LAR of cancer mortality for abdominopelvic (a and c) and chest (b and d) simulations at 80, 100 and 120 kVp. Results are shown separately for males (a and b) and females (c and d). Lines are linear fits $LAR_{mortality} = a \cdot SSDE$ to the data. r = Pearson sample correlation coefficient

Table 4 Results of linear regression analysis describing overall LAR (%) as a function of SSDE (mGy) for abdominopelvic and chest simulations. r = Pearson sample correlation coefficient ($p < .001$)

	LAR incidence				LAR mortality			
	SSDE ₁₆	r	SSDE ₃₂	r	SSDE ₁₆	r	SSDE ₃₂	r
abdominopelvic								
male	0.09	0.99	0.11	0.99	0.03	0.99	0.04	0.99
female	0.14	0.94	0.18	0.95	0.04	0.92	0.05	0.93
chest								
male	0.04	0.96	0.05	0.97	0.03	0.97	0.03	0.98
female	0.16	0.91	0.20	0.92	0.06	0.89	0.08	0.90

Using the full-body voxel model, we have all the anatomical information of the patient at our disposal, allowing the simulated photons to scatter outside the irradiated volume as well. In addition, all organs of interest are integral available to calculate mean organ doses in the most accurate way. For applications in daily routine, we only receive DICOM images of the patient's scanned region (A/T). Therefore, dose calculations might be less precise. Since delineating all 10 organs is time-consuming, we created two simplified models including only the three largest blood containing organs (heart, liver and lungs) in combination with the remainder ($A_{\text{simpl}}/T_{\text{simpl}}$). In this study, organs on the periphery of the thorax and abdominopelvic voxel models were considered to be complete. Additionally, organs outside these models were assumed to receive a dose of 0 mGy. The remainder, on the contrary, was adjusted according to the patient's weight, available in his clinical record. The weight of the simulation model was calculated by multiplying its volume with its mass density (1.050 g/cm^3) [32]. An accurate estimate of the remainder is crucial, since it is the dominant organ in the blood dose calculation (Table 3). This study shows that accurate blood dose calculations can be made based on Monte Carlo simulations using the patient's clinical CT data. Differences between the A/T and the full-body voxel model (B) were not significant: the impact of the incomplete organs at the periphery of the volume, as well as the scatter contribution outside the voxel model is low. Therefore, no need exists in extending the volume with scalable phantoms to complete the patient's anatomy. What is more, the blood dose can be estimated using only lung, liver, and heart doses. To avoid the laborious task of organ segmentation and to minimize calculation time, we developed a clinically applicable method to determine organ and blood dose and total cancer risk. Our study showed an excellent correlation between SSDE on the one hand and organ and blood dose and overall LAR on the other hand. In this way, organ and blood doses and LAR of total cancer incidence and mortality can be estimated using only CTDI_{vol} and the patient's diameter.

CTDI_{vol} is commonly used as a dose indicator for CT examinations. As stated by the IEC standard [33], this parameter is measured in a cylindrical PMMA phantom with diameter of 16 cm (head protocols) or 32 cm (body protocols). However, for paediatric patients, the 16 cm phantom is often used for body protocols. For this reason, we included both CTDI_{16} and CTDI_{32} in our clinically applicable method.

This study focuses on CT examinations with TCM; however, this method can also be applied to scans with fixed mA. In this way, there is no need to extract the CTDI_{vol} /slice from the DICOM headers of the CT images. Care must be taken when extending our method to the adult population. Using tube current modulation (TCM), the mA variation is rather small in children, compared to adult CT examinations. In the study of Khatonabadi et al, better correlations were found between organ doses and patient sizes, when using organ-specific CTDI_{vol} values instead of a global CTDI_{vol} [34].

To our knowledge, no studies exist demonstrating a correlation between the patient's SSDE and blood dose or total cancer risk, resulting from a CT examination. Turner et al

performed Monte Carlo simulations on eight different voxel-based models, including two paediatric models [35]. The authors state that doses of fully irradiated abdominal organs can be estimated using only the knowledge of the $CTDI_{vol}$ and the patient's perimeter. However, partially irradiated organs didn't show any correlation with the size of the patient. The work focuses on the abdomen in which the perimeter does not typically fluctuate much over the scan region. Moore et al used anthropomorphic phantoms to investigate the correlation of SSDE with absorbed organ dose in chest and abdominopelvic CT examinations [36]. For in-beam organs, the average organ dose normalized by SSDE was within 10 % of unity. This is comparable with our results (Fig. 2).

Table 5 LAR of cancer mortality of an 11-year old boy, for abdominopelvic and chest simulations. In addition, results are shown, assuming the patient to be 5 years younger/older

	abdomen-pelvis			chest		
	80 kVp	100 kVp	120 kVp	80 kVp	100 kVp	120 kVp
6 years	0.045	0.093	0.158	0.040	0.083	0.143
11 years	0.037	0.077	0.131	0.033	0.068	0.117
16 years	0.032	0.065	0.111	0.028	0.057	0.098
max diff	21 %	21 %	21 %	22 %	22 %	22 %

One of the limitations of this study was that the patient's clinical data only included images from the head to the mid-thigh. Furthermore, since exams with the arms next to the body may change the dose profile and cause artefacts, the patients were positioned with the arms above the head. Consequently, there was no anatomical information available about the limbs of the examined children. However, arms and legs hold no organs at risk [37]. Moreover, as mentioned earlier, the remainder dose was appropriately scaled taking into account the weight of the patient. The abdominopelvic simulation ended on average 1.5 times the table feed (5.4 cm) before the end of the full-body voxel models. In this way, enough scatter volume remains for secondary photons to scatter outside the scan region. Although gaps up to 6 years occur in the male and female gender groups, we carefully selected patients in different height and weight categories, providing continuity in BMI.

Monte Carlo methods are the gold standard for patient-specific dose calculations. Therefore, if the specific hard and software environment is available to the user, Monte Carlo simulations should be used to estimate the patient's organ doses. Our study shows that, by using only the patient's clinical CT data, accurate blood dose estimations can still be accomplished. However, the SSDE method makes an on-the-spot dose and LAR

estimation possible in routine clinical practice. The quantities can be added to the dose report of the patient, which makes it possible to implement them in a dose monitoring system.

Acknowledgments This study has received funding by the Agency for Innovation by Science and Technology (IWT). The scientific guarantor of this publication is Prof. Klaus Bacher. The authors of this manuscript declare no relationships with any companies, whose products or services may be related to the subject matter of the article. No complex statistical methods were necessary for this paper. Institutional Review Board approval was obtained. Written informed consent was waived by the Institutional Review Board. Methodology: performed at one institution.

REFERENCES

- 1 UNSCEAR (2008) Sources and effects of ionizing radiation. Report to the General Assembly of the United Nations. United Nations, New York
- 2 NCRP (2009) Ionizing Radiation Exposure of the Population of the United States. NCRP Report 160, Bethesda MD
- 3 HSE (2009) Population Dose from CT Scanning, Ireland
- 4 PHE (2010) Frequency and Collective Dose for Medical and Dental X-ray Examinations in the UK (HPA-CRCE-012), United Kingdom
- 5 Brenner D, Hall E (2007) Current concepts - Computed tomography - An increasing source of radiation exposure. *N Engl J Med* 357:2277-2284
- 6 UNSCEAR (2013) Sources and effects of ionizing radiation. Report to the General Assembly of the United Nations. United Nations, New York
- 7 AAPM (2011) Size-specific dose estimates (SSDE) in pediatric and adult body ct examinations (Task Group 204).
- 8 AAPM (2014) Use of Water Equivalent Diameter for Calculating Patient Size and Size-Specific Dose Estimate (SSDE) in CT (Task Group 220).
- 9 Li X, Samei E, Segars WP et al (2011) Patient-specific radiation dose and cancer risk estimation in CT: Part II. Application to patients. *Med Phys* 38:408-419
- 10 Petoussi-Hens N, Zankl M, Fill U, Regulla D (2002) The GSF family of voxel phantoms. *Phys Med Biol* 47:89-106
- 11 Brady Z, Cain TM, Johnston PN (2012) Comparison of organ dosimetry methods and effective dose calculation methods for paediatric CT. *Australas Phys Eng Sci Med* 35:117-134
- 12 Thierry-Chef I, Dabin J, Friberg EG et al (2013) Assessing Organ Doses from Paediatric CT Scans-A Novel Approach for an Epidemiology Study (the EPI-CT Study). *Int J Environ Res Public Health* 10:717-728

- 13 Li X, Samei E, Segars WP et al (2011) Patient-specific radiation dose and cancer risk estimation in CT: Part I. Development and validation of a Monte Carlo program. *Med Phys* 38:397-407
- 14 Lobrich M, Rief N, Kuhne M et al (2005) In vivo formation and repair of DNA double-strand breaks after computed tomography examinations. *Proc Natl Acad Sci U S A* 102:8984-8989
- 15 Beels L, Bacher K, Smeets P, Verstraete K, Vral A, Thierens H (2012) Dose-length product of scanners correlates with DNA damage in patients undergoing contrast CT. *Eur J Radiol* 81:1495-1499
- 16 Halm BM, Franke AA, Lai JF et al (2014) γ -H2AX foci are increased in lymphocytes in vivo in young children 1 h after very low-dose X-irradiation: a pilot study. *Pediatr Radiol* 44:1310-1317
- 17 Rothkamm K, Balroop S, Shekhdar J, Fernie P, Goh V (2007) Leukocyte DNA damage after multi-detector row CT: A quantitative biomarker of low-level radiation exposure. *Radiology* 242:244-251
- 18 Vandevoorde C, Franck C, Bacher K et al (2014) gamma-H2AX foci as in vivo effect biomarker in children emphasize the importance to minimize x-ray doses in paediatric CT imaging. *Eur Radiol*. 10.1007/s00330-014-3463-8
- 19 ICRP (2002) Basic anatomical and physiological data for use in radiological protection: reference values. A report of age- and gender-related differences in the anatomical and physiological characteristics of reference individuals. ICRP Publication 89. *Ann ICRP* 32:5-265
- 20 Chen W, Kolditz D, Beister M, Bohle R, Kalender WA (2012) Fast on-site Monte Carlo tool for dose calculations in CT applications. *Med Phys* 39:2985-2996
- 21 Deak P, van Straten M, Shrimpton PC, Zankl M, Kalender WA (2008) Validation of a Monte Carlo tool for patient-specific dose simulations in multi-slice computed tomography. *Eur Radiol* 18:759-772
- 22 Schmidt B, Kalender WA (2002) A fast voxel-based Monte Carlo method for scanner- and patient-specific dose calculations in computed tomography. *Phys Med* 18:43-53
- 23 Cristy M (1981) Active bone marrow distribution as a function of age in humans. *Phys Med Biol* 26:389-400
- 24 Seuntjens J, Thierens H, Van der Plaetsen A, Segaert O (1987) Conversion factor f for X-ray beam qualities, specified by peak tube potential and HVL value. *Phys Med Biol* 32:595-603
- 25 Council N (2006) Health risks from exposure to low levels of ionizing radiation: BEIR VII phase 2. The National Academies Press
- 26 Brenner DJ (2010) Slowing the Increase in the Population Dose Resulting from CT Scans. *Radiat Res* 174:809-815
- 27 Kropil P, Bigdeli AH, Nagel HD, Antoch G, Cohnen M (2014) Impact of increasing levels of advanced iterative reconstruction on image quality in low-dose cardiac CT angiography. *Rof* 186:567-575
- 28 EPA (2011) EPA Radiogenic Cancer Risk Models and Projections for the U.S. Population. U.S. Environmental Protection Agency, Washington DC
- 29 ICRP (2000) Managing Patient Dose in Computed Tomography. ICRP publication 87. *Ann ICRP* 30

- 30 Tian X, Li X, Segars W, Paulson E, Frush D, Samei E (2014) Pediatric Chest and Abdominopelvic CT: Organ Dose Estimation Based on 42 Patient Models. *Radiology* 270:535-547
- 31 Li X, Samei E, Segars WP, Sturgeon GM, Colsher JG, Frush DP (2011) Patient-specific Radiation Dose and Cancer Risk for Pediatric Chest CT. *Radiology* 259:862-874
- 32 ICRP (2009) Adult Reference Computational Phantoms. ICRP Publication 110. *Ann ICRP* 39:1-166
- 33 (2012) IEC 60601-2-44-am1 ed3.0 Medical electrical equipment - Part2-44: Particular requirements for the basic safety and essential performance of X-ray equipment for computed tomography
- 34 Khatonabadi M, Kim HJ, Lu P et al (2013) The feasibility of a regional CTDivol to estimate organ dose from tube current modulated CT exams. *Med Phys* 40:051903
- 35 Turner AC, Zhang D, Khatonabadi M et al (2011) The feasibility of patient size-corrected, scanner-independent organ dose estimates for abdominal CT exams. *Med Phys* 38:820-829
- 36 Moore BM, Brady SL, Mirro AE, Kaufman RA (2014) Size-specific dose estimate (SSDE) provides a simple method to calculate organ dose for pediatric CT examinations. *Med Phys* 41
- 37 (2002) Basic anatomical and physiological data for use in radiological protection: reference values. A report of age- and gender-related differences in the anatomical and physiological characteristics of reference individuals. ICRP Publication 89. *Ann ICRP* 32:5-265

Part III

General discussion

Chapter 10

Tube current modulation

In Chapter 6 of this PhD dissertation, we examined the behaviour of automatic tube-current modulation (ATCM). The effect of the localizer acquisition and the direction of the scan was critically assessed. The paper emphasizes a strong need for ATCM performance evaluation to assure optimal dose reduction for the patient. Both the SPR and CT scan direction have an important influence on the dose-reducing efficacy of ATCM. In addition to this work, our research group investigated the effect of the table position on the automatic exposure control of Siemens (CareDose4D) [1]. Miscentering the patient causes an incorrect functioning of the modulation technique. A higher table position will lead to a smaller shadow on the posterior-anterior localizer, as the patient is farther away from the X-ray tube (Figure 10.1, a). Consequently, lower exposures will be selected and the image quality will deteriorate. If the patient is too close to the tube (Figure 10.1, c), the image is magnified and the resulting tube current values will be too high.

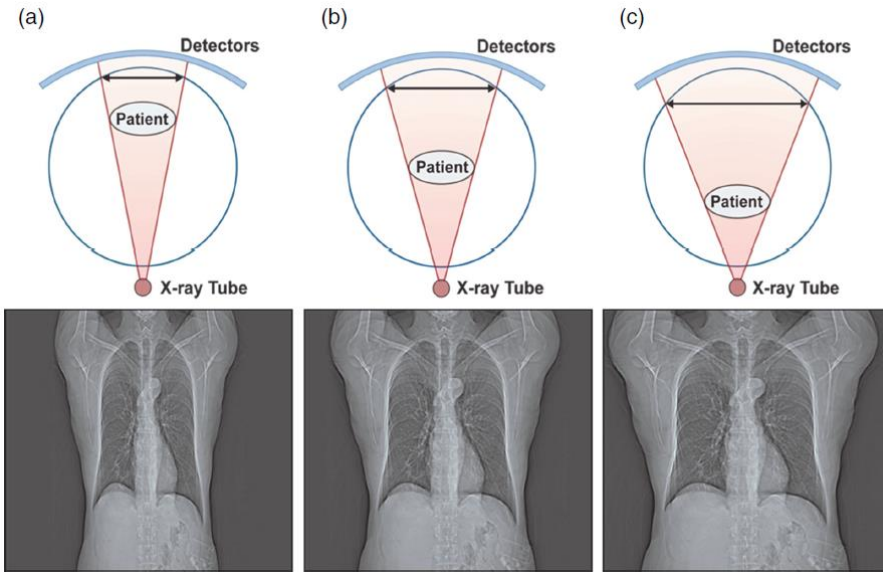


Figure 10.1 PA localizer image at different table heights. Miscentering the patient causes an incorrect functioning of the tube-current modulation technique [2].

The selected mAs values, based on a PA localizer with varying table heights from 80 cm to 100 cm are shown in Figure 10.2. The Alderson RANDO phantom was positioned in the isocenter of the scanner if the table height was 90 cm. Because the effective mAs was limited to 250, both 80cm- en 85cm-curves reach the same maximum exposure. Similar conclusions were found, based on AP localizers. Although this behaviour could be predicted, the differences in dose are much higher than initially expected. Tube current values increase by a factor of 2 between the highest and lowest table position. When the same scans were based on a lateral (LAT) localizer, no significant differences were found between the selected exposure values. After all, no magnifications occur in lateral projections if the table height is changed. Because patients are easier to centre on the table in the left-right direction than in the anterior-posterior direction, a LAT localizer is less susceptible to mis-centering errors. These results confirm the findings of Paper 1 of this PhD, stating a lateral (or dual) SPR is the best choice for Siemens scanners.

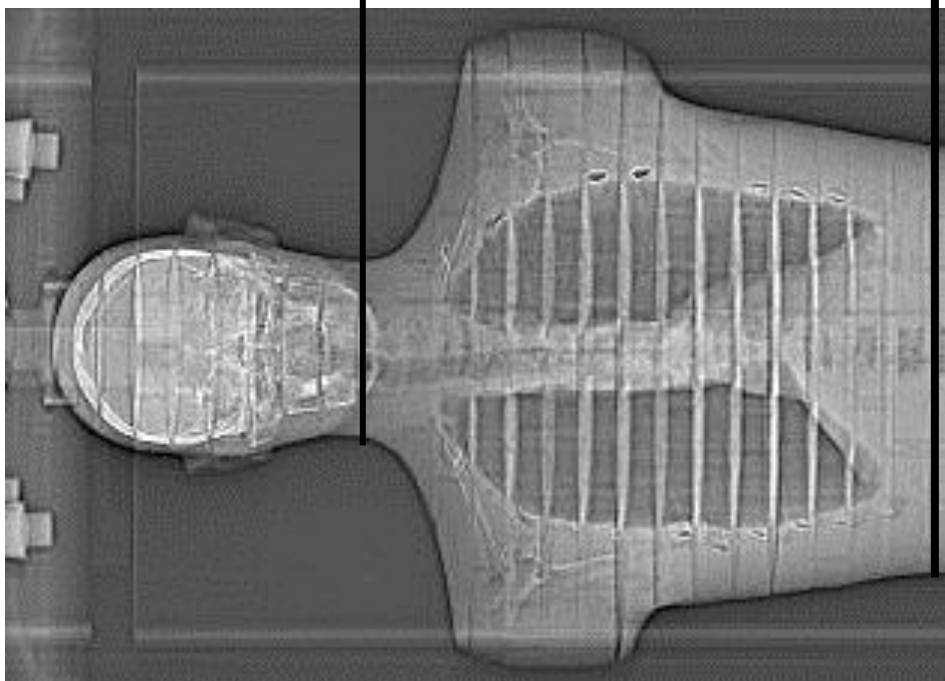
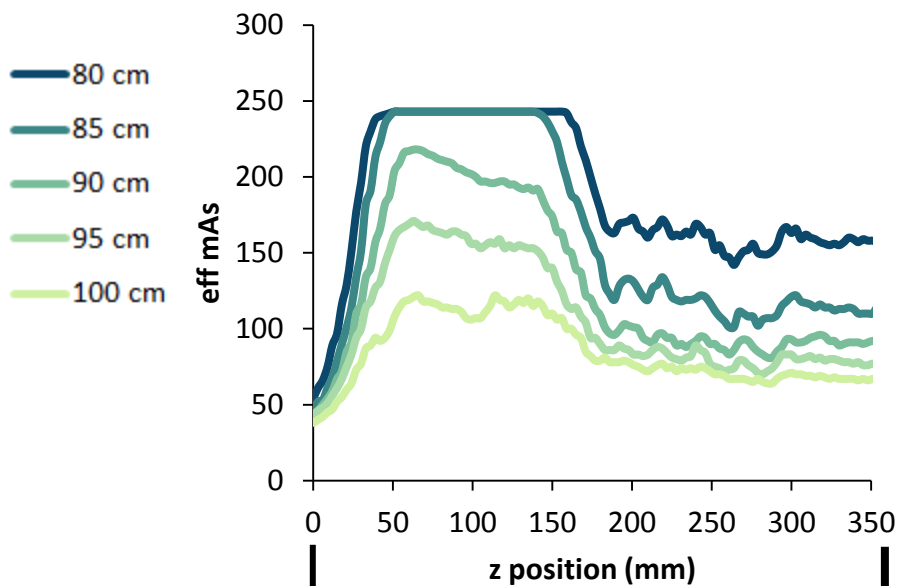


Figure 10.2 Effective mAs values as a function of slice position along the z-axis of the scanner. Chest scans of the anthropomorphic RANDO phantom were made, based on a PA localizer image, with varying table heights from 80 cm (close to the tube) to 100 cm (farther away from the tube) [1].

With ATCM, the tube current will be automatically modulated to compensate for variations in patient attenuation. Different vendors use different methods to define a desired image quality. With GE, Smart mA tries to maintain a constant noise level (specified by the Noise Index) at all z locations [3]. Siemens, on the other hand, uses a Quality Reference mAs (QRM) to prescribe image quality [4]. The main difference is that CareDose4D tries to maintain a constant level of overall diagnostic quality, instead of a noise parameter. Consequently, with a Siemens device, ATCM will not lead to a constant noise level. For smaller attenuation levels, lower noise is required in order to have the same diagnostic value since smaller patients have finer anatomical structures and lower inherent contrast. For larger attenuation levels, higher noise is accepted, since larger patients usually have larger anatomical structures and higher inherent contrast.

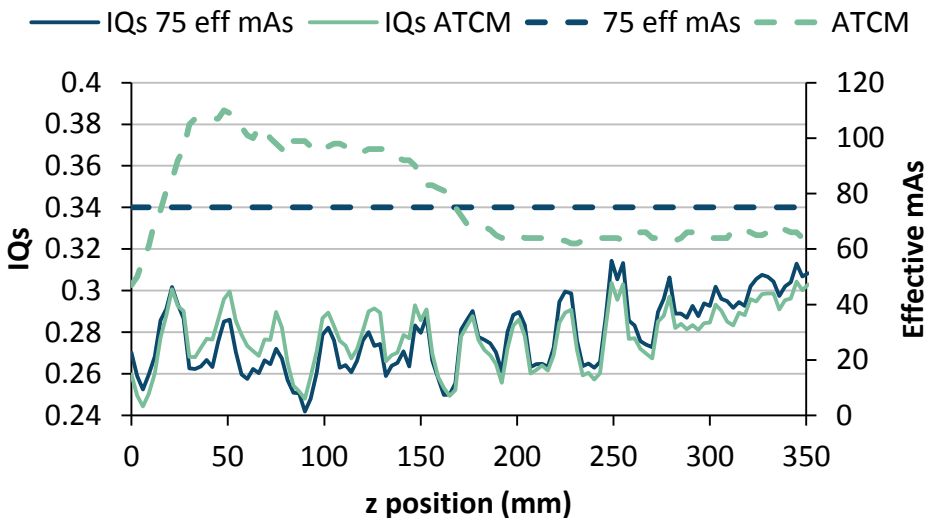


Figure 10.3 IQs and effective mAs values as a function of slice position along the z-axis of the scanner. Chest scans of an anthropomorphic RANDO phantom were made with ATCM and with a fixed exposure value of 75 mAs_{eff} [5].

Our research group studied the behaviour of CareDose4D in more detail with the use of a RANDO phantom [5]. Chest scans were made with ATCM and with a fixed exposure value of 75 mAs_{eff} . For both scans, the Image Quality scores (IQs, see Chapter 4) were calculated and plotted against the slice locations along the length of the scan. The results are presented in Figure 10.3. It is noticed that the IQs values for ATCM (green) are higher, with respect to the IQs values at fixed tube-current (blue), whenever the exposures are higher

than $75 \text{ mAs}_{\text{eff}}$. Along the length of the thorax scan, two breakpoints are observed where both exposure curves intersect. These landmarks correspond to the start and end of the shoulders, as can be seen in Figure 10.2. This means that the required diagnostic quality could not be reached with a fixed exposure of $75 \text{ mAs}_{\text{eff}}$. Instead, higher tube-current values had to be selected.

A similar trend can be seen in both IQs-curves, suggesting that our results confirm the absence of a constant image noise level. However, variations are smaller with ATCM (20%), compared to a scan at fixed exposure (23%).

The exposure parameters along the length of the patient are stored in the DICOM information of the acquired CT data. By extracting these values, the z-axis TCM can be visualized as shown in Figure 10.2. In addition, the tube current varies while rotating around the patient, to account for differences in attenuation depending on the projection angle. A more realistic representation of the tube current modulation is given in Figure 10.4. In this way, the exposure value reported in the DICOM data of a particular image represent the average exposure of all projections needed to reconstruct this slice. The specific distribution of tube current values in the axial plane is lost. This information is however crucial to correctly simulate the acquired CT scan in a Monte Carlo software.

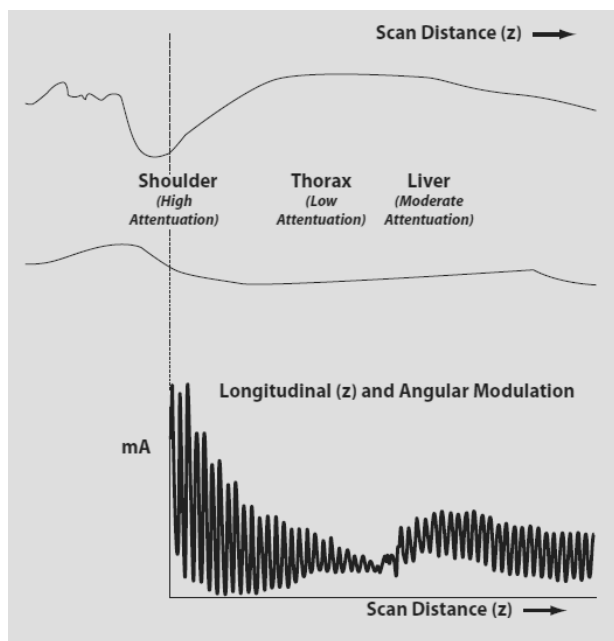


Figure 10.4 Longitudinal and angular tube current modulation [3].

In paper 3 of this PhD dissertation, CT datasets were collected with a slice thickness of 3mm and a table feed of 34.56mm. As a result, approximately 11 exposure values were extracted for each rotation. The performed Monte Carlo calculations for patient-specific organ dose assessment were simulated with 34 projections per rotation. Consequently, the same exposure parameters were applied to every 3 successive projection angles. It is possible to determine the tube current settings for each projection of the CT acquisition by accessing the raw data of the scan. However, since paper 3 was a retrospective study, this information was no longer available. Nevertheless, relying on personal communication with Siemens, acquiring the raw projection data of a CT examination is not possible as it contains confidential information.

To evaluate the clinical performance of ATCM systems, access to the raw data must be provided by the manufacturer. It holds crucial information about in-plane tube current values needed for an accurate calculation of the organ doses and radiation induced risks to the patient.

Unlike in conventional TCM, information about organ-based modulation is provided by the manufacturer (Siemens Healthcare, Germany). According to Figure 10.5, X-CARE reduces the tube current to 25% of the mean value, within a range of 80°. Posteriorly, the exposure is increased to 125% to compensate for the reduced photon flux to the detector. A linear transition zone of 20° is present on either side of the patient, so that 100% of the mean value is reached at 55°. Because the raw data of the acquired CT datasets was no longer available, it was not possible to verify this angular distribution. We relied on the manufacturer's information to perform the organ-based TCM (OBTCM) simulations in Paper 3.

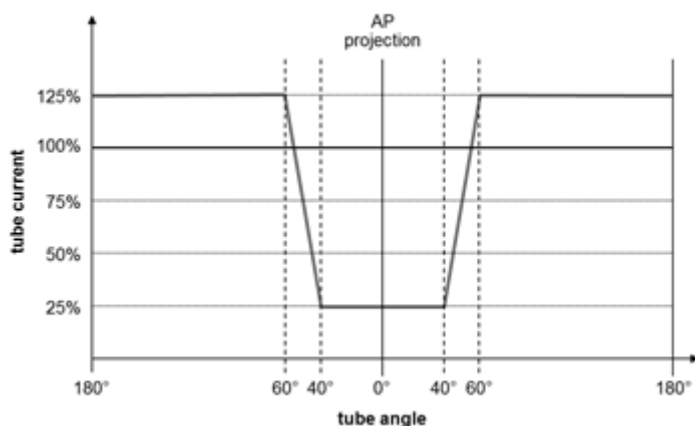


Figure 10.5 Schematic overview of the angular tube current modulation used by X-CARE [6].

Paper 3 of this PhD work concluded that the potential benefit of OBTCM to the female breast is overestimated as the reduced tube current zone of 40° on either side of the patient is too limited. Our results show that the breasts are more laterally located. On average this radiosensitive organ extends to 83° on both sides. Consequently, part of the glandular tissue will be situated in the increased tube current zone. A simple solution exists in wearing a brassiere. The amount of breast tissue within the reduced dose zone hereby increases to 83-97%, depending on the cup size of the patient [7].

As, for large cup sizes, still 17% of the breasts is located in the increased tube current zone and wearing a brassiere is not always possible, modification of the OBTCM algorithm is needed. Up until now, the user cannot alter the X-CARE angle in terms of size and position. However, HandCARE is able to switch off the X-ray exposure for a 100° angle at 3 different positions in the axial plane (at 10, 12 and 2 o'clock) as shown in Figure 10.6. The technique is a dedicated algorithm for dose savings to the operator's hand during the interventional CT procedures (Siemens Healthcare, Germany). Thus, if altering the reduced tube current angle is indeed possible, a suggestion would be to increase the dose-saving zone, used for X-CARE, from 80° to 160°. Further research is necessary to determine whether this angle is not too large and the CT acquisition is still able to deliver an acceptable image quality without increasing the overall $CTDI_{vol}$.

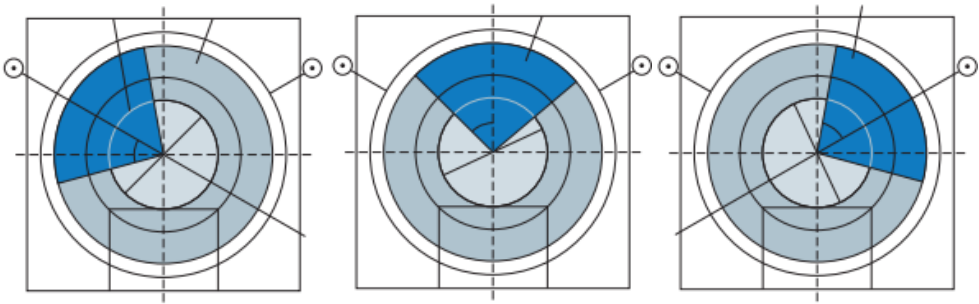


Figure 10.6 Selectable HandCARE positions (10, 12 and 2 o'clock). Blue indicates the angular range where the X-ray tube is turned off [6].

10.1 REFERENCES

- 1 Sterckx B, Franck C, Bacher K (2012) Modelling van geïndividualiseerde patiëntendosimetrie bij CT. Master dissertation, unpublished work, Ghent University
- 2 AAPM (2014) Use of Water Equivalent Diameter for Calculating Patient Size and Size-Specific Dose Estimate (SSDE) in CT (Task Group 220).
- 3 Bruesewitz MR, Yu L, Vrieze TJ, Kofler JM, McCollough CH (2008) Smart mA - Automatic Exposure Control (AEC): Physics Principles and Practical Hints. Mayo Foundation for Medical Education and Research
- 4 Rego SL, Yu L, Bruesewitz MR, Vrieze TJ, Kofler JM, McCollough CH (2008) CARE Dose4D Automatic Exposure Control System: Physics Principles and Practical Hints. Mayo Foundation for Medical Education and Research
- 5 De Roo B, Franck C, Bacher K (2014) Beeldkwaliteit bij gebruik van nieuwe CT dosisreductietechnieken: een studie aan de hand van Thiel gebalsemde lichamen. Master dissertation, unpublished work, Ghent University
- 6 Siemens Healthcare, Germany
- 7 Seidenfuss A, Mayr A, Schmid M, Uder M, Lell MM (2014) Dose reduction of the female breast in chest CT. *AJR Am J Roentgenol* 202:W447-452

Chapter 11

Dose calculation and risk estimates

The computed tomography dose index (CTDI) is a quantity expressing the average dose, resulting from a CT acquisition, to a cylindrical PMMA phantom. It is included in the dose report of the examined patient and used to compare the radiation output of different CT systems or protocols. A common misunderstanding is the use of this metric to quantify the delivered dose to the patient [1]. It is true that the density of PMMA is similar to that of a real patient, but these 16cm or 32cm cylinders are either too small or too big to represent the human anatomy. The paediatric study population used in Paper 4 of this PhD work is summarized in Table 11.1. Only 1 patient's water equivalent diameter D_w (a 5 y/o boy) matches closely to the 16cm of the 'head CTDI phantom'. For all other subjects, $CTDI_{16}$ will either under- ($D_w < 16\text{cm}$) or overestimates ($D_w > 16\text{cm}$) the dose delivered to the patient.

To account for the girth of the patient, the AAPM introduced a new metric: the size-specific dose estimate (SSDE) [2,3]. With conversion factors, based on D_w , the CTDI values are scaled to give a more realistic image of the absorbed dose to the patient. It is expected that, in the future, SSDE values will be automatically calculated for each reconstructed CT slice and stored in the DICOM header of the image [3]. Some dose management systems already provide estimates for D_w and SSDE in addition to $CTDI_{vol}$ and DLP [4-7].

Table 11.1 Summary of the study population used in Paper 1 of this PhD dissertation.

Age (y)	Gender	Height (cm)	Weight (kg)	BMI (kg/m ²)	D _w thorax (cm)	D _w abdomen (cm)
2	F	96	11	11.9	13.7	13.8
4	M	100	12	12.0	15.3	15.2
4	F	111	19	15.4	17.1	17.2
5	M	116	18	13.4	15.8	16.2
9	F	135	32	17.6	20.1	20.5
11	M	148	31	14.2	19.8	20.0
14	M	174	50	16.5	22.0	22.1
15	F	170	53	18.3	23.7	23.6
17	F	162	57	21.7	25.1	24.4
18	M	173	73	24.4	26.3	26.5

Dose calculation tools based on anthropomorphic phantoms allow a quick, yet imprecise estimation of individual organ doses. Only standard patient sizes at discrete reference ages can be used. In this PhD thesis we aimed for a more realistic representation of the human anatomy by converting the patient's CT data into a voxel model, used in a Monte Carlo environment. Besides the geometry of the scanner (centre of rotation (COR), distance focus to COR) and the properties of the beam (collimation, fan angle, spectrum and shaping filter), the starting position and angle need to be defined in the simulation software. When performing a CT examination, the location of the tube in the longitudinal (z) direction of the patient is clear. However, the position of the X-ray tube in the transverse (xy) plane is unknown. Consequently, determining the starting angle of the performed Monte Carlo simulations is not straightforward.

Relying on personal communication with Siemens, the X-ray tube does not necessarily starts at 0° (position 1 in Figure 11.1). Rather, the starting angle is equal to the last position of the tube, either at 0°, 90°, 180° or 270°, depending on the orientation of the localizer (AP, LAT or PA), taken prior to the CT acquisition. Previous studies noticed a dose increase to small and superficial located organs, when changing the starting angle [8-12]. To assess the influence on the absorbed organ doses in chest CT, we performed 4 simulations of the same patient in ImpactMC, each with a different starting angles (0°, 90°, 180° and 270°). The doses to the breasts, liver, lungs, kidneys and thyroid were calculated and are presented in Figure 11.2 [13]. No significant differences were found, except for the thyroid. According to our results, changing the tube's starting position can lead to a change in thyroid dose of 23%. Starting the simulation at 90° yields the lowest dose. Our results confirm the findings of Zhang *et al.* [12].

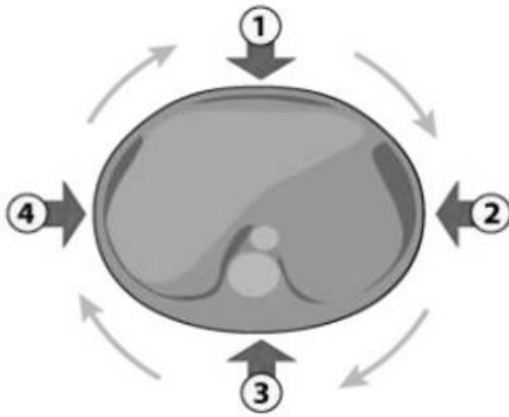


Figure 11.1 Positions of the X-ray tube in the axial (xy) plane. The tube is at position 1 (0°) or 3 (180°) to acquire an AP or PA localizer, respectively. Lateral scout scans can either be taken at positions 2 (90°) or 4 (270°).

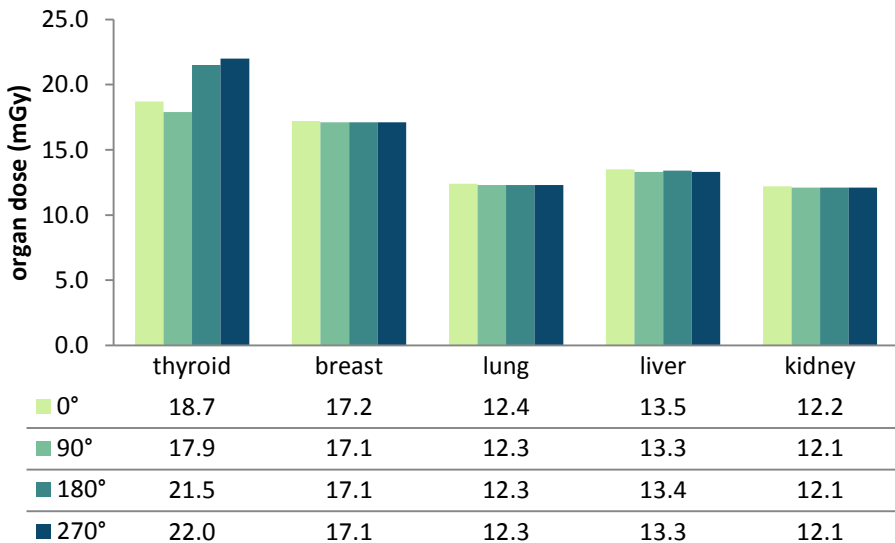


Figure 11.2 Organ doses resulting from a chest CT, in function of X-ray tube starting angles (0°, 90°, 180° and 270°). Percentages are relative differences of organ doses at different starting angles. [13]

The superficial location, small size and the fact that the organ is located at the periphery of the longitudinal FOV in a thoracic CT scan can explain the significant changes in absorbed dose. In helical CT scanning, the table moves into the gantry as the X-ray tube rotates around the patient. If the acquisition is started at 0° (or 90°), the tube will turn away from the thyroid gland, irradiating only part of the organ. By the time the tube is back at 12 o'clock, the table has moved forward and the organ is no longer in the beam. If the tube starts at 180° or (270°) the thyroid will remain longer in the primary beam, causing higher absorbed doses. All simulated CT scans in this PhD dissertation, were performed with a table feed of 34.56 mm. The mean longitudinal size of the thyroid was 34 mm or only 1 rotation. The dose to larger organs is independent of the tube's starting angle. On average, the breasts account for 159 mm in the z-direction. Consequently, 4.6 rotations were needed so that the organ was fully irradiated.

In Chapters 6, 8 and 9 of this PhD work, Monte Carlo simulations of chest CT's were performed. Because no information about the position of the X-ray tube in the axial plane was available, the starting angle was set at 0° for all simulations. In Paper 3, thyroid doses of standard and X-CARE scans were compared. Therefore, it was not necessary to know the exact position of the tube. Only a consistent set-up of the simulations was required.

Using CT data as a voxelized phantom model in Monte Carlo simulations improves dosimetric accuracy as individual organ doses can be assessed. However, in clinical practice, we only receive data of the patient's scan range, making the phantoms incomplete. For chest CT, no anatomical information of the head, abdomen and pelvis is available. In addition, no scatter can occur outside the models. In Chapter 9 of this PhD dissertation, we evaluated the consequences of using only the clinically available anatomical information of the patient. A comparison was made between simulations with a full-body model and a thoracic or abdominopelvic model (Figure 11.3).

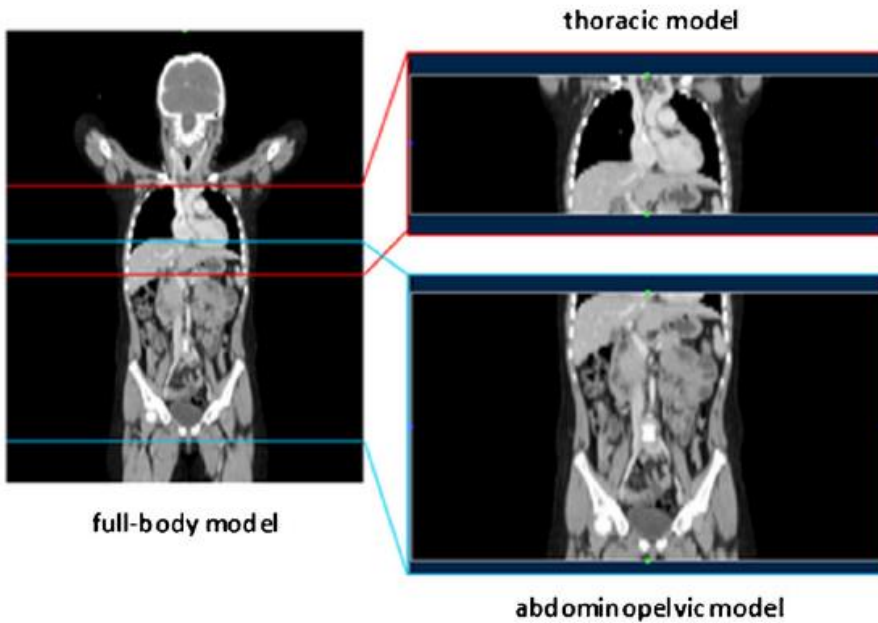


Figure 11.3 Full-body, thoracic and abdominopelvic voxelized phantom models as used in Paper 1 of this PhD work [14].

Using the full-body voxel model, the entire anatomy of the patient is available, allowing the simulated photons to scatter outside the irradiated volume as well. Besides, all relevant organs are at our disposal so that the absorbed dose can be calculated in the most accurate way. The thoracic and abdominopelvic models are incomplete, making the dose calculations less precise. In the performed study, organs on the periphery were considered to be complete. These included liver in both models as well as thyroid gland in the thoracic model. In addition, organs outside these models were assumed to receive a dose of 0 mGy. Table 11.2 summarizes the results of chest and abdominopelvic CT simulations of 10 paediatric patients. Mean relative differences in simulated organ doses between the full-body and the incomplete phantom models are shown for chest and abdominopelvic CT acquisitions.

$$relative\ difference = \frac{D_{incompl} - D_{fb}}{D_{fb}} * 100$$

Results for in-beam organs indicate the error of using the incomplete voxel model is low (< 4%). Organ doses for heart and lungs in chest CT and liver, stomach, spleen, colon, kidneys and bladder in abdominopelvic CT can be calculated by using only the patient's clinical data. There is no need to extent the models with scalable phantoms. The underestimation

of the thyroid dose can be explained by its small size and location on the border of the scan range. Apparently, a large scatter fraction contributes to the dose of this organ. On the other hand, liver, stomach and spleen dose is overestimated by the thoracic phantom, because the volume fraction included in the model is too limited. On average, the phantoms only include 70-80% of the considered organs. In reality, the other 20-30% will receive a small amount of scatter dose, which will lower the mean dose to the complete organ.

Table 11.2 Mean relative differences (%) in calculated organ doses. Simulations with the full-body and the incomplete voxel models are compared for chest and abdominopelvic CT acquisitions. A negative sign means doses calculated with the incomplete voxel model are an underestimation.

Organ	Chest CT	Abdominopelvic CT
Thyroid	-26.3	-
Heart	-1.4	-
Lungs	-2.0	-
Liver	25.7	-3.0
Stomach	24.5	-3.3
Spleen	10.7	-3.4
Colon	-	-0.5
Kidneys	-	-1.0
Bladder	-	-2.0

A possible solution is to append the available patient data with existing mathematical or hybrid phantoms. Kalender *et al* use the ORNL family to extend the acquired CT images of a 1 y/o CIRS phantom (Computerized Imaging Reference Systems, VA, USA) [15,16] (Figure 11.4). Since the 1 y/o ORNL model was larger than the CIRS physical phantom, the ORNL model was scaled with a factor 0.8, calculated as the ratio of their lateral diameters. In addition, the ORNL model was virtually wrapped with fat-equivalent layers to match the size of the CIRS phantom and to smoothen the transition between CT and voxel model data.

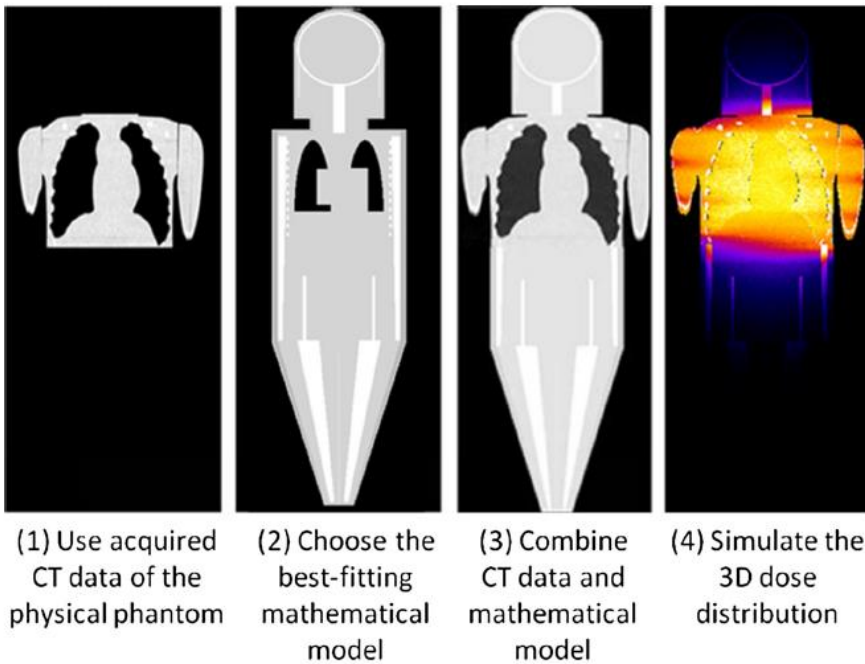


Figure 11.4 Steps for the generation of a whole-body model. The recorded CT dataset of 1 y/o CIRS phantom (1) was appended cranially and caudally with the 1 y/o ORNL mathematical voxel model (2) in order to generate a whole-body combined model (3) [16].

Immunofluorescence microscopy makes it possible to quantify the radiation effects due to CT examinations with biomarkers in the patient's blood. For example, γ -H2AX foci are formed at sites of DNA double-strand breaks in blood lymphocytes [17-19]. This makes the patient's blood dose an important parameter to quantify. In Chapter 9, blood dose was calculated according to ICRP 89 as the weighted sum of individual organ doses D_i as listed in Table 11.3 [20]. Remainder tissue was defined as the total volume of the patient, excluding individual delineated organs. A simplified calculation was proposed, including only heart, liver and lungs (+ remainder), as these are the largest blood-containing organs in the human body.

$$D_{blood} = \sum_{i=1}^n w_i * D_i$$

With $n=11$ (10 organs + remainder) or $n=4$ (3 organs + remainder).

Our study found no significant differences in blood dose calculation between both methods, implying D_{blood} can be defined using only heart, liver and lung doses.

In the calculation of D_{blood} the remainder dose was scaled according to the weight of the patient. By multiplying its volume with its mass density (1.050 g/cm^3), the weight of the simulation model was calculated. An accurate estimate of the remainder dose is crucial, since it is the dominant organ in the calculation of D_{blood} (Table 11.3).

Table 11.3 Blood content in percentage of total blood volume [20].

Organ	Blood content w_i (%)
heart	10.00
liver	10.00
lungs	12.50
remainder	67.5
bladder	0.02
colon	2.20
stomach	1.00
thyroid	0.06
gonads	0.04 ^a
kidneys	2.00
spleen	1.40
remainder	60.78 ^a

^aData are given for males. For females, blood content of gonads and remainder is respectively 0.02% and 60.80%.

Recent studies of our research group observed a low-dose hypersensitivity to radiation exposure in children, which challenges the LNT hypothesis [28,29]. DNA damage was estimated by scoring γ -H2AX foci in peripheral blood T lymphocytes. Earlier work demonstrated that the γ -H2AX foci assay, a biological method, can be used to determine the effect of CT exposure at the molecular level [17-19]. Results of the study of Vandevoorde *et al* are shown in Figure 11.5. The mean number of foci per cell, related to the amount of DNA double-strand breaks, is plotted against the absorbed blood dose in paediatric patients undergoing a chest or abdomen CT. It can be seen that a linear extrapolation, based on the amount of foci induced in cord blood after an *in vitro* dose of 0.5 Gy, underestimates the radiation effects of lower doses. The observed results can be explained by the bystander effect, in which genetic and biochemical changes not only occur in cells hit by ionizing radiation but also in unexposed 'bystander' cells, in close proximity to the directly hit cells.

Assessing the dose to the blood remains challenging since blood is a circulating organ. The reference adult male contains 5.3 litres of blood and has a cardiac output of 6.5 l/min [20], meaning 1 circulation takes almost 60 seconds. For children, the blood flow is slightly higher. For a 5 y/o, the round trip is made in 25 seconds. These values are high compared to a typical thoracic or abdominal CT examination of 5-10 seconds. This partial irradiation of the total blood volume eventually leads to an overestimation of dose. However, the methodology used in Chapter 9 is the best we can do so far as it includes patient-specific dose calculations as opposed to the anthropomorphic phantoms in other dosimetry tools [30,31]. If the obtained blood doses were indeed an overestimation, the curve in Figure 11.5 will shift to the left, towards lower dose values. For the same number of foci per cell, the absorbed blood dose will be lower. As a result, the underestimation of the LNT model will even be larger than initially observed.

The abovementioned example illustrates the strong need for accurate individualized dosimetry in medical imaging to improve and support scientific knowledge on the biologic effects of ionizing radiation in the clinical dose range.

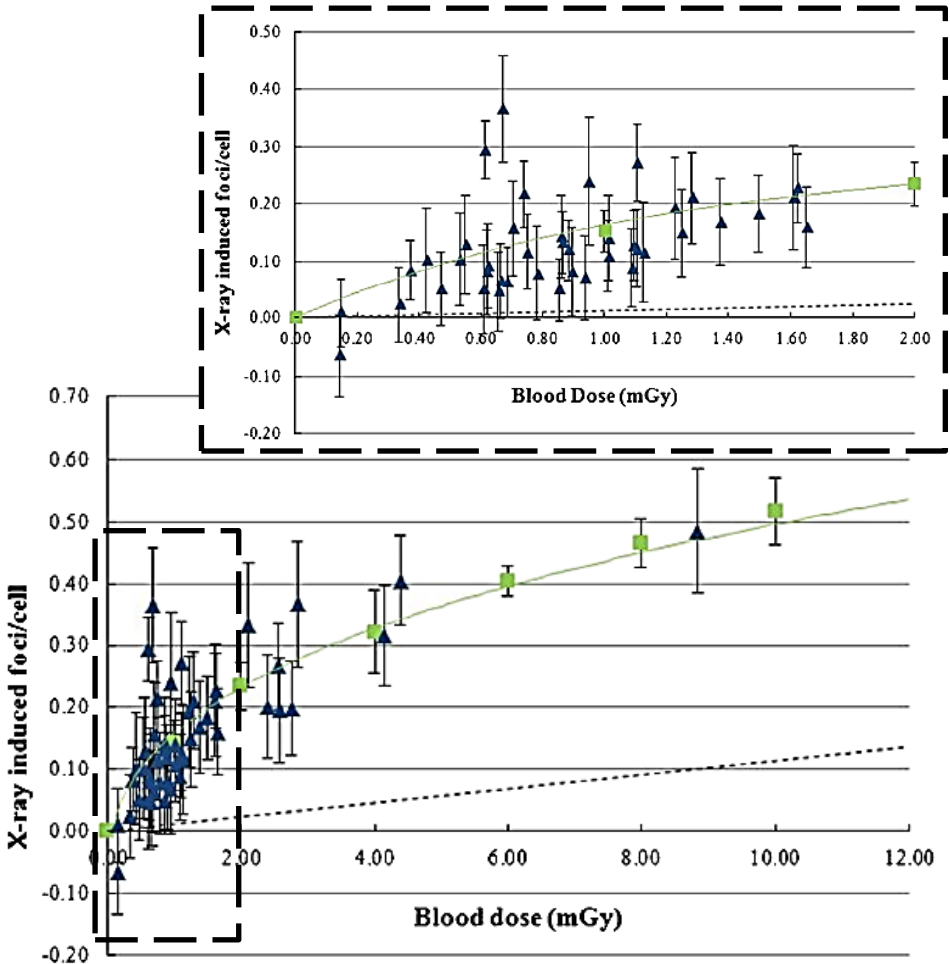


Figure 11.5 Mean number of γ -H2AX-foci per cell induced by in vivo X-ray exposure plotted versus the Monte Carlo calculated blood dose in paediatric patients undergoing a chest or abdomen CT (*blue*). The dose-response curve after in vitro X-ray irradiation of cord blood is shown in *green*. The *dashed line* represents a linear extrapolation based on the γ -H2AX foci induced in cord blood after an in vitro dose of 0.5 Gy, based on the LNT hypothesis. Since a large part of the data are clustered in the 0-2 mGy range, this is presented in a separate figure [29].

11.1 REFERENCES

- 1 McCollough CH, Leng S, Yu L, Cody DD, Boone JM, McNitt-Gray MF (2011) CT dose index and patient dose: they are not the same thing. *Radiology* 259:311-316
- 2 AAPM (2011) Size-specific dose estimates (SSDE) in pediatric and adult body ct examinations (Task Group 204).
- 3 AAPM (2014) Use of Water Equivalent Diameter for Calculating Patient Size and Size-Specific Dose Estimate (SSDE) in CT (Task Group 220).
- 4 (2015) TQM Dose. Qaelum NV, Leuven, Belgium. Available via <http://www.qaelum.com/>. Accessed 01.12.2016
- 5 (2016) DoseWatch. GE Healthcare. Available via http://www3.gehealthcare.com/en/products/dose_management/dosewatch/. Accessed 01.12.2016
- 6 (2016) Radimetrics Enterprise Platform. Bayer HealthCare LLC. Available via <https://www.radiologysolutions.bayer.com/products/ct/dosemanagement/rep/>. Accessed 01.12.2016
- 7 (2017) teamplay. Siemens Healthcare. Available via <https://www.healthcare.siemens.com/medical-imaging/low-dose/low-dose-information-by-modality/cross-modality-approaches/teamplay>. Accessed 25.03.2017
- 8 Liu H, Liu T, Xu X, Wu J, Zhuo W (2015) Eye Lens Dose Reduction From CT Scan Using Organ Based Tube Current Modulation. *Med Phys* 42:3250-3250
- 9 Matsubara K, Sugai M, Toyoda A et al (2012) Assessment of an organ-based tube current modulation in thoracic computed tomography. *J Appl Clin Med Phys* 13:148-158
- 10 Seidenfuss A, Mayr A, Schmid M, Uder M, Lell MM (2014) Dose reduction of the female breast in chest CT. *AJR Am J Roentgenol* 202:W447-452
- 11 Tsai HY, Liao YL, Lai NK, Chen JR, Chen TR (2015) Patient Eye-Lens Dose Reduction in Routine Brain CT Examinations Using Organ-Based Tube Current Modulation and In-Plane Bismuth Shielding. *Med Phys* 42:3584-3584
- 12 Zhang D, Zankl M, DeMarco JJ et al (2009) Reducing radiation dose to selected organs by selecting the tube start angle in MDCT helical scans: A Monte Carlo based study. *Med Phys* 36:5654-5664
- 13 Van de Sande L, Franck C, Bacher K (2016) Analyse van dosis en beeldkwaliteit bij gebruik van X-Care voor CT-beeldvorming. Master dissertation, unpublished work, Ghent University
- 14 Franck C, Vandevoorde C, Goethals I et al (2016) The role of Size-Specific Dose Estimate (SSDE) in patient-specific organ dose and cancer risk estimation in paediatric chest and abdominopelvic CT examinations. *Eur Radiol* 26:2646-2655
- 15 Cristy M, Eckerman KF (1987) Specific absorbed fractions of energy at various ages from internal photon sources I: methods. Oak Ridge National Laboratory Report.
- 16 Kalender WA, Saltybaeva N, Kolditz D, Hupfer M, Beister M, Schmidt B (2014) Generating and using patient-specific whole-body models for organ dose estimates in CT with increased accuracy: feasibility and validation. *Phys Med* 30:925-933

- 17 Beels L, Bacher K, Smeets P, Verstraete K, Vral A, Thierens H (2012) Dose-length product of scanners correlates with DNA damage in patients undergoing contrast CT. *Eur J Radiol* 81:1495-1499
- 18 Lobrich M, Rief N, Kuhne M et al (2005) In vivo formation and repair of DNA double-strand breaks after computed tomography examinations. *Proc Natl Acad Sci U S A* 102:8984-8989
- 19 Rothkamm K, Balroop S, Shekhdar J, Fernie P, Goh V (2007) Leukocyte DNA damage after multi-detector row CT: a quantitative biomarker of low-level radiation exposure. *Radiology* 242:244-251
- 20 ICRP (2002) Basic anatomical and physiological data for use in radiological protection: reference values. A report of age- and gender-related differences in the anatomical and physiological characteristics of reference individuals. ICRP Publication 89. *Ann ICRP* 32:5-265
- 21 Preston DL, Shimizu Y, Pierce DA, Suyama A, Mabuchi K (2003) Studies of mortality of atomic bomb survivors. Report 13: Solid cancer and noncancer disease mortality: 1950-1997. *Radiat Res* 160:381-407
- 22 Council N (2006) Health risks from exposure to low levels of ionizing radiation: BEIR VII phase 2. The National Academies Press
- 23 Morgan WF, Bair WJ (2013) Issues in low dose radiation biology: the controversy continues. A perspective. *Radiat Res* 179:501-510
- 24 Averbeck D (2009) Does scientific evidence support a change from the LNT model for low-dose radiation risk extrapolation? *Health Phys* 97:493-504
- 25 Grudzenski S, Rath S, Conrad S, Rube CE, Lobrich M (2010) Inducible response required for repair of low-dose radiation damage in human fibroblasts. *Proc Natl Acad Sci U S A* 107:14205-14210
- 26 Tubiana M, Feinendegen LE, Yang C, Kaminski JM (2009) The linear no-threshold relationship is inconsistent with radiation biologic and experimental data. *Radiology* 251:13-22
- 27 Brenner DJ, Doll R, Goodhead DT et al (2003) Cancer risks attributable to low doses of ionizing radiation: assessing what we really know. *Proc Natl Acad Sci U S A* 100:13761-13766
- 28 Beels L, Bacher K, De Wolf D, Werbrouck J, Thierens H (2009) gamma-H2AX foci as a biomarker for patient X-ray exposure in pediatric cardiac catheterization: are we underestimating radiation risks? *Circulation* 120:1903-1909
- 29 Vandevoorde C, Franck C, Bacher K et al (2015) gamma-H2AX foci as in vivo effect biomarker in children emphasize the importance to minimize x-ray doses in paediatric CT imaging. *Eur Radiol* 25:800-811
- 30 ImPACT. Available via www.impactscan.org. Accessed 20/03/2017
- 31 CT-Expo, Medizinische Hochschule, Hannover, Germany

Chapter 12

Image quality

CT image reconstruction is a mathematical process where the measured raw data projections, acquired during the rotational exposure, are transformed into volumetric image data. The traditional filtered backprojection (FBP) method includes many approximations of the true CT scan process and is therefore susceptible to noise and artefacts. The alternative way to handle the reconstruction process is through iterative methods. Iterative reconstruction (IR) approaches the final CT image gradually. The method can take into account the noise statistics which will result in a more accurate and reliable outcome.

With traditional FBP it is assumed that a point source in the X-ray tube sends a pencil beam through point voxels in the patient, which will reach point detector cells with a perfect noise sample. Model-based IR allows the focal spot to be finite, sending a divergent beam through finite 3D voxels in the patient which are then projected to a finite detector structure. In addition, a more realistic noise model including quantum and electronic noise is applied [1].

In Figure 12.1 the noise power spectrum of a standard FBP image (black curve) and three IR methods are compared. It can be seen that the FBP has the largest magnitude in NPS. The IR images contain significantly less noise. However, the NPS peak is shifted to the lower frequencies when a higher level of IR is used. These differences in noise texture in the clinical images have a potential effect on the human detection.

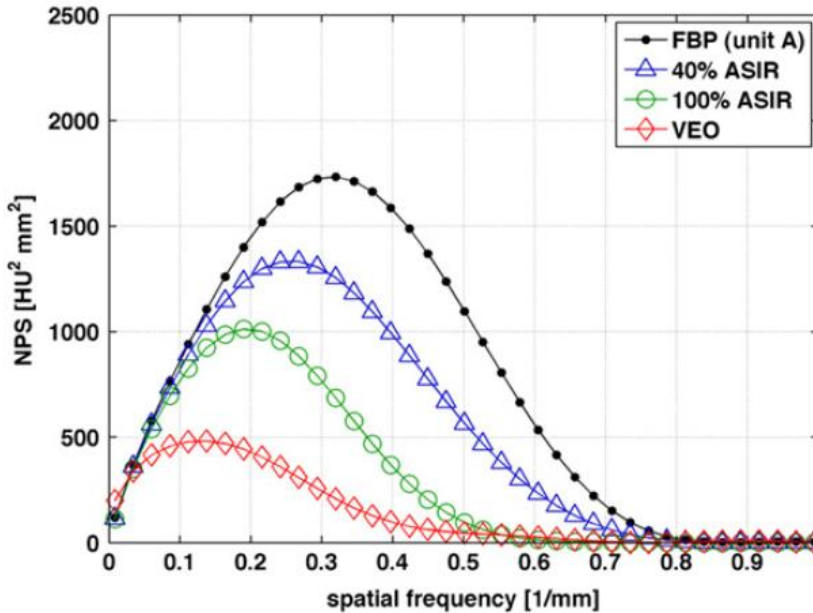


Figure 12.1 Noise power spectra of a FBP reconstructed image (black) and 3 IR methods: 40% ASIR (blue), 100% ASIR (green) and VEO (red) [1].

Although the capacity of IR for improvement of IQ has been shown, severe dose reduction can result in loss of lesion detection, particularly in low-contrast regions [2]. Studies have shown reductions in sharpness and loss of margins (e.g. portal vein) and organ edges associated with some iterative reconstruction techniques [3]. By using denoising techniques, maintenance of IQ does not always guarantee preservation of diagnostic performance on low-dose CT. Understanding if the noise texture of iterative reconstructions can affect the diagnostic quality for a patient, or if it is only a matter of habit due to the radiologist's FBP background, appears to be an important challenge to safely set up low- and ultra-low-dose protocols [4]. The use of higher strengths of IR can result in a somewhat unfamiliar, almost "plastic" appearance of the images [5]. As a consequence, high levels of dose reduction should be introduced gradually and guided by reader performance. Studies with reference standards can be used to ensure that a particular dose reduction can be achieved while still fulfilling the requirements for a specific diagnostic task.

In Chapter 7 of this PhD dissertation, an algorithm based on local standard deviations was used to assess the IQ in chest CT. Results were compared with the outcome of a human observer study. CT datasets were reconstructed using FBP and two different strengths of SAFIRE (B30, I30/1 and I30/3; Siemens Healthcare, Germany). A significantly high correlation was found between VGA scores and IQs values, both for FBP ($\rho = 0.943$) and

SAFIRE ($\rho = 0.902$) images. Consequently, the proposed algorithm does account for differences in image appearance due to changes in noise texture. This can be explained by the nature of the algorithm. Unlike global noise measurements performed in selected ROIs, the method assesses local SD in the surroundings of every single pixel of the image [6].

The traditional IQ parameters (CNR, MTF, NPS, DQE) are useful for image detector characterisation and to ensure conformity of CT systems. However, in the framework of patient dose optimization, task based assessment of IQ is required. To this end, evaluation of patient images by interpreting radiologists is the most accepted approach. Because this approach is extremely labour intensive and becomes unmanageable when multiple imaging parameters have to be optimized, more efficient methods are needed [7]. Task based IQ metrics obtained with model observer studies have gained popularity in CT image quality evaluation. These are mathematical models designed to make decisions on defined tasks based on statistical decision theory and can be divided into two main groups [8-10]:

1. *Classification* is used for low contrast problems. The pathology (signal) can be present or absent, either in a uniform or structured background.
2. *Estimation* is a high contrast task where the size and shape of the object have to be determined.

The basic principle of a model observer is to make a convolution of the image with a template to obtain a decision variable. The template is the type of observer used in the model. The ideal observer utilizes all the available statistical information in the image regarding the task, to maximize the outcome. The performance of an ideal observer provides the upper bound that is achievable by any observer [11]. To be more in relation with the performance of human observers, various anthropomorphic observers are developed. Examples include the non-prewhitening matched filter (NPWE) [12,13] and the channelized Hotelling observer (CHO) [12,14].

The disadvantage of these methods is that they are defined for simple situations, like the detection of a representative signal in a given phantom. Once a model observer is verified to be highly predictive of human observers in realistic diagnostic tasks, objective IQ assessment becomes feasible. However, until now, the tasks investigated with mathematical model observer studies remain very basic and far from clinical reality. They do not cover the whole range of characteristics that define IQ at the clinical level [8]. The automatic IQ scoring algorithm used in Chapter 7 of this PhD work has proven to a valuable alternative for image quality assessment. The method could allow for IQ monitoring over time without the need for human intervention.

12.1 REFERENCES

- 1 Thibault JB, Sauer KD, Bouman CA, Hsieh J (2007) A three-dimensional statistical approach to improved image quality for multislice helical CT. *Med Phys* 34:4526-4544
- 2 Goenka AH, Herts BR, Obuchowski NA et al (2014) Effect of reduced radiation exposure and iterative reconstruction on detection of low-contrast low-attenuation lesions in an anthropomorphic liver phantom: an 18-reader study. *Radiology* 272:154-163
- 3 Patino M, Fuentes JM, Singh S, Hahn PF, Sahani DV (2015) Iterative Reconstruction Techniques in Abdominopelvic CT: Technical Concepts and Clinical Implementation. *AJR Am J Roentgenol* 205:W19-31
- 4 Mieville FA, Gudinchet F, Brunelle F, Bochud FO, Verdun FR (2013) Iterative reconstruction methods in two different MDCT scanners: physical metrics and 4-alternative forced-choice detectability experiments--a phantom approach. *Phys Med* 29:99-110
- 5 Geyer LL, Schoepf UJ, Meinel FG et al (2015) State of the Art: Iterative CT Reconstruction Techniques. *Radiology* 276:339-357
- 6 Kortensniemi M, Schenkel Y, Salli E (2008) Automatic image quality quantification and mapping with an edge-preserving mask-filtering algorithm. *Acta Radiol* 49:45-55
- 7 Leng S, Yu L, Zhang Y, Carter R, Toledano AY, McCollough CH (2013) Correlation between model observer and human observer performance in CT imaging when lesion location is uncertain. *Med Phys* 40:081908
- 8 Verdun FR, Racine D, Ott JG et al (2015) Image quality in CT: From physical measurements to model observers. *Phys Med* 31:823-843
- 9 Barrett HH, Yao J, Rolland JP, Myers KJ (1993) Model observers for assessment of image quality. *Proc Natl Acad Sci U S A* 90:9758-9765
- 10 Beutel J (2000) Handbook of medical imaging. SPIE Press, Bellingham, Wash.
- 11 Yu L, Leng S, Chen L, Kofler JM, Carter RE, McCollough CH (2013) Prediction of human observer performance in a 2-alternative forced choice low-contrast detection task using channelized Hotelling observer: impact of radiation dose and reconstruction algorithms. *Med Phys* 40:041908
- 12 Hernandez-Giron I, Calzado A, Geleijns J, Joemai RM, Veldkamp WJ (2015) Low contrast detectability performance of model observers based on CT phantom images: kVp influence. *Phys Med* 31:798-807
- 13 Veldkamp WJ, Kroft LJ, van Delft JP, Geleijns J (2009) A technique for simulating the effect of dose reduction on image quality in digital chest radiography. *J Digit Imaging* 22:114-125
- 14 Zhang Y, Pham B, Eckstein MP (2004) Evaluation of JPEG 2000 encoder options: human and model observer detection of variable signals in X-ray coronary angiograms. *IEEE Trans Med Imaging* 23:613-632

Chapter 13

Final conclusions

The objective of this PhD dissertation was to assess the performance of CT systems in terms of patient dose and image quality (IQ). The behaviour of tube current modulation (TCM) techniques was investigated with patient-specific phantoms and Monte Carlo simulations. An edge-preserving mask algorithm was used for automatic IQ evaluation. In addition, a clinically applicable method was developed to calculate patient-specific organ doses and to estimate the risk of radiation induced malignancies, resulting from CT examinations.

Evaluation of different tube current modulation systems showed that there is a need to optimize this technique. Both the localizer type (AP, PA or LAT) and the scan direction have an important influence on the dose reducing efficacy of TCM. In chest CT, a 60% lung and thyroid dose reduction was achieved when the CT acquisition was based on two orthogonal localizers instead of a single PA projection. The patient's size and attenuation level can be estimated more accurately by the system if a dual scout is available. Hence, the generated tube current values will be lower, resulting in an overall decrease in dose. Performing the CT acquisition in the caudocranial (feet first) direction reduces the thyroid dose with 50%, without significant differences in image quality.

Excellent correlations were found between the proposed IQ scoring algorithm (IQs) and different physical-technical image quality parameters (noise, CNR and IQF_{inv}) in thoracic CT. In addition, the IQs metric correlates highly with the observed clinical IQ, expressed as VGAS. After normalizing the image quality score, different reconstruction kernels can be compared. This automatic scoring algorithm is a promising tool for clinical IQ evaluation in chest CT. It allows IQ monitoring over time without the need for human intervention. With the use of this metric, CT reconstructions can be compared to a reference dataset or to other patients. Subtle changes in IQ can be detected automatically by setting appropriate alerts in a quality management environment.

The potential benefit of organ-based TCM to the female breast in chest CT is overestimated. The anterior range of reduced exposure values is too limited. Glandular tissue is located more laterally and even extends into the high tube current zone. An

average dose reduction to the breasts of only 9% was observed, whereas the thyroid dose was reduced with 18%. However, liver, lungs and kidneys experienced a dose increase of 11%, 17% and 26% respectively, resulting in no overall benefit for radiation induced cancer risks. Application of the IQs metric showed an improvement of the image quality for organ-based TCM scans. Consequently, if one aims for the same IQ-level for both standard and organ-based TCM acquisition, X-CARE exposure values can be reduced.

The size-specific dose estimate (SSDE) represents the average dose to the patient, yet does not allow the estimation of individual organ doses. However, excellent correlations were found between SSDE and simulated organ doses in paediatric chest and abdominopelvic CT scans. Conclusions about organ doses and radiation induced cancer risks can be made on the basis of this metric, by taking into account a linear correction factor. This makes an on-the-spot dose and LAR estimation possible in routine clinical practice. The SSDE needs to be available in the patient's dose report so that risk estimations of radiation induced malignancies can be performed more accurately.

Chapter 14

Future perspectives

The last years, CT manufacturers increasingly invest in radiation dose reduction tools. Tube current modulation and peak kilovoltage optimization aim to lower the tube output by adapting the exposure to the specific size of the patient. Iterative reconstruction methods and more advanced detectors improve the image quality of a CT dataset. The medical physics expert should play a key role in both the evaluation of new technology during commissioning, the optimization of these systems and the support/training of local staff using them.

This PhD thesis concluded that the breasts of supine positioned women are located too far laterally to benefit from the use of organ-based tube current modulation (OBTCM). However, this technique holds a significant dose reducing potential, if the user is able to modify the size and position of the dose saving angle. Consequently, performance optimization of OBTCM systems is essential future work.

An automatic image quality method, based on local standard deviations in the image, was evaluated for use in CT. A significant correlation was found between the observed clinical image quality and the outcome of the proposed algorithm. Additional research in large patient cohorts is needed for further evaluation of the clinical validity of this approach. Furthermore, other anatomic regions should be included in future studies. Last, the performance of the method is not yet investigated in other imaging modalities. It would be useful to explore the potential of automatic IQ evaluation tools in both radiography and fluoroscopy.

Automated IQ analysis could become an essential part in dose management software tools. In fact, apart from systematically analysing patient dose, a relevant objective evaluation of image quality is still missing in these systems.

Task based IQ metrics based on model observer studies have gained popularity in CT image quality evaluation. Due to their simplicity, most of these studies are performed using objects with a uniform background. Phantoms with a realistic texture and lesion appearance are highly desirable as performance may be affected by the anatomical

background. The commercially available anthropomorphic phantoms are usually not patient-specific and difficult to customize. A possible solution would be the use of 3D printing techniques to create more realistic training phantoms, based on clinical CT data. Alternatively, the use of human cadavers could serve as an ideal surrogate of the patient model.

Part IV

About the author

PERSONAL INFORMATION

Name	Caro Franck
Address	Nieuwstraat 1, 2630 Aartselaar
Date of Birth	September 14, 1987
Nationality	Belgian
Mobile	+32 486 14 35 67
E-mail	caro.franck@ugent.be

PROFESSIONAL CAREER

- Jan 2013 - present PhD in Health Sciences – IWT doctoral grant
“Towards patient-specific dose and image quality in CT imaging”
Supervisors: Prof. Dr. Ir. K. Bacher and Prof. Dr. E. Achten

Ghent University – Department of Basic Medical Sciences – Medical Physics
- Sep 2013 - present Licensed medical physics expert (radiology)

QCC Ghent, Ghent University
- Oct 2011 - Dec 2012 Teaching assistant
Responsible for practical classes and exercises in physics

Ghent University – Department of Basic Medical Sciences - Medical Physics

EDUCATION AND TRAINING

2011 – 2013	Professional medical physicist training (radiology) <i>Ghent University – Medical Physics / QCC Ghent</i>
2011 – 2013	Postgraduate: Expert in medical physics (radiology) <i>Ghent University</i>
2005 – 2011	Master of Science in Biomedical Engineering <i>Ghent University</i>

A1 PUBLICATIONS

C. Vandevoorde, **C. Franck**, K. Bacher, L. Breyssem, M.H. Smet, C. Ernst, A. De Backer, K. Van De Moortele, P. Smeets & H. Thierens. Gamma-H2AX foci as in vivo effect biomarker in children emphasize the importance to minimize x-ray doses in paediatric CT imaging. *Eur Radiol* (2015) 25:800-811

C. Franck, C. Vandevoorde, I. Goethals, P. Smeets, E. Achten, K. Verstraete, H. Thierens & K. Bacher. The role of Size-Specific Dose Estimate (SSDE) in patient-specific organ dose and cancer risk estimation in paediatric chest and abdominopelvic CT examinations. *Eur Radiol* (2016) 26:2646-55

C. Franck & K. Bacher. Influence of localizer and scan direction on the dose-reducing effect of automatic tube current modulation in computed tomography. *Radiat Prot Dosimetry* (2016) 169 (1-4):136-142

C. Franck, A. De Crop, B. De Roo, P. Smeets, M. Vergauwen, T. Dewaele, M. Van Borsel, E. Achten, T. Van Hoof, K. Bacher (2017) Evaluation of automatic image quality assessment in chest CT – a human cadaver study. *Phys Med* 36:32-37

INTERNATIONAL COMMUNICATION

European Congress of Radiology 2017 (Vienna, Austria)

Oral presentation: A human cadaver study to evaluate automatic image quality assessment in chest CT

European Congress of Radiology 2016 (Vienna, Austria)

Oral presentation: Scan direction and scout acquisition influences the dose reducing effect of automatic tube current modulation in CT

Optimisation in X-ray and Molecular Imaging 2015 (Gothenburg, Sweden)

Oral presentation: Influence of scout acquisition and scan direction on the dose reducing effect of automatic tube current modulation

European Congress of Radiology 2015 (Vienna, Austria)

Oral presentation: Size-specific dose estimate (SSDE) can be used to estimate patient-specific blood dose from paediatric CT examinations

NATIONAL COMMUNICATION

Annual Symposium of the Belgian Hospital Physicist Association 2017 (Ghent)

Oral presentation: A human cadaver study to evaluate automatic image quality in chest CT

Annual Symposium of the Belgian Hospital Physicist Association 2015 (Antwerp)

Oral presentation: SSDE can be used to calculate patient-specific blood doses from paediatric CT examinations